High Speed Flywheel and Test Rig Design for Rural Energy Storage

By Richard Okou

This thesis is submitted to the Department of Electrical Engineering, University of Cape Town, in complete fulfilment of the requirements for the degree of Doctor of Philosophy

February 2010

Declaration

I hereby:

(a) Grant the University free license to reproduce the above thesis in whole or in part, for the purpose of research;

(b) Declare that:

(i) The above thesis is my own unaided work, both in conception and execution, and that apart from the normal guidance of my supervisor. Where collaboration with other people has taken place, or material generated by other researchers is included, the parties and/or materials are indicated in the acknowledgements or are explicitly stated with references as appropriate.

(ii) Except as stated below, neither the substance nor any part of the thesis has been submitted in the past, or is being, or is to be submitted for a degree at this University or any other University.

(iii) I am now presenting the thesis for examination for the Degree of PhD.

Richard Okou

Date

To Dad (Rtd Dr), Mum (MP) and the entire Otim Family

For all the sacrifice, love and encouragement.

Acknowledgements

Firstly, I would like to thank the almighty Lord God for giving me life and protecting me throughout my time. There is truly nothing impossible with the Lord and his son Jesus Christ by your side.

Special thanks to my loving mother Mrs. Dorothy Otim (Sr. MP) and loving father, Dr. (Rtd) Charles Peter Otim for your consistent encouragement, love and sacrifice over the years. You are the best parents anyone would ever wish for.

My sincere thanks to my thesis supervisors, Professor Pragasen Pillay, Dr. Mohamed Azeem Khan and Dr. Paul Stanley Barendse for the high level guidance, advice and financial support throughout my studies.

I am indebted to Dr. Dave Johnson, Mr. Guan Rui, Mr. Gomezyani Mwaba and Mr. Michel Nlandu for laying the foundation to this work. Special thanks are extended to Dr. Ben Sebitosi and Dr. Marubini Manyage for the encouragement and in depth insight into this research.

I am also grateful for the support received from Mr. Chris Wozniak, Mrs. Marlene Joubert and Mr. Philip Titus, thank you so much. To my colleagues and friends Barbara Herndler, John Wanjiku, Ashwill, Stefan Sager and Jaffer Abu baker, thanks for consistent assistance in the laboratory.

My sincere thanks to my friends Diana Nakkazi, Jerry Oluk, Stephen Kinara, Julio Sebanenya, Milton Edimu, Mao Amis, Justin Masuka, Josephine Nakato, Sara Kabahuma, Raymond Mugwanya, Nalongo, Gladys Kigozi, Fredo, Jojo, Charlie, Dora and John Kazembe for the support and love. Special thanks to my brothers from Pallisa, Denis Etyono, John Okoboi, Abdallah, Omadang, Obelle, Jomo Erugudo, Simon Okanya, Engineer, Joshua and Tom.

I am indebted to the CAP family, for all the derailing and the special memories but most importantly your comfort and love. You brought Pallisa so close to Cape Town! Thank you so much!

To the Otim family Kernan, Keroy, Elaine, Emma, Baraka, Ps. Arot, Charles, Karla, Rachel, Jane, Charles and Jemimah. I could not have done this without your support, encouragement and sacrifice. You are the best family anyone would love to have and cherish. Thank you for the prayers, I love you all.

Finally to the Tatas, Mamei Keda Nu Ija Kere, you always listened and welcomed me to your homes and loved me like your own. I thank you and Yalama Ailip.

May the Almighty Lord bless you all.

Abstract

There is considerable growth in the renewable energy sector to contribute to sustainable development, environmental conservation and most importantly to provide affordable energy to isolated rural communities of sub-Saharan Africa. Renewable energy sources such as solar and wind require energy storage since the source of energy is intermittent. Electrochemical batteries especially from lead acid are commonly used to store energy in Solar Home Systems (SHS) for rural electrification in sub-Saharan Africa. Disadvantages such as low efficiencies, low life cycle costs, high maintenance, comparatively short life and serious environmental and human toxicity effects exist. Since recycling is not widespread, replacement costs are high, as are the resultant environmental damage and health hazards from lead and sulphuric acid. In this thesis, an electromechanical flywheel energy storage device is proposed as an alternative to a lead acid battery in order to increase efficiency, life expectancy, increased high depth of discharge, low life cycle cost and elimination of adverse environmental effects.

Due to income and service skill constraints in rural areas, the proposed, high speed flywheel systems (for long time energy storage) will require the use of low cost configurations and topologies, special considerations on the flywheel rotor profile design, robust electrical machines, simple power electronics and a low cost bearing set. Low loss magnetic bearings are also possible but were limited by time while also making their maintenance complex especially in rural areas.

Conventional high strength composite materials used in flywheel rotor manufacture for high speed operation are expensive. Therefore there is a need to develop techniques to profile the rotor shape so as to improve on material usage and exhibit lower mechanical stresses. A robust electrical machine topology for high speed operation and a simple drive system are investigated to ensure simple assembly, low cost and low maintenance.

The various flywheel components were designed using analytical and numerical methods. Two techniques were used to develop two optimal profiles for the flywheel rotor structure. Partial differential equations and analytical solutions were employed to develop the profiles. Analytical equations were used to design the electrical machine, drive, bearing system and other accessories. The final electromechanical battery prototype consisted of a composite flywheel rotor made from E-glass fibre materials, double rotor Axial Flux Permanent Magnet (AFPM) machine and a drive system using Brushless DC (BLDC) mode of operation. The system was designed for 300Wh of energy storage for the delivery of 100W and 500W of power and an operating speed range of 8,000 rpm-25,000 rpm.

The design and development of the flywheel energy storage system and test rig using locally available materials was investigated. Experiments were conducted for speeds up to 6,000 rpm. The electromechanical battery was able to store a maximum of 77Wh of energy. The shortfall of the system to meet its design specifications was investigated and found to have been caused by vibrations resulting from prototyping issues. A thermal model was developed to predict the temperature rise in the system which showed a good correlation with the experimental results.

Table of contents

List of Figures

List of Tables

List of Abbreviations

AFPM	-Axial Flux Permanent Magnet
BLDC	-Brushless Direct Current Machine
CAD	-Computer Aided Design
CAES	-Compressed Air Energy Storage
CNC	-Computer Numerical Controlled
CFCA	-Crushing Fragment Containment Analysis
CW	-Clockwise
DC	-Direct Current
DOF	-Degrees of Freedom
EMF	-Electro Motive Force
FEA	-Finite Element Analysis
FEM	-Finite Element Method
HOMER	-Hybrid Optimisation Model for Distributed Power
Hz	-Hertz
ID	-Inner Diameter
MGoe	-Mega Gauss Oersteds
MMF	-Magneto Motive Force
MPa	-Mega Pascal
NASA	-Nationals Aeronautics Space Administration
NdFeB	-Neodymium Iron Boron

OECD	-Organization for Economic Cooperation and Development
OD	-Outer Diameter
NREL	-National Renewable Energy Lab
PM	-Permanent Magnet
PMAC	-Permanent Magnet Alternating Current
PWM	-Pulse Width Modulation
RFPM	-Radial Flux Permanent Magnet
RPM	-Revolutions Per Minute
SHS	-Solar Home Systems
SKE	-Specific Kinetic Energy
USD	-United States Dollar

Chapter 1

Introduction

This thesis critically evaluates the development of a low cost high speed flywheel energy storage system for energy applications in rural areas. Detailed analysis of the flywheel rotor system are clearly described. A design approach of the Axial Flux Permanent Magnet machine and Brushless DC drive are described. The design of the test rig is also explained. In this chapter, the background to the research is given, a review of other energy storage systems is provided, a brief literature review is compiled and an overview of the thesis is presented.

1.1 Background

There is renewed interest in renewable energy, which is largely attributed to concerns over increased global energy demand, climate change effects and continued depletion of conventional energy sources. These conventional sources account for 79% [1.1] of the total global energy supply. The increased use of conventional fuels has created a versatile change in climate an aspect linked to global warming. The global energy demand is projected to grow by 50% from 2005 to 2030 [1.2] and the non Organization for Economic Cooperation and Development (OECD) countries account for 85%. In addition, this increase can also be attributed to a large portion of the world's population not having access to electricity. Two billion people in the world today lack access to electricity and other modern sources of energy. In South Africa alone, 66% have access to electricity [1.3] and in the case of Uganda; only 6% have access to electricity and only 1% from rural areas [1.4], 2% for Zambia and 5% for Kenya and Mali [1.1]. These non-electrified rural areas in sub-Saharan Africa are usually far away from the grid, are mountainous, or not

considered economically viable. They are gifted by nature giving rise to renewable energy resources that can be harnessed to produce electricity from anywhere. This means, unlike traditional central power generation, some renewable energy can be generated close to where it is required and massive savings on transmission infrastructure and power delivery losses can be realized. The intermittent nature of the resources however, means that power is often generated before or after it is required [1.5]. Therefore, in order to reliably utilize these resources, suitable energy storage must be available.

Current energy storage technologies are however, still riddled with various problems. The lead acid battery, which is extensively used in Sub Saharan Africa in solar Photovoltaic (PV) cells, for example, is characterized by high maintenance costs, low depth of discharge, limited number of charge cycles and short life spans. In addition, the lead acid battery is widely used in rural electrification projects where environmental waste policies are not enforced making its hazardous waste a potential threat. Hydropower storage technology on the other hand has high capital costs and requires adequate water resources with the right geo-terrain. Others include magnetic storage in superconducting medium but are currently still in its development stages. Needless to say, energy storage is by far one of the biggest challenges to the viable exploitation of renewable energy resources. Today, the total storage capacity worldwide is the equivalent of about 90GW of a total production of 3400 GW, or roughly 2.6% [1.6]. The development of low-cost, long-life storage systems that are also environmentally friendly will lead to increased potential, particularly for rural sub-Saharan Africa.

Energy storage systems can be classified as electrical, thermal, magnetic, chemical, potential and kinetic. The selection criteria of a particular energy storage system is based on a number of characteristics [1.6]; storage capacity, available power, depth of discharge, discharge time, efficiency, durability, autonomy, cost, self discharge, mass, control, reliability and environmental aspects. In a typical rural setting, a standard small Solar Home Systems (SHS) can operate several lights, a radio and

charge a phone. This eliminates the need for candles, kerosene, liquid, and battery charging, and provides improved indoor air quality, safety and better lighting for reading. Furthermore, savings from constant purchase of these products can be used for other productive purchases within the household. In addition, energy through powering radios and TVs can be used to send information related to health, education etc. The size of the system (typically 10 to 100 W) determines the number of hours available for a specific load. A typical rural household requires 300Wh approximately for lighting, radio, phone charging and the possibility of a using a TV.

An electromechanical battery is a simple machine which stores energy in the form of rotational motion. Advances in rotor material, power electronics, mechanical bearings and others have found the flywheel to be a viable replacement of lead acid batteries [1.6-1.8]. In addition to its predicted long life span, the flywheel is environmentally friendly as it's made of largely inert materials. The system exhibits short charge times and has an unlimited number of discharge cycles. The maintenance is simple, inexpensive and the systems are usually made compact [1.9].

However, high speed flywheel systems (for long time energy storage) require special considerations on the rotor profile design, machine parameters and power electronics. These systems require high strength materials to withstand the stresses involved. These materials are expensive and as a result various approaches were used to improve on the material usage whilst increasing on the strength of the rotor. With this in mind, the flywheel system was built on locally available materials and other commodity items. A test rig for testing the flywheel system and other system components was also designed, built and tested using locally available materials.

1.2 Brief Literature Survey

An initial literature survey was conducted to determine the evolution of the electromechanical battery and its components through the years. The origins and use of modern flywheel technology for mechanical energy storage can be traced to several hundred years ago and was further developed throughout the industrial revolution. This development was to a large extent as a result of seminal work by Dr. A. Stodola on the theoretical stress limitations of rotational disks [1.10][1.11], whose first translation to English was made in 1917.

The development of flywheel for power and vehicle applications started in the 1940s [1.12]. These systems were constructed with steel rotors, conventional bearings and only run at low speed. For example, the first commercial gyro bus was constructed in Switzerland, started operations in 1953 and ended in 1960. The bus carried a large flywheel that was spun up to 3,000 rpm by an electric motor. The gyro bus was charged at booms and this took between 30 seconds to 3 minutes. The maximum distance of the bus was 6 km with a top speed of 60 km/h.

In the 1960s and 1970s, NASA sponsored flywheel programs for space and stationary applications. However, not until the 80s and 90s with the development of high strength materials, power electronics and magnetic bearings did renewed interest in the system occur. Subsequent works by Post [1.5] [1.13], University of Austin, Beacon Power Corp [1.14] and Trinity [1.15] have seen the flywheel used for power, attitude control, vehicle and telecommunication back up applications [1.16]. Various components, configurations and designs are used to ensure proper operation of the system. For high speed operations, the rotor configuration, rotor profile, bearing, power electronics and electrical machine are of significant importance as explained further in the following sections.

Previous work in the research group at University of Cape Town investigated the use of the electromechanical flywheel to replace the lead acid battery. The system was

designed to operate at 100,000 rpm and store 300Wh using an outside rotor PM Halbach array with hybrid magnetic bearings and a heat pipe cooling system. Special emphasis was placed on implementing the Halbach array, using even and odd numbers of magnet segments. A passive control hybrid magnetic bearing system was used to levitate the machine. Two radial repelling magnetic bearings were used in combination with an axial journal bearing, like a spinning top with the precession limited by radial magnetic bearings.

An ultimate shape composite flywheel was designed to reach high speeds with high energy density. This shape incorporated the electric machine and hybrid magnetic bearing. It was operated in a vacuum, where the machine / bearing system approached efficiencies in the upper 90s. The flywheel rotor was manufactured from glass reinforced epoxy. The prototype was hand layered, in stages, to minimize the heating problem. This process was considered since the stresses are all perpendicular to the axis of rotation and in the plane of the glass layers. Previous attempts to have the flywheel made by a local manufacturer in one single piece were futile due to thermal cracking of the thick parts. The flywheel system was tested up to 120rpm achieving 1.92 J of energy. The problems encountered with this system included: vibrations, damping of the bearing system and heat evacuation with the heat pipe.

1.2.1 Flywheel Rotor Configurations

There are mainly three types of rotor configuration described, the inside-out type, integrated and the conventional design. The first configuration is the barrel or inside-out type. This design is advantageous when high strength composite fibres are used. This means the rotor can be spun to high speeds, increasing the stored energy without increasing the weight. This configuration opens avenues for the use of the Halbach array machine which can be used in high speed operation and is able to reach high efficiencies as presented in [1.13] [1.17]. The major disadvantage of this topology is the dependence of the electrical machine dimensions to the flywheel rotor design. A change in the machine dimensions requires a change in the flywheel rotor design. Further, the configuration experiences thermal problems resulting from

having an embedded machine. Using a heat pipe is a possible solution but further increases the thermal complexity in design.

The second configuration is an integrated design in which the electromagnetic and energy storage portions of the rotor are combined as presented in [1.18] [1.19] [1.20]. This type of design is not well suited for a composite rotor flywheel because of the need for electromagnetic material for torque production. The argument brought forth in this design is minimization of the weight of the containment, reduced material costs, lower mechanical complexity and reduced manufacturing costs. However, its dependency on steel for torque development in high speed operation requires high levels of safety and this is attributed to poor failure criteria of isotropic materials [1.21].

The conventional rotor design is the most common configuration as seen in [1.5] [1.22] [1.23], where most of the energy is stored in the rotor which is attached to a shaft used by the motor to spin the flywheel. The shaft connection induces problems of radial elongation differences at the interface and dynamic instability, which includes lateral and tilt mode shapes during whirl motion about the axis of rotation [1.17] [1.24]. These problems can be addressed during the prototyping and assembly as discussed in chapter 6. The advantage of this configuration is the possibility of both horizontal and vertical orientation mounting. Furthermore, the machine and flywheel can be designed independently giving flexibility in the design process.

1.2.2 Flywheel Rotor Profile

Conventional shape profiles have been used widely in rotor design as presented in [1.5] [1.16] [1.25]. However, the need to optimize on the material usage [1.26] is motivated by the high cost of high strength materials [1.13]. This is enhanced when conventional shapes are used since they utilize more material.

In [1.27], the best thickness distribution along the radius of a centrally bored flywheel is investigated. A simplified model was developed and found not to exhibit

an even stress shape for a hole radii greater than the square root of one third of the radius flywheel. Chern [1.28] investigated the optimal design of the rotating disks with the radial displacement as a prescribed value. David Eby [1.29] discussed the optimal design of elastic flywheels using injection island genetic algorithm to search for the shape variations to optimize the specific energy density. The limitation of this technique is that it's not implemented with a central hole, making it complex for the electromechanical flywheel application in this study.

This thesis considers two approaches to the derivation of an optimal shape. Firstly, the derivations of the novel shape for optimal design of the rotor based on work by Berger and Porat with a central hole [1.30]. This is done mathematically using partial differential equations theory, a piecewise differentiable disk built with four shapes. In [1.26] piecewise optimal shapes are used to create the ultimate shape. This profile exhibits exponential characteristics and is analysed numerically.

The second approach involves the use of Dr Stodola's stress solutions for isotropic material together with solutions by Timoshenko, Hartog [1.31] and Faupel [1.32] to ascertain a profile that reduces stress. A Matlab program is used to preselect the profile parameter and inertia is validated using CAD software. This profile exhibits hyperbolic characteristics.

1.2.3 Electrical Motor/Generator

This component of the flywheel is charged with converting electrical energy to mechanical energy when charging and vice versa when discharging. Various machine types have been used since 1970 to date as seen in [1.13] [1.18] [1.23] [1.33]. The operating speed of the motor/generator sets presented varies from a few hundred rpm to thousands. For this flywheel application, the choice of the machine lies in simplicity of construction, cost and consideration on the power electronics. For example, the conventional induction machines suffer high rotor losses which are undesirable in low air pressure environments.

The synchronous reluctance motor has previously been used in flywheels however acquiring a high L_d/L_q ratio during construction is complex leading to increased cost due to high VA rating requirement [1.34]. Switched reluctance motors have high torque density, are simple to construct and are cheap but use of a laminated rotor is not suitable and high strength material is necessary for this application. The homo-polar machines are not widely used for flywheel applications, however in [1.18] a machine was designed for a high speed flywheel with an efficiency of 83%.

Klaus Halbach, a scientist at Lawrence Livermore laboratory conducted research on permanent magnets for use in particle accelerators and further discovered its usage in high power, high efficiency machines called the Halbach arrays [1.35]. His paper [1.36] describes the novel approach in generating multi-pole magnetic fields arrangement of PMs. In the 90s, Post [1.13] further developed this for use in motor/generator designs. Other designs have since been built as seen in [1.13] [1.17] with efficiencies of up to 99% and 90% respectively. This particular machine exhibits high power density, low losses due to ironless stator core and a high electromagnetic field within the bore.

Permanent Magnet (PM) motors are currently the most commonly used motors for flywheel systems as seen in [1.25] [1.37-1.39]. They exhibit high efficiency and low rotor losses, however, they are temperature sensitive. This can be overcome by the use of temperature resistant magnets and evaluation of the heat flow. From investigations discussed in chapter two, an Axial Flux Permanent Magnet (AFPM) machine was selected.

1.2.4 Bearing System

The bearings are used to constrain relative motion of the flywheel system. This allows for free rotation of the system. The demand on stationary applications is less rigorous than that for mobile applications; however some of the issues that transcend both applications are dynamic load, residual balance, high speeds and the life time of the bearing system. Bearings are classified as either conventional or magnetic.

1.2.4.1 Conventional Bearings

These are contact bearings and provide support in either the axial or radial planes. The common types of these bearings are: rolling element and journal bearings. A widely used rolling element bearing type is the deep groove bearings. In this application, hybrid and energy efficient bearings were considered. These hybrid and energy efficient bearings have a higher speed capability and will provide longer service life than all-steel bearings in most applications. Other successful bearings for high speed applications are the high precision angular contact ball bearings with axial preloading. In these systems, the preloading should be adjusted to its minimum so as to minimize frictional loss, increase the speed limit and control the bearing stiffness. The major advantage of the conventional bearings is the low cost and simplicity of handling.

Conventional bearings are specifically relevant to rural applications as replacement is made easier. They ensure quick and ease of assembly making them achievable in the rural areas. With bearing manufacturers moving towards energy efficiency, more efficient contact bearings will see a further reduction in cost.

1.2.4.2 Magnetic Bearings

Magnetic bearings are non contact bearings and hence exhibit low friction, low wear and are well suited for high speed operation [1.13] [1.17] [1.23]. Magnetic bearing advantages include very low and predictable friction, ability to run without lubrication and in a vacuum. They also provide cleaner, faster and more efficient bearings at extreme temperatures [1.40]. The main disadvantages include high cost and relatively large size. There are different types of magnetic bearings currently being tested, i.e. passive magnetic bearings and the active magnetic bearings [1.10] [1.41-1.43].

The active magnetic bearings require control hardware, digital signal processors, amplifiers, digital to analog converters, analog to digital converters and software [1.41 - 1.44]. In addition, the control current of the system is proportional to the

stator rotor gap. On the other hand, the passive systems do not require any control. These bearings are constructed from PMs, electrodynamic effects, super conductors, diamagnetic materials and ferro fluids. It is difficult to build a magnetic bearing using permanent magnets due to the limitations imposed by Earnshaw's theorem, and techniques using diamagnetic materials, in the past were relatively undeveloped. Nevertheless, passive magnetic bearings exhibit advantages, that is, larger rotor-stator gaps may be possible since the current for active magnetic bearings is proportional to the square of the rotor-stator gap.

The major disadvantage of passive magnetic bearing systems is the low stiffness and damping and so in designing, sufficient stiffness and damping must be built in to allow them to perform over their entire operating range. In selecting the type of bearings to use, complexity and cost are major issues. It can be noted that passive magnetic bearings are easier to construct and are more cost effective than active magnetic bearings as they require a simpler control system.

The passive magnetic bearings have a high potential because they are economically viable, reliable and practical. Passive systems have already replaced some active magnetic bearings, predominantly in situations where, smaller sized equipment systems with large air gaps are used. Combinations of superconductor and PM bearings have been tested in flywheel applications whereby efficiencies of up to 84% have been recorded. High temperature superconducting magnetic bearings have been found to perform best, however, these require cryogenic cooling by liquid nitrogen [1.10] [1.43].

1.2.5 Power Electronics

The power electronics mainly include the drive, DC-DC converter and the control system. Brushless DC mode of operation was chosen due to its simplicity in design and operation, low cost and availability of the system components.

1.3 Research Questions and Objectives

The main research question associated with this research project is:
"Can an efficient, low cost flywheel energy storage system be manufactured with consideration given to the structural integrity of the rotor component, optimised material usage and use of locally available materials?"

This question will be addressed through detailed consideration of each of the following secondary research questions:

- What are the past and current technological trends in flywheel energy storage systems?
- Which component configurations are best suited for efficient, safe, robust low cost flywheel energy storage applications?
- Which considerations in the flywheel rotor configuration and profile in stress, modal and thermal analyses will ensure structural integrity of the complete system? This will be done analytically, numerically and experimentally.
- Which electric machine topology is best suited for this application?
- What considerations will be made to increase the energy stored in the flywheel while keeping the flywheel safe, cheap and robust?
- What test rig facility will be considered for testing the flywheel system?

The main objective of this research is to design and develop an efficient, robust flywheel system.

The specific objectives of this research include the following:

- Identifying the past and current technological trends in flywheel energy storage systems.

- Investigating the component configurations best suited for this application.
- Critically evaluating the identified flywheel rotor configurations and profile procedure for material optimisation.
- Identifying and assessing the most suitable bearing set for the flywheel system.
- Evaluating the electric machine topologies for the system.
- Prototyping and integrating the various components of the system.
- Identifying and improving on the design trade-offs encountered when integrating the complete system.
- Developing a test rig for flywheel system testing.

1.4 Justification

A comparison was carried out between the life cycle costs of the traditional lead acid battery storage system and a proposed electromechanical flywheel battery for a rural energy storage application, using two different models. The flywheel system was found to be more cost effective in the long run than the traditional lead acid battery. It was evident that small-scale flywheel energy storage has the potential to improve rural electrification problems. Integrating the flywheel system into SHSs would mean a saving of 35% per kWh with rural systems. The use of electromechanical flywheel battery storage would further mitigate the environmental problems associated with lead acid battery disposal. These systems can also be used in health centres; schools and telecommunications base stations as they fall within the power/energy range. In addition, money that would have been used on maintenance and replacement on the traditional lead acid batteries can now be used for more productive activities like education, health, food and other basic household needs hence addressing the United Nations Millennium Development Goals, which includes eradication of poverty among others.

A simulation program, HOMER (NREL, 2007) was used to validate the results. The levelized cost of energy for the system using batteries as energy storage was found to be $ USD1.611 and for the flywheel was $USD 1.368.

1.5 Structure of the Thesis

Chapter two considers the flywheel system components namely the electrical machine and the power electronics. In chapter three, analytical methods are used to develop two flywheel profiles. Chapter four analyses the prototyping of the different system components. The test rig design, prototyping and thermal analysis of the flywheel system are discussed in chapter five. The experimental results are discussed in chapter six. Conclusions and recommendations are finally drawn in chapter 7.

1.6 Concluding Remarks

This introduction chapter gives an overview of energy storage technologies. The motivation for better energy storage systems is highlighted. A brief literature is given for the various components used in the flywheel system. The main objectives this thesis seeks to answer are mentioned. The following chapters give a step by step process of how the flywheel system was designed, prototyped and tested.

1.7 References

[1.1] E. Martinot, Global status report, *Renewable,* 2007.

[1.2] International energy outlook, *DOE/EIA-0484*, June 2008.

[1.3] H. Winkler, "Renewable energy policy in South Africa: Policy options for renewable electricity," *Energy Policy,* vol. 33, pp. 27-38, 2005.

[1.4] G. Kamese, *Renewable Energies in Uganda*, March 2004.

[1.5] R. F. Post, "A New Look at an Old Idea," *Electromechanical battery Science and Technology Review*, pp. 13-19, April 1996.

[1.6] H. Ibrahim, A. Ilinca and J. Perron, "Energy storage systems—Characteristics and comparisons," *Renew Sustain Energy Rev*, *doi:10.1016/j.rser*.2007.01.023.

[1.7] J. Tzeng, R. Emerson and R. Moy, "Composite Flywheels for energy storage," *Science and Technology,* vol. 66*,* pp. 2520-2527, 2006.

[1.8] US Department of Energy, Federal Technology Alert, DOE/EE-0286, 2003.

[1.9] G. Genta, *Kinetic energy storage, Theory and practice of advanced flywheel systems*, Butterworth & Co. Ltd, 1985.

[1.10] J. G. Bitterly, "Flywheel technology, Past, Present, and 21St Century Projections," in *Proc.1997 IECEC Energy Conversion Engineering Conference*, vol.4, pp. 2312-2315.

[1.11] A. Stodola, *Steam and Gas Turbines*, McGraw-Hill Book Company, Inc, 1927.

[1.12] The Oerlikon Electrogyro, *Automobile Engineer*, pp. 559-566, Dec 1955.

[1.13] R. F. Post, T. K. Fowler and S. F. Post, "A high efficiency electromechanical battery," *Proceedings of the IEEE, 81(3)*, March 1993.

[1.14] http://www.beaconpower.com/ Last checked 20th October, 2009.

[1.15] D. Bender, R. O. Barlett, "Improved high performance flywheels," *DOE Energy Storage Systems Annual Review*, November 19-20, 2002.

[1.16] S. Ginter, G. Gisler, J. Hanks, D. Havenhill, W. Robinson and L. Spina, "Spacecraft energy storage systems," *NAECON*, 1997.

[1.17] T. M. Mulcahy, J. R. Hull, K. L. Uherka, R. G Abboud and John J Juna, "Test results of 2-kWh flywheel using passive PM and HTS bearings," IEEE *transactions on applied superconductivity, 11(1)*, March 2001.

[1.18] P.I. Tsao, "An integrated flywheel energy storage system with a homopolar Induction motor/generator and high frequency drive," Ph.D. dissertation, University of California Berkeley, 2003.

[1.19] S. Richey, "Cleansource2 battery –free energy storage: theory of operation," *Electrical energy storage systems applications and technologies (EESAT) conference proceedings*, 2002.

[1.20] P. P. Acarnley, B.C. Mecrow, J.S. Burdess, J.N. Fawcett, P.G. Dickinson and Kelly, J.G, "An integrated flywheel/machine energy store for road vehicles," *IEE In colloquium on new topologies for permanent magnet machines,* vol. 090, pp. 1-6, August 2002.

[1.21] J. Widmer, P. V. Burg, Failure of tangentially wound composite energy storage flywheels, unpublished.

[1.22] K. Murakami, M. Komori, H. Mitsuda and A. Inoue, "Design of an energy storage flywheel system using permanent magnet bearing (PMB) and superconducting magnetic bearing (SMB)," *Cryogenics,* vol. 47, pp. 272-277, 2007.

[1.23] G. G. Sotelo, R.D. Andrade Jr, Antonio Carlos Ferreira, "Magnetic bearing sets for a flywheel system," *IEEE transactions on applied superconductivity,* vol.17 (2), June 2007.

[1.24] F.J.M. Thoolen, "Development of an Advanced High speed Flywheel for Energy Storage System," Ph.D. dissertaion, Eindhoven University of Technology, 1993.

[1.25] F.N. Werfel, U. Floegel-Delor, T. Riedel, R. Rothfeld, D. Wippich, B. Goebel, G. Reiner, and N. Wehlau, "A compact HTS 5 kWh/250 kW flywheel energy storage system," *IEEE transactions on applied superconductivity,* vol. 17(2), June 2007.

[1.26] M. Berger and I. Porat, *Optimal design of rotating disk for kinetic energy storage*, Faculty of mechanical engineering, Technikon-Israel institute of technology, Haifa Israel.

[1.27] G.R Kress, Struct Multidisc potim, vol. 19, pp. 74-81, 2000.

[1.28] J.M Chern, W. Prager, "Optimal design of rotating disk for given radial displacement of edge," *Journal of Optimization Theory and Applications*, vol. 6, no 2, 1970.

[1.29] D. Eby, R.C Averill, E. Goodman, and W. Punch, "An injection island GA for flywheel design optimization," Artificial Intelligence in Engineering , Design, Analysis and Manufacturing, vol. 13, pp. 389-402. 1999.

[1.30] D. Johnson, "Design Considerations and Implementation of an Electromechanical Battery System," Ph.D. dissertation, University of Cape Town, 2008.

[1.31] D. Hartog, J. Pieter, *Advanced strength of materials*, Network McGraw-hill, 1952.

[1.32] J.H. Faupel, F.E Fischer, *Engineering design, a synthesis of stress analysis and materials engineering*, 1st edition. New York: Wiley; 1964.

[1.33] S. Samineni, B. K. Johnson, H. L. Hess and J. D. Law, "Modelling and analysis of a flywheel energy storage system for voltage Sag correction," *IEEE Transactions on Industry Applications,* vol. 42(1), February 2006.

[1.34] H. Hofmann, Sr. Sanders, "High speed synchronous reluctance machine with minimized rotor losses," *IEEE transactions on industry applications,* vol. 36, pp. 531-539, 2000.

[1.35] B.T. Merritt, R.F. Post, G.R. Dreifuesrt, D.A. Bender, "Halbach array motor/generator. A novel generalized electric machine," *Halbach festschrift symposium, Berkeley, California*, February 3, 1995.

[1.36] K. Halbach, Design of permanent multi-pole magnets with oriented rare earth cobalt material.

[1.37] D. A. Bender and P.K. Snyder. DC power management with a high performance flywheel, in *Proc. Electrical Energy Storage Systems Applications and Technologies (EESAT)*, 2002.

[1.38] R. Hockney and C. Driscoll, Powering of standby power supplies using flywheel energy storage, *International-Telecommunications-Energy-Conference (INTELEC),* pp. 105–109, 1997,.

[1.39] R. Wagner and R. Jansen, Flywheel technology development at the NASA

Glenn research Centre, *Electrical Energy Storage Systems Applications and Technologies (EESAT) Conference Proceedings*, 2002.

[1.40] M. A. Arslan, Flywheel geometry design for improved energy storage using finite element analysis, *Materials and design*, 2007.

[1.41] B. Bolund, H. Bernhoff, M. Leijon, "Flywheel energy and power storage systems," *Renewable and Sustainable Energy Reviews,* Vol. 11, pp. 235–258, 2007.

[1.42] M. Siebert, "Passive magnetic bearing development," *University of Toledo, NASAGlenn Mechanical components branch*, May 14 2002.

[1.43] J. Hillyard, Magnetic Bearings, Technische *Universität München*, Joint Advanced Student School, 2006.

[1.44] G. Schweitzer, Active magnetic bearings - chances and limitations, *International Centre for Magnetic Bearings, ETH Zurich*, CH-8092 Zurich,

Chapter 2

System Description and Components

This chapter gives a brief system description. A machine topology selection and design is described. The power electronics for the control of the system is also given.

2.1 System Description

The flywheel energy storage system consists of a flywheel rotor coupled to a three phase AFPM machine. The flywheel rotor provides the required inertia to store the designed energy and the electrical machine is charged with the energy conversion in the system. The machine is powered through a 100A rectifier dc supply via a three phase bidirectional inverter driven by PWM switching from control desk as shown in Fig.2.1.

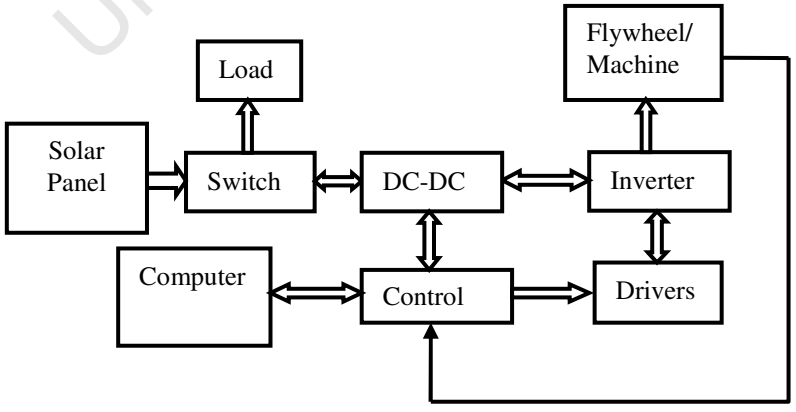

Figure 2.1: General schematic of flywheel system

The control of the system is determined by the rotor position of the magnets given by the hall sensor magnets and the PWM switching of the inverter switches. Details of this control strategy are given in section 2.3.

The amount of energy in the system increases exponentially with speed hence the need to have a high operating speed limit. This is illustrated in equation (2.1). In principle, the amount of energy stored in a flywheel is given by [2.1].

$$E = \frac{1}{2} J \omega^2 \tag{2.1}$$

Where J is the moment of inertia and ω is the rotational speed of the flywheel rotor

The designed operating speed range is 8,000 rpm to 25,000 rpm. During motor mode, the flywheel system is ramped to its maximum designed speed when the PV panel (dc source) transfers energy to the machine. During generator mode, the supply is switched off, a load is connected as shown in Fig. 2.1. This in turn absorbs energy from the flywheel hence reducing its speed. For the case when no load is connected, the speed drops due to the rotational losses. As the voltage magnitude and frequency of the machine are directly proportional to the speed of rotation, a DC-DC converter is required to ensure constant voltage at the load side. However, in the final system, the DC-DC converter was neglected and the load was supplied directly.

The ability of a flywheel to reach high speeds is mainly dependent on the maximum strength of the material, which is given by equation (2.2) below [2.1].

$$\sigma = \rho r^2 \omega^2 \tag{2.2}$$

Where σ is the ultimate tensile strength of the rotor material, ρ is the density of the flywheel rotor material, r is the radius of the flywheel rotor and ω is the rotational speed of the flywheel.

In addition, the energy density of a rotor at burst speed is dependent only on the flywheel design and the characteristics of the material [2.1] as shown in equation (2.3) below.

$$\left(\frac{e}{m}\right) = K\frac{\sigma}{\rho} \tag{2.3}$$

Where $\left(\frac{e}{m}\right)$ is the energy density and K is the shape factor

From equation (2.3) it can be seen that the energy stored is proportional to the strength of the material. In fact, structural integrity is by far the biggest challenge to this technology.

For improved safety, the system is contained in a thick steel cylinder with reduced air pressure to reduce windage losses. In this design, the windage loss is ignored due to its low magnitude.

2.2 Permanent Magnet Machines

The machine is charged with converting electrical energy to mechanical energy and vice versa when discharging. In this thesis, the major driving factors of choice for the electrical machine are; low cost, simple control, high torque and high power density. In addition, a good thermal behaviour and simple construction of the machine is essential. Section 1.2.3 described the various machines that can be used for flywheel operation and these include induction machines, switched reluctance and Halbach machines [2.2] [2.3]. The characteristics in relation to the high speed

operation were also discussed and the PM machines were found to be more suitable for this design due to their high torque density, high power density, high efficiency and low rotor losses.

PM machines are widely used for automation and industry applications as a result of advancement in PM technology. These machines are highly efficient, exhibit high torque and power densities and can be used for high speed applications [2.4] [2.5]. The conventional Radial Flux Permanent Magnet (RFPM) machine has been used for decades and it has one rotor and stator just like the conventional Axial Flux Permanent Magnet (AFPM) machine. As shown in Fig. 2.2, the RFPM machine has an external stator and internal rotor with either surface mounted or interior magnets.

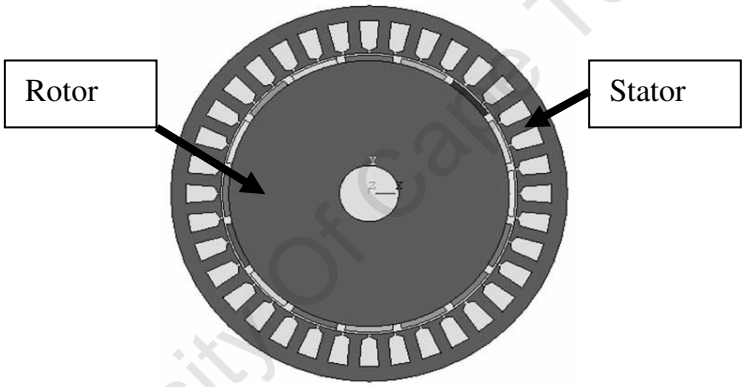

Figure 2.2: Inner rotor radial flux machine

These machines are extensively used for industrial applications and have higher torque than the conventional induction machines [2.6]. The RFPM can be constructed with either a slotted or non-slotted stator. The major disadvantage of this machine is that only the windings facing the rotor PMs are used for torque production. In addition, this machine topology is considered to have long end windings on the other side of stator which means increased copper loss. This topology also has a large air gap which results in reduced flux density. However, this topology has a great thermal transfer capability giving a relatively high machine electrical loading.

Alternatively, the conventional AFPM machines have been seen as an alternative to conventional RFPM machines in domestic and naval applications [2.6]. The advantages of the conventional AFPM machine over the conventional RFPM machine include; higher power to weight ratio, compactness and hence can be used in space limited applications. They also have planar and adjustable air gaps. The major disadvantage of this machine is the machine structure can easily be twisted by the large axial forces exerted on the stator. The similarity with these machines is that they can be constructed with multiple rotors and stators as shown in Fig. 2.3 and 2.4.

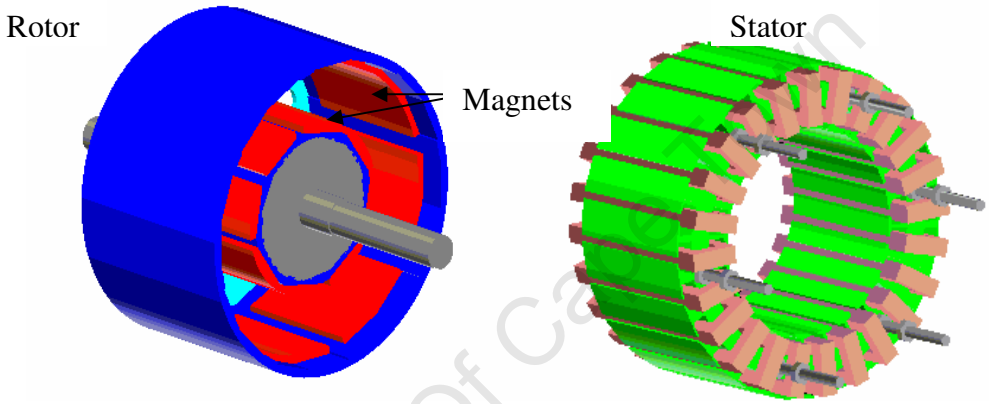

Figure 2.3: Double rotor machine topology [Source: Lipo]

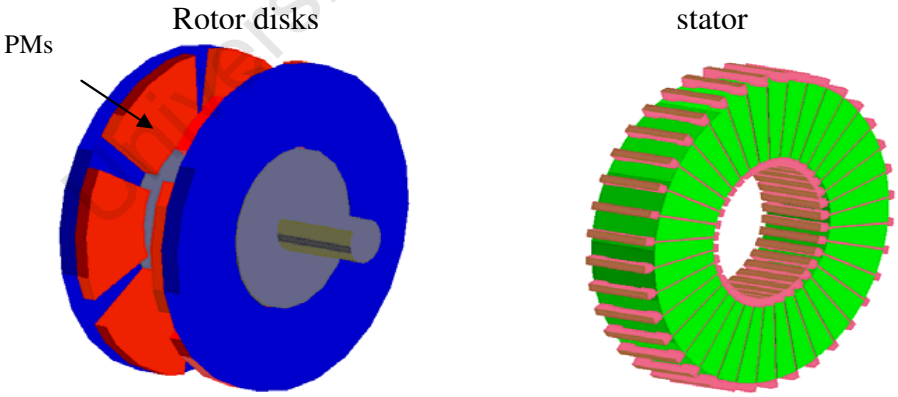

Figure 2.4: Double rotor axial flux machine [Source: Lipo]

The two major disadvantages can be eliminated by introducing a second stator to the machine. These machines have been investigated and found to increase the torque density as well as the efficiency of the machine.

According to Qu [2.7], the RFPM and AFPM machines exhibit similar performance in torque density, torque-to-mass ratio, losses and efficiency although the material cost of the AFPM are higher than those of the RFPM. In addition to stronger cooling capabilities in the AFPM machine, the ratio of the length to diameter can be optimized for various applications as compared to the RFPM whose ratio is constant hence limiting applications. On the contrary, the optimization of the RFPM topology is more complex as the resultant two air gaps are associated with two different electric loadings. The flat profile of the AFPM topology is desirable as it adds less to the volume of the flywheel container. Most importantly, the AFPM is a compact machine making its use in flywheel systems quite desirable.

2.3 Axial-Flux Permanent Magnet Machine

This machine can be designed with various types of topologies, ranging from the number of disks used, armature slots to location of magnets (surface mounted or buried). The choice of which topology to use is dependent on the application. The selection of the parameters is very important, that is, torque, power density and cost should be outlined and the topology selected from these aspects. This AFPM machine exhibits high torque output, high power density, is maintenance free, among others [2.8]. As compared to other machines, there are various advantages and disadvantages to the AFPM.

The major advantages of the AFPM are:

- Compact machine construction and short frame
- High power density
- High efficiency, no rotor copper losses due to permanent magnet excitation
- Have a short rotor in axial direction and it can be constructed without steel
- More robust structure than cylindrical type

The major disadvantages of the AFPM are:

- High windage losses at high speed applications which may be minimised by operating in a vacuum.
- Complicated machine topology with two air gaps

2.3.1 Different Combinations of AFPM

The different configurations for the AFPM can best be expressed in the Fig. 2.5 below.

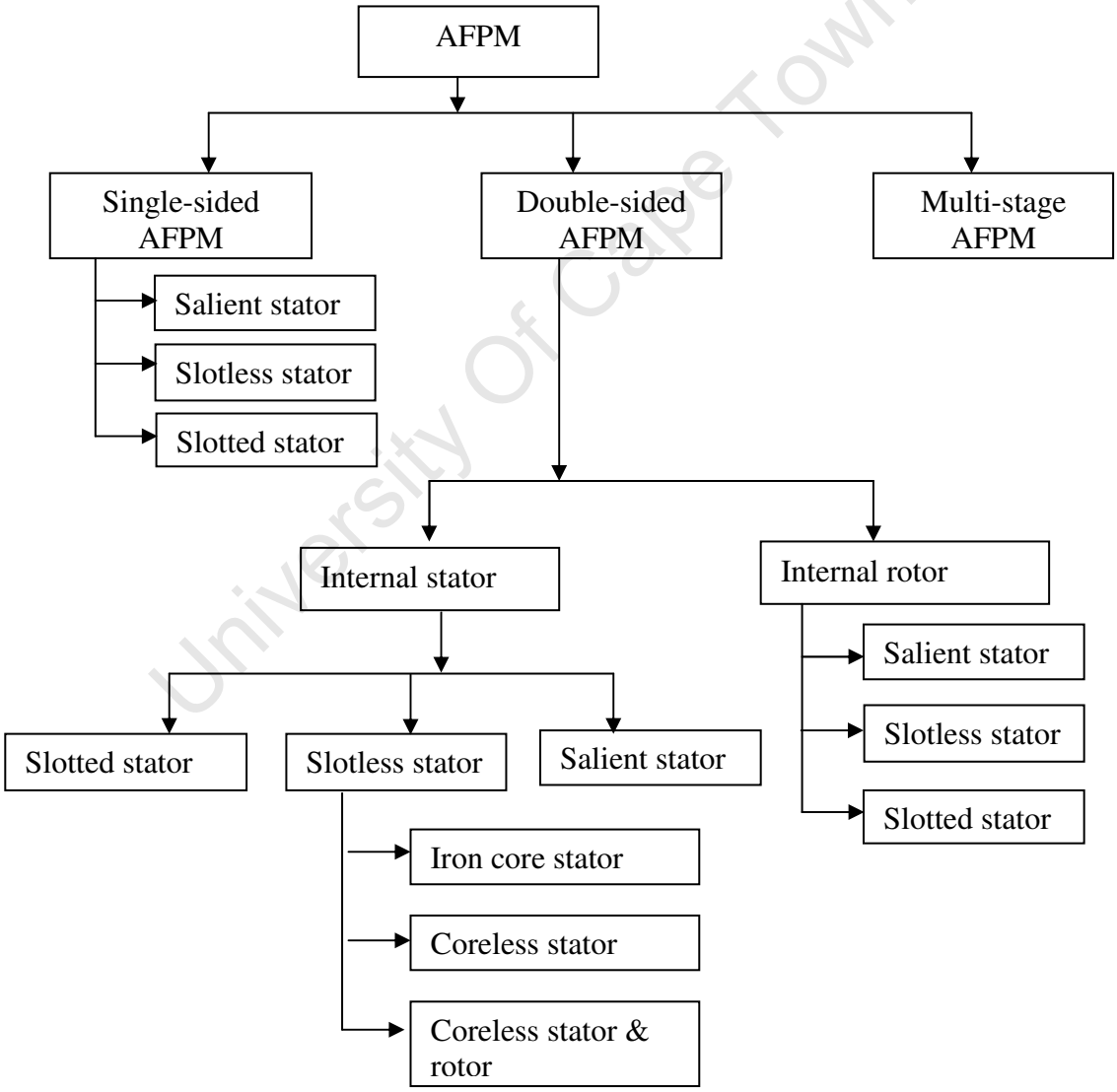

Figure 2.5: AFPM configuration combinations

2.3.1.1 Stator-Rotor Arrangement

The AFPM structure can be arranged as single-sided, double-sided or multi-disk. The choice of the structure depends on the application, cost and volume available for the machine. The single sided structure [2.9] [2.10] is the cheapest although it suffers from high attractive forces [2.11] and requires a thicker rotor disk. Two techniques are used in chapter 4 to handle the attractive forces. The double-sided arrangement can be used to resolve the problem [2.12] and this can be configured with an internal or external stator. The internal stator, that is, one stator-two rotors [2.13] ensures better utilization of the copper hence improving the efficiency and power density.

The reduced cost of the single sided structure makes it attractive for the flywheel application but this structure does not have good utilization of the copper. Furthermore, the double stator also has long end windings thus increasing the copper and iron losses, however this is good for cooling. The double rotor fully utilises the copper used. The rotor disk frames act as fans but this increases the windage and frictional losses. On the other hand, in multi-disc topologies, the mechanical stresses and windage losses are higher and costly due to the large number of PM used.

2.3.1.2 Type of Mounting

The choice between the two types of mountings is based on the simplicity of construction and the ability to withstand high centrifugal forces. The buried type mounting offers better protection from centrifugal forces however this is more complex to construct as compared to the surface mounted magnets. This can be made easier by slicing a small section of the iron to embed the magnets and also applying glue with nickel coating to improve the ruggedness of the magnet attachment. From an electrical point of view, the effective air gap of the surface mount is larger because the permeance of magnets nears that of the air gap. This lowers the inductance of the stator windings limiting the operation of the machine above its base speed.

2.3.1.3 Armature Slots

AFPM machines can be constructed with or without armature slots. A machine with armature slots is more robust than the slotless machine. In addition, the effective air gap is much smaller. However, because of the stator slots, the machine exhibits flux ripple, tooth iron losses, tooth saturation and tooth related vibrations which are eliminated when using the slotless armature. In contrast, the slotless stator is not suitable for applications where the machine is subjected to excessive mechanical stress. This can be minimised by applying resin over the windings. In addition, the copper losses are minimized as this topology has relatively short end windings.

2.3.1.4 Topology Selection for AFPM

The AFPM can either be constructed as a NN or NS machine as shown in Fig. 2.6 (a,b) below. Each configuration exhibits both advantages and disadvantages.

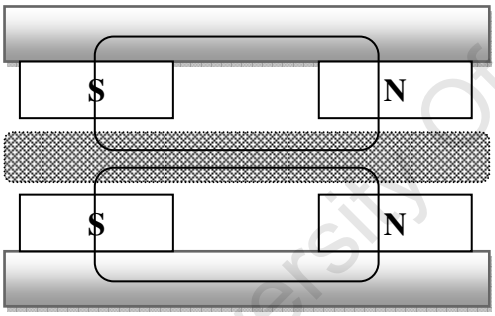

Figure 2.6a: NN configuration

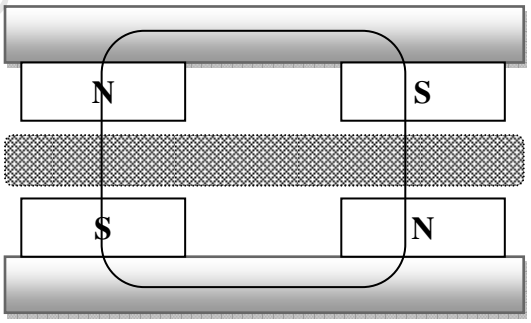

Figure 2.6b: NS configuration

The flux path of the NS passes through the stator and does not pass circumferentially making the axial length shorter. This characteristic makes the NS less heavy than the NN weight. It also ensures less iron and hence higher efficiency. In addition, the NS can be manufactured with no core for small power machines.

In coreless stator, the hysteresis and eddy current losses do not exist and the rotor steel losses are negligible ensuring higher efficiencies with zero cogging torque, however, hysteresis loss may occur at high frequency [2.14].

2.3.2 Comparison of the Permanent magnet Brushless AC and DC Machine

According to [2.9], AFPM machines can be classified as either a brushless AC or DC machine. The brushless AC also known as the permanent magnet synchronous machine is characterised by:

- Sinusoidal or quasi-sinusoidal distribution of the magnet flux in the airgap
- Sinusoidal or quasi sinusoidal current waveforms
- Quasi-sinusoidal distribution of stator conductors

Brushless DC machines (BLDC) contains most of the characteristics of PMAC motors. They are generally designed as surface-mounted motors with concentrated windings on the stator. With the appropriate placement of the PM on the rotor, a trapezoidal back-EMF shape is obtained.
The brushless DC machines are characterised by:

- Rectangular distribution of the magnet flux in the airgap
- Trapezoidal current waveforms
- Concentrated stator winding

These machines are similar in nature and only differ when choice for a specific application has to be made. According to [2.9] there is no significant torque density difference between these machines. The AC machine is considered to be more efficient and produces a smoother torque at higher speeds. Torque of square wave machines decreases at high speed or with low supply voltage because of the distortion of the phase current.

However, the sine wave machines need a high precision and expensive position transducers. The control of sine wave machines is more complicated and the converter switching losses are higher in sine wave operation.

2.3.3 Mathematical Model of the BLDC

The mathematical model of the BLDC is presented with the underlying assumptions:

- The motor windings have a constant resistance, self inductance and mutual inductance.
- All the three phases have identical back EMF shapes
- Power semi conductor devices in the inverter are ideal

The BLDC is represented by three phases resulting in the total sum of the currents being equal to zero. The designed machine is surface mounted and hence no saliency such that the stator self inductances are independent of the rotor position. This means that the self inductances are equal. Under balanced three phase conditions, all three phases are equal as in equation (2.4).

$$r_s = r_a = r_b = r_c \tag{2.4}$$

The matrix that describes the model is hence given by equation (2.5).

$$\begin{bmatrix} V_a \\ V_b \\ V_c \end{bmatrix} = \begin{bmatrix} r_s & 0 & 0 \\ 0 & r_s & 0 \\ 0 & 0 & r_s \end{bmatrix} \begin{bmatrix} i_a \\ i_b \\ i_c \end{bmatrix} + \left[\begin{bmatrix} L-M & 0 & 0 \\ 0 & L-M & 0 \\ 0 & 0 & L-M \end{bmatrix} \frac{d}{dt} \begin{bmatrix} i_a \\ i_b \\ i_c \end{bmatrix} \right] + \begin{bmatrix} e_a \\ e_b \\ e_c \end{bmatrix} \tag{2.5}$$

The back EMF waveforms are trapezoidal in nature and can be represented by either Fourier series or Laplace transforms. The BLDC voltage equation originates from the voltage equation of the Brush DC motor given by equation (2.6).

$$V(t) = r_a i_a(t) + k_e \omega_m(t) + L_a \frac{di_a(t)}{dt} \tag{2.6}$$

This results into

$$\frac{di_a(t)}{dt} = \frac{v(t)}{L_a} - \frac{r_a}{L_a} i_a(t) - \frac{E(t)}{L_a} \tag{2.7}$$

The electromechanical torque T_{em} is linearly proportional to the armature current i_a and expressed as

$$T_{em} = k_T i_a \tag{2.8}$$

The resultant solution gives the motion equation in Laplace form as:

$$T_{em} = \frac{k_T V(s) - k_e \Omega_{rm}}{r_a + sL_a} \tag{2.9}$$

2.3.4 Mechanical Design Considerations

There are various mechanical design considerations in AFPM design. In the first instance, the integration of the rotor disc and shaft is significant especially for high speed operation. Any imbalance could cause deterioration in the performance of the machine component, vibrations and reduce the life time of the system. The different radial expansions of the shaft and discs means the joint needs to be well designed and the fabrication done properly. In addition, a uniform air gap of a double sided AFPM is complex to achieve. This is further reduced if the attractive forces are not catered for as the discs will tend to attract. In the analysis, the impact of the attractive forces is compensated using a fixed pressure load on the system.

Of great importance for high speed design is the maximum radius of the rotor discs. The major limitation is the strength of the back iron and the maximum strain. In this design, the thickness of the back iron was fixed as well as the pressure due to the attractive forces. Ideally, a smaller disc would reduce the stress and strain components on the disc at high speeds; however the small diameter means smaller areas for the stator windings. This results in lower torque in the machine and lower cooling capability. Enlarging the discs has an impact on rotor dynamics and mechanical integrity of disc-shaft joint.

To establish the maximum stress on the rotor disk, equation (2.10) is used as shown [2.14].

$$\sigma_{\max} = \frac{3+\upsilon}{8}\left[\frac{\rho}{g \times 39.87}\right]\left[\frac{2\pi\omega}{60}\right]^2 \left(r_o^2 - r_i^2\right) \tag{2.10}$$

Where σ_{max} is the maximum allowable stress, υ is the poison's ratio, ρ is the density of the material, ω is the rotational speed, r_o^2 and r_i^2 are the outer and inner radius respectively.

In [2.14], the normal attractive force between parallel discs with magnets is given by equation (2.11) and this was used to ascertain the fixed pressure between the disks.

$$F_z = \frac{1}{2}\frac{B_{mg}^2}{\mu_o} S_{PM} \tag{2.11}$$

The numerical package ANSYS is used to determine the maximum stress and strain at the maximum operating speed range of 25,000 rpm. The stresses on the rotor discs with magnets are much lower than the maximum allowable stresses for the steel used.

2.3.5 Electrical Considerations

This section introduces the electrical considerations of the designed machine. The major aspects are the excitation voltage, power and developed torque.

2.3.5.1 Back EMF

The back EMF induced in the stator winding of an axial flux BLDC PM Machine is given by:

$$E_{ph} = k_e n \tag{2.12}$$

Where n is the speed and k_e is the armature voltage constant, given by:

$$k_e = \frac{\pi}{2}\sqrt{2}pN_{ph}\phi k_w \tag{2.13}$$

Where p is the number of poles, N_{ph} is the number of phases, Φ is the flux and k_w is the winding factor.

2.3.5.2 Developed Torque

The developed torque is derived from the apparent electromagnetic power induced in the stator winding which is given by:

$$T_d = \frac{S_{em}\cos\psi}{2\pi n_s} \tag{2.14}$$

But the apparent electromagnetic power is given by equation (2.15)

$$S_{em} = \pi^2 k_D k_w n_s B_{mg} A_m D_{out}^3 \tag{2.15}$$

Hence

$$T_d = \frac{\pi}{2} k_D k_w D_{out}^3 B_{mg} A_m Cos\psi \tag{2.16}$$

Where T_d is the developed torque, k_D is a function of the ratio of outer to inner diameter of the stator, k_w is the winding factor, D_{out} is the outer diameter of the stator, B_{mg} is the magnetic flux, A_m is the magnetic area and Cosψ is the power factor.

2.3.6 Stator Windings Design

A BLDC machine was selected with a coreless stator. The material selection for the stator holding structure is vital. A high strength and thermal conductivity material is required for this purpose. The tooth saturation and core losses are neglected for this topology. The essential parameter for maximising the flux linkage is the inner to outer ratio of the stator diameter which is kept at 1.73. A low value of the electric loading is considered to ensure better thermal performance of the machine. Two machines were designed and the design procedure is explained as follows.

The number of turns and diameter of the conductor of the electrical machine is given by equations (2.17) and (2.18) respectively.

$$A = \frac{2\left(N_{ph} m I_{rms}\right)}{\pi D} \tag{2.17}$$

$$D_{cond} = \sqrt{\left(\frac{8 m N_{ph} I_{rms}}{A \pi^2 D}\right)} \tag{2.18}$$

Where N_{ph} is the number of turns per phase, A is the electric loading, m is the number of phases, D is the average diameter of the stator, I_{rms} is the rms current.

The slot area and depth are given by equations (2.19) and (2.20).

$$A_{slot} = \frac{A_{cond} N_{ph}}{N_c S_{fil}} \tag{2.19}$$

$$S_{depth} = \frac{A_{slot}}{S_{width}} \tag{2.20}$$

Where A_{cond} is the conductor area, N_{ph} is the number of phases, N_c is the number of coils per phase and S_{fil} is the slot fill factor.

The design parameters of the stator windings are calculated based on the analytical equations given in section 2.2.7. The two machines are, a 100W machine rated at 12V and a 500W machine rated at 150V. Table 2.1 shows the design parameters.

Table 2.1: Stator winding parameters

Design parameters	100 W Machine	500W Machine
Number of poles	4	4
Inner/outer diameter	64mm/80mm	80mm/150mm
Axial length	23mm	26mm
Airgap	2mm	2mm
Electric loading	10,000A/m	15,000A/m
Current density	$4A/mm^2$	$6A/mm^2$
Conductor gauge	18AWG	17AWG
Number of turns per phase	32	32
Magnetic loading	0.47T	0.7T
Magnet thickness	8.5mm	10mm
Remnant flux density	1.2T	1.35T
Back iron thickness	9mm	10mm

2.3.7 Armature Reaction

This refers to the magnetic field produced when currents flowing in the stator which distort the field flux created by the PMs. This reduces the flux density in the air gap. Armature reaction in PM machines can cause partial or full demagnetization of the magnets. In surface mounted BLDC machines, the magnets present low permeability to the impressed MMF hence the distortion is weak. However, for the buried magnet, the protruding iron presents a high permeability causing high distortion in the field [2.15]. The rotor disc introduces saturation in the magnetic material hence the need for a non linear analysis. The topology selected introduces a large air gap and high energy magnets.

2.4 BLDC Machine Losses

The losses were investigated to estimate the efficiency of the machine component and to observe the thermal behaviour of the machine. The total losses in the machine include the copper losses, iron losses, mechanical losses and stray losses.

Distribution of the stator windings, short pitching of the windings and magnet skewing reduce higher order winding and slot harmonics but reduce torque. High speed machines tend to generate very high windage losses hence the need to reduce the air pressure in the containment. This reduction in the air pressure brings about a decreased heat transfer which results in rise in magnet and rotor temperature.

2.4.1 Copper Loss

This is referred to as the I^2R loss and contributes to the total machine loss. It is mainly a function of the loading and the stator winding resistance. Minimizing the copper losses requires shortening the end windings. Concentrated windings are used and connected in series with each coil.

The copper loss for the BLDC is expressed as:

$$P_{cu} = 2I_{DC}{}^2 R \tag{2.21}$$

Where I_{DC} is the rms current and R is the stator winding resistance.
Temperature correction of the stator winding resistance is given as

$$R_T = R_{20}\left[1 + 0.00393\left(T - T_{20}\right)\right] \tag{2.22}$$

Where R_{20} is the resistance at 20°C and T is the temperature of the resistance measurement.

2.4.2 Core Loss

This is significant at very high speeds however the topology selected avoids the use of a core using a NS configuration.

2.4.3 Eddy Current Loss

In high speed operation of the machine, there is a rapid variation of the flux density within the stator windings, which results in induced eddy currents in the windings. A finite element aided model is used to predict winding eddy current losses [2.16]. This incorporates the static equation with flux densities obtained from finite element simulations and is expressed as:

$$P_e = \frac{\pi^2 \sigma}{4\rho} f^2 d^2 m_{con} \left[B_{mx}^2 + B_{my}^2\right] \eta_d^2 \tag{2.23}$$

Where σ is the conductivity of the winding material, ρ is the density of the winding material, f is the frequency, d is the diameter of the conductor, m_{con} is the mass of the conductor, B_{mx} and B_{my} are the x and y components of the flux density respectively.

The harmonic factor η_d is expressed as [2.16]

$$\eta_d = \sqrt{1 + \frac{(3B_x)^2 + (3B_y)^2}{B_{x1}^2 + B_{y1}^2} + \frac{(5B_x)^2 + (5B_y)^2}{B_{x1}^2 + B_{y1}^2} + ...} \tag{2.24}$$

Where B_{x1} and B_{y1} are the *x* and *y* components of the flux density for the first and second harmonic respectively.

The mechanical losses of the machine are combined with the flywheel windage loss and presented in chapter 5.

2.5 Power Electronics

The power electronics in the flywheel system control the energy conversion process. The designed power electronics include a DC-DC converter and BLDC drive. The BLDC drive ensures that the MMF frequency of the stator is in synchronism with the position of the rotor's magnetic field. The back EMF generated by the machine is dependent upon speed, therefore a DC-DC converter ensures that the voltage at the consumer output is maintained at reference voltage, irrespective of the system mode of operation. For the purpose of this thesis, the solar panel side of the DC-DC converter shall be referred to as the input and the flywheel side of the converter shall be referred to as the output of the converter. Preliminary work by Dave Johnson [2.17] on BLDC and further analysis of the drive and DC-DC converter by Mac Stuart [2.18] and Paul Barendse made this section of the thesis possible. Their contributions to this section well appreciated. The topology considered in the work is shown in Fig. 2.7.

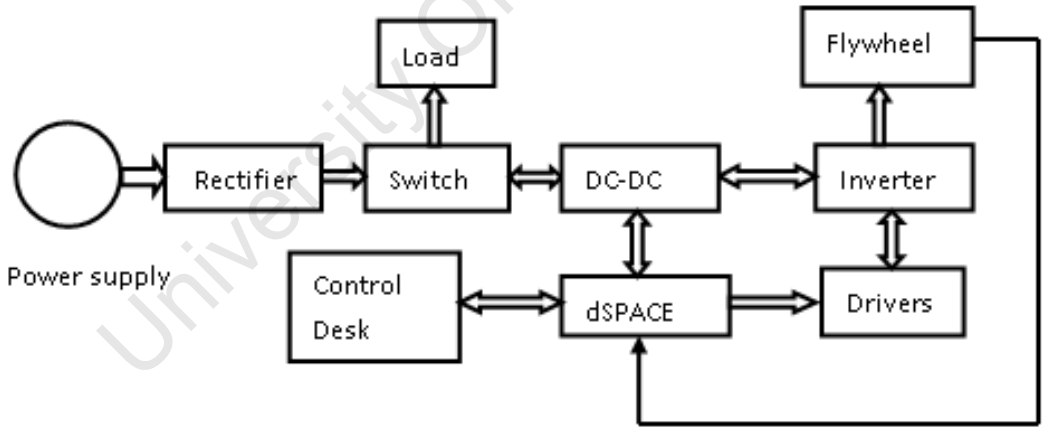

Figure 2.7: General schematic of the power electronics

2.6 Operating Modes

The purpose of the control system is to process the flow of power while ensuring the current is maintained below its rated value. The above flywheel system has been designed such that the BLDC machine has a back EMF of approximately 12V at the nominal operating point of 8 000 rpm and a back EMF of approximately 36V at a maximum speed of 25,000 rpm.

The control strategy of the flywheel system can be split into 4 different modes of operation:

- Flywheel start-up mode of operation
- Motoring mode of operation
- Generating mode of operation
- Free spinning mode of operation

2.6.1 Flywheel Start Up Mode of Operation

When the flywheel accelerates from 0 rpm to 8,000 rpm the output voltage increases from 0V to 12V, while the input voltage remains at 12V. During this phase the DC-DC converter operates in current control mode, ensuring the current does not surpass the rated value of the machine, 10A. The need for current limiting arises due to the low stator impedance within this low speed range. As the motor spins at low speeds, the back EMF is small resulting in a high potential difference across the small stator impedance. This results in high stator currents and potential motor burn out. When the flywheel reaches 8,000 rpm, the controller will switch from this mode of operation into the motoring mode of operation.

2.6.2 Motoring Mode of Operation

The flywheel will be in this mode of operation whenever the input voltage is above the low voltage threshold of 11V and the flywheel speed is above 8,000 rpm. During

this mode the DC-DC converter will transfer power from the solar panels to the flywheel, while the speed is ramped from 8000 rpm to 24000 rpm and the power is limited to its rated value.

2.6.3 Generating Mode of Operation

The flywheel will be in this mode of operation whenever the input voltage is below the low voltage threshold of 11V and the flywheel speed is above 8,000 rpm. The DC-DC converter will transfer power from the flywheel to the load, since the BLDC machine will be operating as a generator. The DC-DC converter will try and maintain the input voltage at 12V. This will be achieved by bucking the voltage produced by the generator down to 12V.

2.6.4 Free Spinning Mode of Operation

The flywheel will be in this mode whenever the input voltage is below the low voltage threshold of 11V and the flywheel speed is below 8,000 rpm. The DC-DC converter will be switched off, to prevent power from continuing to be drawn from the flywheel. The motor will still slowly run down due to frictional and windage losses.

2.7 DC-DC Converter

The interface between the BLDC drive and the consumer-end, takes the form of a DC-DC converter. Assuming that the solar panel provides the necessary 12V at start up, the current flowing to the motor will need to be limited. This is achieved by limiting the DC motor voltage; hence a buck mode DC-DC converter is required, since the output voltage range during this mode is between 0V and 12V. While the flywheel is accelerating from its nominal operating point, 8000 rpm to its maximum speed, the voltage needs to be increased above its input voltage of 12V; therefore a boost converter is required, whereby the output voltage range varies between 12V and 36V. During this mode, the power is limited by the converter. In these two

modes of operation, power is transferred from the solar panel to the flywheel, however the DC-DC converter also requires power to be transferred in the opposite direction when generating. In this mode the speed of the machine is between 8000 rpm and 24000 rpm, providing a voltage range of between 12V to 36V at the terminals of the BLDC. The voltage at the user-end needs to be maintained at 12V; therefore a buck converter with necessary voltage control is required.

In order for power to flow in both directions, from solar panel to the flywheel system during the charging of the electromechanical battery and from the electromechanical battery to the user, a bidirectional DC-DC converter needs is required.

2.7.1 DC-DC Converter Topologies

A buck converter works in such a way that the average output voltage is lower than the input voltage.

The average output voltage is given by [2.19]:

$$\frac{V_{out}}{V_{in}} = D \tag{2.25}$$

Where V_{in} is the input voltage to the converter, V_{out} is the output voltage from the converter and D is the duty ratio.

This topology, as shown in Fig. 2.8, works by varying the ratio of the time that the switch is on to the time that the switch is off (the duty cycle/ratio). The inductor and the capacitor at the output stage act as current and voltage filters respectively. This converter is a linear converter as the output voltage varies linearly with respect to changes in the duty cycle.

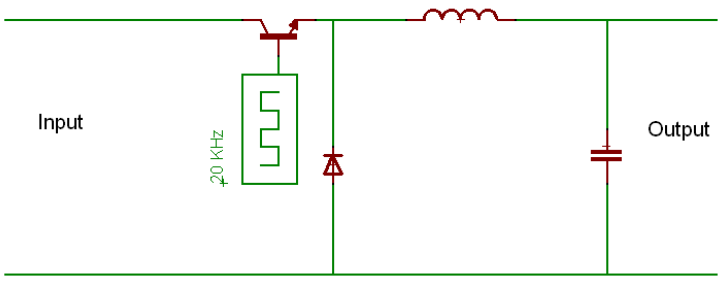

Figure 2.8: Buck Converter

This converter topology acts as a fundamental building block in numerous DC-DC converter topologies. The second topology examined is that of a boost converter, as shown in Fig. 2.9. A boost converter works in such a way that the average output voltage is higher than the average input voltage. When the switch is turned on, the input supplies energy to the inductor as the diode is reverse biased and the output stage is isolated. When the switch is turned off, the energy stored in the inductor flows to the output stage. Additionally, energy flows from the input stage to the output stage. This energy stored in the inductor boosts the output voltage above the input voltage.

The average output voltage is given by [2.19]:

$$\frac{V_{out}}{V_{in}} = \frac{1}{1-D} \tag{2.26}$$

Where V_{in} is the input voltage to the converter, V_{out} is the output voltage from the converter and D is the duty ratio.

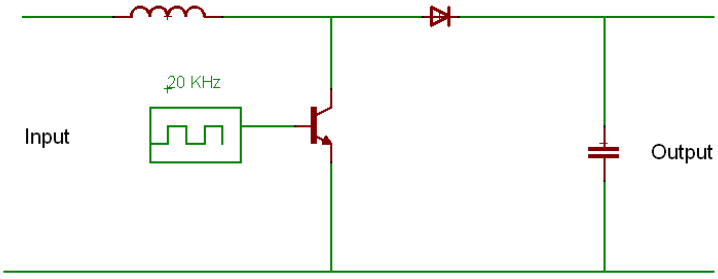

Figure 2.9: Boost Converter

The ideal gain of 1/(1-D) is not realizable as the duty ratio gets close to 1. This is because of the parasitic losses associated with the inductor, the capacitor and the diode. These losses put an upper bound on the step up ratio that a boost stage can achieve. This drop off in the available gain is shown in Fig. 2.10.

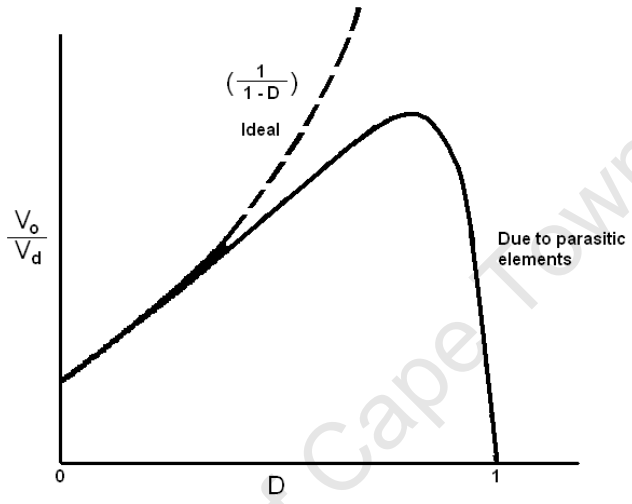

Figure 2.10: Voltage gain curve for boost converter

The third topology is a combination of the buck and boost converter, known as a buck-boost converter. There are numerous circuit configurations available in literature for the buck-boost converter topology. A number of these converters are analysed below.

The tapped inductor converter is one which uses a tapped inductor (auto transformer) to increase the input to output gain ratios. The proposed converter is shown in Fig. 2.11. The converter is both bi-directional and can either buck or boost the input voltage depending on the requirements. The advantage of this configuration is that it only consists of 2 switching devices, resulting in fewer components and a simplified control circuit.

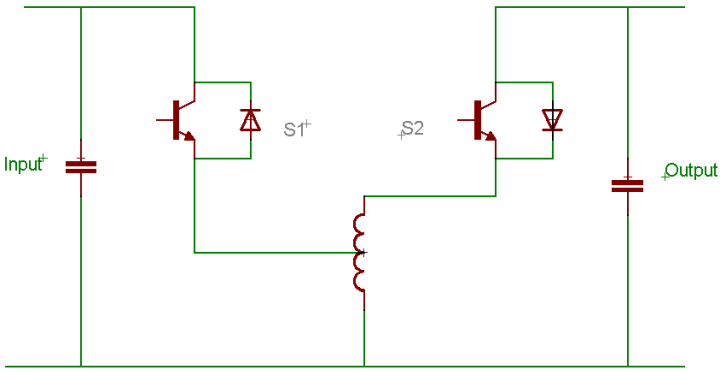

Figure 2.11: Tapped inductor converter

The voltage transfer ratio for the tapped inductor converter is given by the following equation:

$$M = \frac{U_2}{U_1} = \frac{D \cdot n}{(1-D)} \tag{2.27}$$

$$n = \frac{N_1 + N_2}{N_2} \tag{2.28}$$

Where N_1 and N_2 are the number of windings on the first half and second half of the tapped inductor respectively.

Fig. 2.12 shows how the gain is achievable by the converter. The gain may be varied by changing the value of n, the ratio of turns on the tapped inductor.

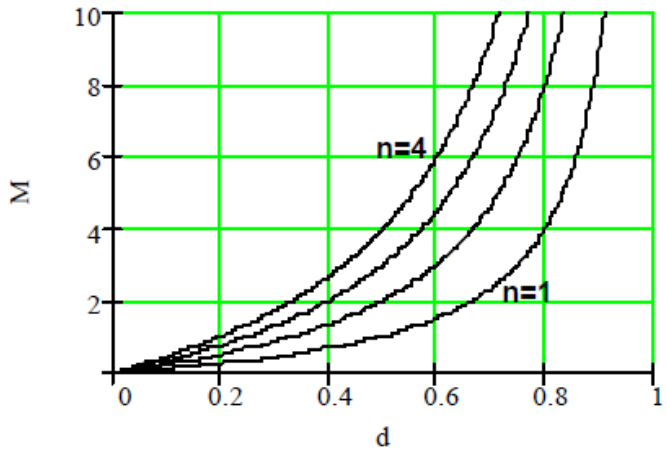

Figure 2.12: Voltage gain curves for tapped inductor converter

This converter is controlled by varying both the switching frequency and the duty cycle of switches. The frequency is varied to prevent an oscillation of energy between the two sides of the converter at low loads. The two switches are driven in push-pull mode.

The following converter topology is based on the buck and boost converter topologies, as discussed earlier. It consists of two synchronous converters in tandem sharing a single inductor. The converter is designed to use four switches to allow bi-directional power flow and the ability to operate in both buck and boost modes. The design schematic is shown in Fig. 2.13. The various states of the switches required for the converter to operate in the four different modes of operation are shown in Table 2.2.

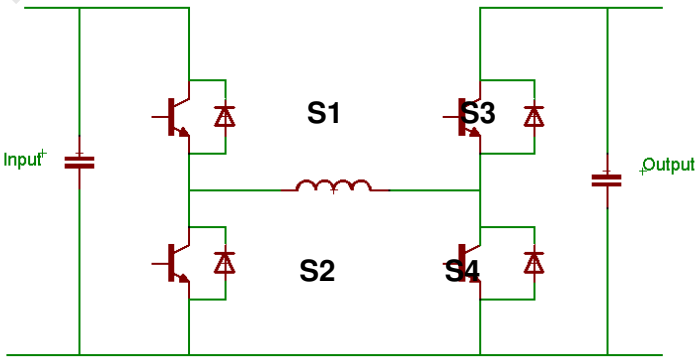

Figure 2.13: Bidirectional synchronous buck-boost converter

Table 2.2: Various switch states for operation of the synchronous converter in the four different modes of operation

Power flow direction	Mode of operation	S1	S2	S3	S4
Left to right	Step Up	ON	OFF	OFF	SW
Left to right	Step Down	SW	OFF	OFF	OFF
Right to left	Step Up	OFF	SW	ON	OFF
Right to left	Step Down	OFF	OFF	SW	OFF

An addition to the above synchronous converter is suggested by [2.20], as shown in Fig. 2.14. Across each diode and switch, a resonant capacitor is placed which enables soft switching of the switching devices. This soft switching could result in the reduction of switching losses in the converter by thirty percent. A thorough analysis of the operation of the converter topology in Fig. 2.14 is presented by [2.20] and will not be repeated here.

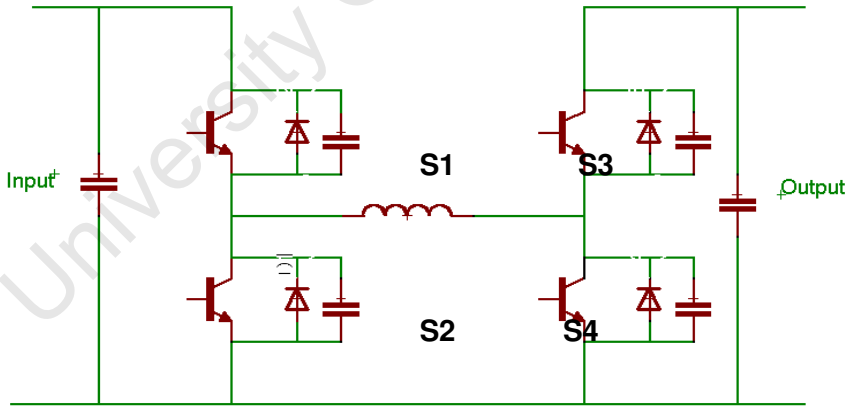

Figure 2.14: Bidirectional synchronous DC-DC converter with resonant capacitors

2.7.2 Choice of DC-DC Converter Topology

In order to meet the requirements for the flywheel system the following criteria were used in the choice of the design of the system:

- low cost
- materials available locally
- high efficiency
- low complexity
- low maintenance

The three converters that meet the requirements for bi-directional buck/boost power flow are the converters proposed by [2.20]. These are the synchronous buck-boost converter, the synchronous buck boost converter with resonant capacitors and the tapped inductor converter. A summary of the advantages and disadvantages of the converters are presented in Table 2.3 below.

Table 2.3: Advantages and disadvantages of bi-directional buck/boost DC-DC converters

	Advantages	**Disadvantages**
Synchronous buck-boost converter	Simple design Easy control	High number of switching devices
Synchronous buck-boost converter with resonant capacitors	High efficiency	Complicated control required to implement soft switching High number of components
Tapped inductor converter	Only two switching devices High boosting ability	Complicated control since gain is affected by both switching frequency and duty cycle Higher cost of tapped inductor vs. normal inductor

The topology that is implemented is the synchronous buck boost converter. This topology is implemented because it meets the design requirements stipulated at the beginning of this chapter and is shown in Fig. 2.15. Out of all the three options, the control required for the synchronous buck/boost converter is the simplest. While the tapped inductor converter has the fewest components, the price of the tapped inductor is sufficiently higher than the price of a normal inductor to negate this advantage.

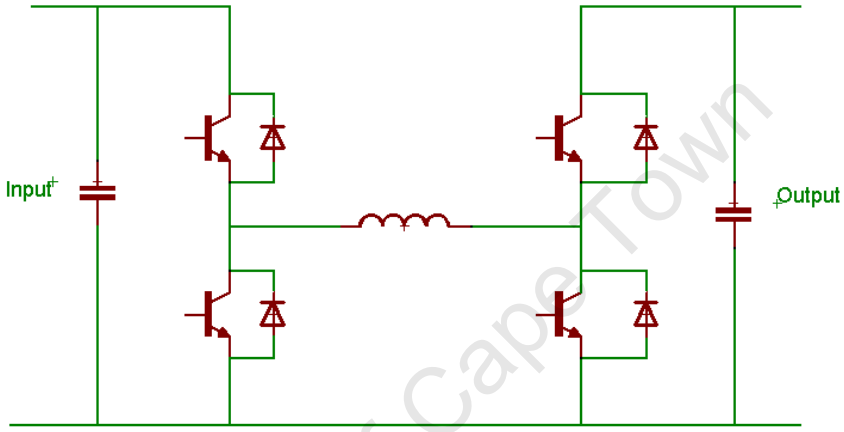

Figure 2.15: Topology that was implemented for the DC-DC converter

2.7.3 Sizing of Components

For the sizing of the components, the buck and boost stages were sized separately, after which these are combined for the bi-directional buck-boost converter. The design of the boost component of the converter will now be discussed.

The maximum boosting required is stepping up the input voltage by 3 times. This will occur when the motor is accelerating up to its maximum operating speed of 24,000 rpm. At this speed the back EMF is approximately 34V and therefore the applied voltage will need to be 36V. The minimum voltage required is 12V. Therefore if the converter is to be kept in the continuous region, the range of duty cycle required is from 0% to 66% (from equation 2.26).

From [2.19] and [2.21] the following equations were used to determine the inductance and capacitance required:

$$L = 0.074\frac{T_s \times V_o}{I_o} \tag{2.29}$$

$$C = \frac{I_{om} \times D \times T_s}{\Delta V_o} \tag{2.30}$$

Where L is the inductance (H), T_s is the switching period (s), V_o is the output voltage (V), I_o is the minimum output current (A), C is the capacitance (F), I_{om} is the maximum output current (A), D is the duty cycle, ΔV_o is the percentage voltage ripple.

The specifications of the boost converter and its component sizes are summarised in Table 2.4.

Table 2.4: Boost converter specifications and component sizes

Specification	**Value**
T_s	1/f=0.00005s
V_o	36V
D	0.66
ΔV_0	0.05
I_o	1A
I_{om}	10A
L	0.1mH
C	7mF

The maximum reduction required for generator mode of operation is 3:1. This will occur when the flywheel is at its maximum speed and the back EMF is 36V. The minimum reduction that the converter will be required to perform is when the flywheel is spinning at 8,000 rpm and the back EMF is 12V. At this time no bucking

will be required from the converter. Therefore if the converter is kept in the continuous conduction region the range of duty cycles required is from 33% to 100% (from equation 2.25). From [2.21], the components of the buck converter can be selected as follows:

$$L \geq \frac{(1 - D_{\min})V_o}{\Delta I_L f} \tag{2.31}$$

$$C_o = \frac{\Delta I_L}{\Delta V_o \times 8 \times f} \tag{2.32}$$

Where D_{min} is the minimum duty cycle, ΔI_L is the inductor current ripple (A), f is the switching frequency (Hz), C_o is the output capacitance (F), ΔV_o is the output voltage ripple (V).

The specifications of the buck converter and its component sizes are summarised in Table 2.5.

Table 2.5: Buck converter specifications and component sizes

Parameter	Value
V_o	12V
D_{min}	0.33
ΔI_L	2A
F	20 000Hz
ΔV_o	5%
L	0.2mH
C	19uF

The component sizes for the two converters were of a similar nature. The larger of the two options were chosen in each case to enable the converter to buck and boost effectively. The inductor was over-rated to ensure that the output current is as

smooth as possible to prevent torque pulsations in the motor. The final component sizes are as follows:

Input capacitance:	7mF
Output capacitance:	7mF
Inductor size:	0.4mH

The inductor was designed from first principles. The core used was the Ferro cube E 55/28/21 core with grade 3C90 material. This core was used due to its availability.

The starting point in inductor design is the product: $I_{L\max}^2 \times L$. This is used to determine the core size and the corresponding relative permeability. This is done using the DC magnetisation curve.

$I_{L\max} = 10A$ (The maximum rated motor current), L=0.4mH

$I_{L\max}^2 \times L = 40A^2 mH$

From the magnetisation curve, μ_e is found to be ≈33. Using the following formula from [2.21] and the data from the Ferox cube data sheet:

$$A_L = (H)\frac{\mu_e \mu_o}{l/A} \tag{2.33}$$

Where A_L is the inductance rating, μ_e is the relative permeability of the magnetic core, μ_o is the permeability of free space = 4π x 10^{-7} H/m and *l*/A is the core factor

A_L was found to be 119nH.

From the Ferox cube data sheet the airgap required was found to be 5mm. Finally the number of turns required was found to be 58 turns using the formula below from [2.21].

$$\text{Required turns} = \left[\frac{DesiredL(nH)}{A_L\left(\frac{nH}{N^2}\right)} \right]^{1/2} \tag{2.34}$$

The size of the wire used was as large as possible, to limit the resistance of the inductor, while still allowing the correct number of turns to fit on the core. The wire size chosen was copper wire with a diameter of 0.315mm.

The converter was controlled using PWM control. The switching frequency was 20 kHz.

The driver circuit used to switch the MOSFETs is shown in Fig. 2.16. The input driver signals are sourced from a dSPACE controller card. All control is performed by the controller card, which allows for rapid control prototyping. The MOSFETs were mounted on a heat sink to dissipate the heat generated.

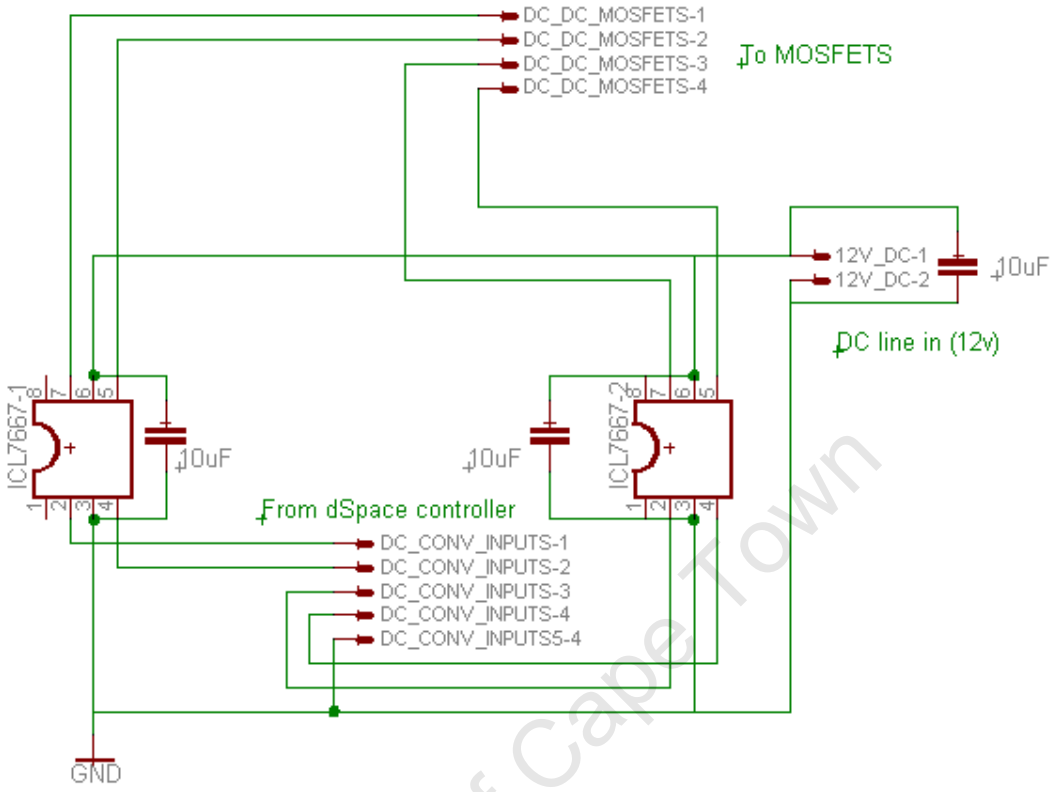

Figure 2.16: MOSFET driver circuit for DC-DC converter

2.7.4 DC/DC Converter Simulation

The following set of simulation results shows the DC-DC converter operating under its various modes. These tests were performed on the DC-DC converter in isolation of the flywheel system. For all tests conducted, a load of 1Ω is used.

Fig. 2.17 shows the voltage and current waveforms for the converter operating in buck mode with a duty cycle of 50%. The input to the converter (consumer-end) is 12V and the output, which is connected to the BLDC drive end, is shown in Fig. 2.17. At a 50% duty cycle the expected output should be 6V, however taking the diode losses into account, the output voltage settles at 4.6V as shown in the figure.

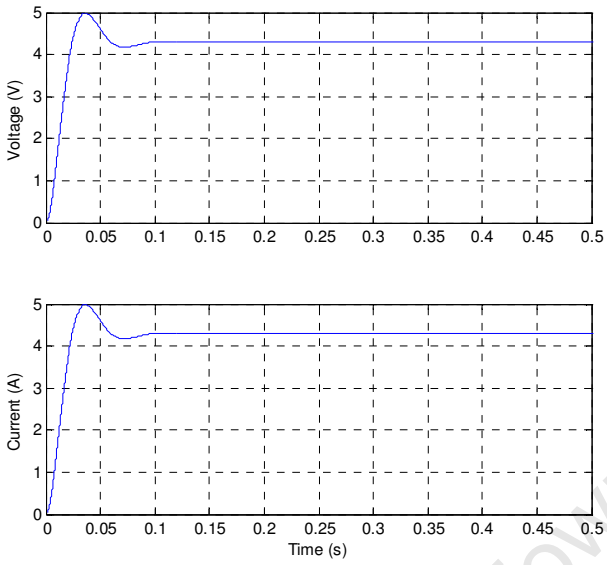

Figure 2.17: Buck mode of DC-DC Converter

Figure 2.18 shows voltage and current waveforms for boost operation. Again the input (consumer-end) is 12V and the duty cycle is 66%. Under these conditions the voltage should be boosted to 3 times its input value, 36V, however taking the losses into account, the output settles to 33.5V. Both buck and boost modes of operation in this case are transferring power from the solar panel to the flywheel via the machine of operation would be responsible for ramping up the flywheel to 25,000 rpm.

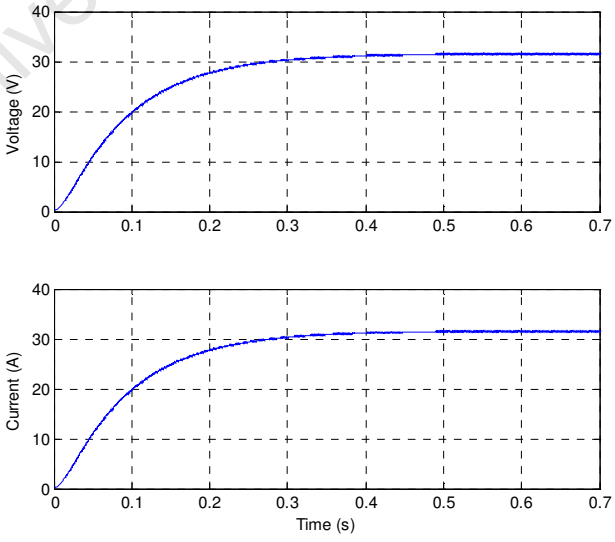

Figure 2.18: Boost mode of DC-Dc Converter

The third test shows power being transferred from the flywheel to the load. In this mode, the DC-DC converter would need to be bucking in the opposite direction. The input in this case is the BLDC drive-end, which would have a maximum voltage of 34V, which would need to be reduced to 12V at the output, therefore the duty cycle is set to 30%. Fig. 2.19 shows the output voltage at the consumer-end, whereby the voltage is approximately 9V, instead of 12V, again attributed to losses. Therefore, indicating that a greater duty cycle would be required to maintain the voltage at 12V.

These results illustrate the converters ability to transfer power in both directions while also highlighting the losses which need to be catered for in the experimental design.

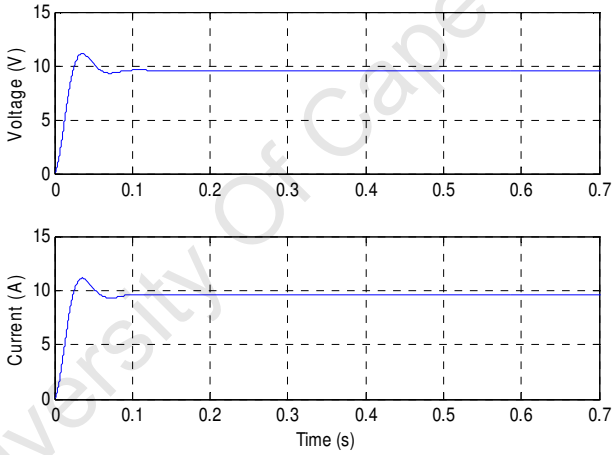

Figure 2.19: Buck mode of DC-DC Converter in when generating

2.8 BLDC Converter and Encoder Design

Due to the absence of brushes in the machine, commutation cannot occur naturally but forced commutation is required. This commutation is controlled by electronics. The purpose of the commutation strategy is to ensure the commutation of the stator windings corresponds to the correct position of the rotor. In order for this to occur, the controller needs to know the position of the rotor. However, a precise determination of the rotor position is not necessary, as it is only required that the

position of the rotor is known at the commutation points [2.23] Two methods for detecting the rotor position will be presented and discussed below.

To control the stator windings for commutation, an inverter consisting of three half bridges is used. Fig. 2.20 shows the standard schematic of a BLDC inverter.

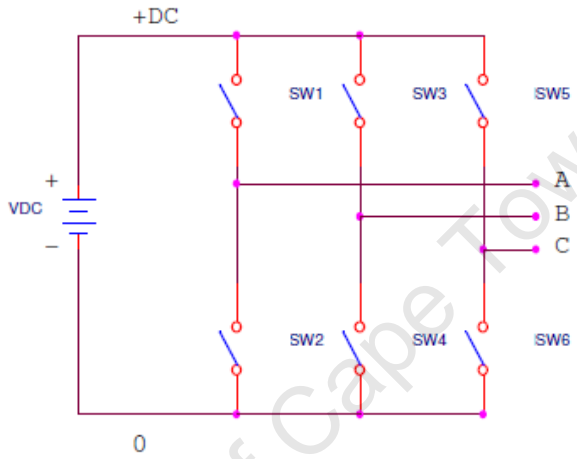

Figure 2.20: BLDC Inverter

In order to control the machine, only two of the windings are energised at any one time. This is achieved by connecting the terminal of one phase to the positive terminal of the supply and one end of another phase to the negative terminal. This switching strategy results in currents of a trapezoidal shape flowing through the stator windings.

The table 2.6 below gives the switches that are required to be on for each of the 6 possible commutation segments.

Table 2.6: Switch Commutation for CW Rotation

Hall Sensors value (CBA)	Phase	Switches
101	A-B	SW1;SW4
001	A-C	SW1;SW6
011	B-C	SW3;SW6
010	B-A	SW3;SW2
110	C-A	SW5;SW2
100	C-B	SW5;SW4

If the number of magnetic poles on the rotor is increased, the commutation strategy does not change [2.23], however it is necessary to account for the conversion between electrical and mechanical revolutions.

2.8.1 Rotor Position Measurement Using Hall Sensors

Three Hall-effect sensors are placed 120 electrical degrees apart within the stator. With the sensors placed in these positions, there are six different possible outputs from the sensors. With every change in hall sensor output, commutation occurs.

The advantages of using Hall sensors to determine the position of the rotor are:

- Simplified signal processing as the hall sensor output is not greatly affected by electrical noise.
- Simplified signal processing as the commutation sequence is easily obtained from Hall sensor outputs.

The disadvantages of using Hall sensors to determine the position of the rotor are:

- Increased cost of the machine
- Temperature sensitivity

2.8.2 Rotor Position Using Back EMF Sensing

The direct Back-EMF method of sensorless position determination is the most popular method used [2.24]. This method involves sensing the back EMF in the phase that is not being fed by the motor inverter. The instant of commutation is reached when the slope of the back EMF changes from a positive or negative value to zero [2.23]. The problem of sensing these commutation points is extremely difficult due to the large amount of electrical noise that is present at any stage [2.23]. Significant processing power or additional circuitry is required to filter out this noise so that a clear reading of the back EMF can be obtained.

A significant disadvantage of using the sensorless approach when driving a BLDC motor is the complicated start up procedure required [2.23]. A start up procedure is required since the rotor is at standstill; therefore no back EMF is present. This makes estimation of the rotor position from the back EMF impossible at start up. A start up procedure is proposed by H.C. Chen and C.M Liaw in [2.25].

For this high speed application, the hall sensors provide a more reliable and simplistic means of rotor position detection, therefore these were selected.

2.8.3 BLDC Converter Simulation

The BLDC drive performs the necessary commutation for the PM machine, speed control is merely performed by varying the input DC voltage. For the simulations, a DC source is used instead of the DC-DC converter, as this validates the operation of the drive in isolation of the DC-DC converter. Speed, line voltage and current are shown in the figures below.

Fig 2.21 shows results for start up and motor mode of operation. The start up procedure occurs between 0-0.45 seconds, whereby the DC voltage is maintained at 12V while the speed ramps up to 8,000 rpm, after which the DC voltage is stepped to 36V, whereby the speed then ramps up to 25,000 rpm.

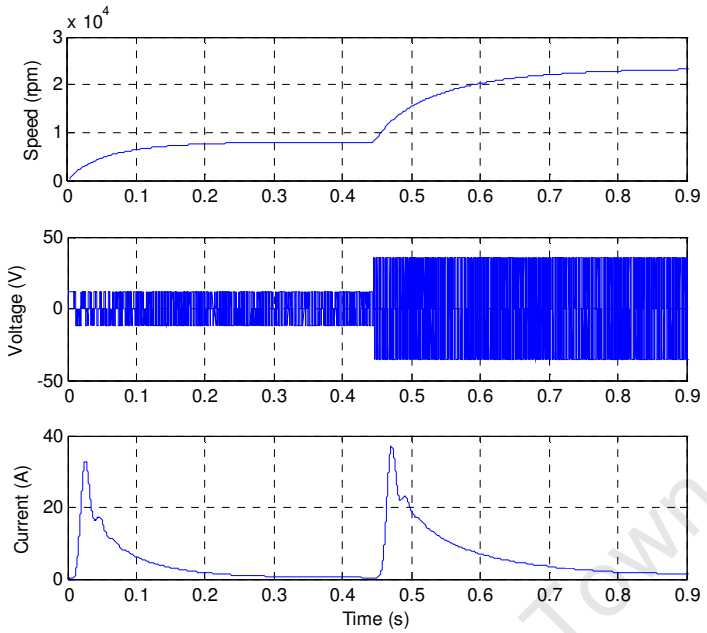

Figure 2.21: Start up and motor mode of operation

Based on the short time required to ramp up to 25,000 rpm, it is quite evident that the flywheels inertia is not taken into account for these simulations. This was done to reduce the processing time required for simulation, which proved too lengthy for the processing capabilities of the PC. Fig. 2.22 illustrates the generating mode of operation whereby the power from the flywheel is dissipated into a 1Ω resistor.

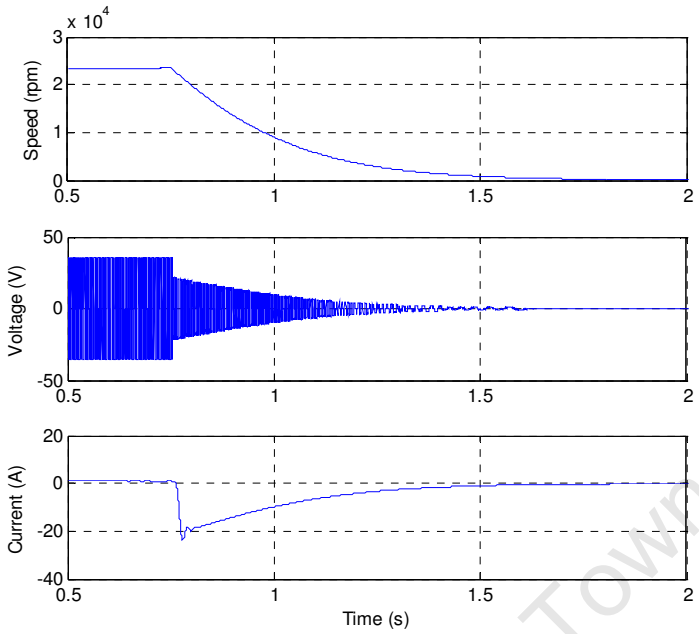

Figure 2.22: Generating mode of operation

The machines speed falls off from 25,000 rpm to standstill. The overall flywheel system however would disconnect from the load at 8,000 rpm. It is clear from the Fig. 2.22 that current is reversed in this mode, since it is now generating.

2.9 Flywheel Drive System Simulation

The following set of results shows tests conducted on the overall flywheel system, i.e. DC-DC converter and BLDC drive. Fig. 2.23 shows the speed, voltage and current for start up and motor mode of operation. When operating the motor below 8,000 rpm, the motor is current limited to a maximum of 10A. When surpassing 8,000 rpm, the machine enters the constant power region whereby the machines power is limited to rated power, 100W. Fig. 2.24 shows the steps in output voltage of the DC-DC converter as the voltage is firstly stepped from 0V to 10V, then at 0.8seconds it is stepped from 10V to 33V, to achieve the desired speed response.

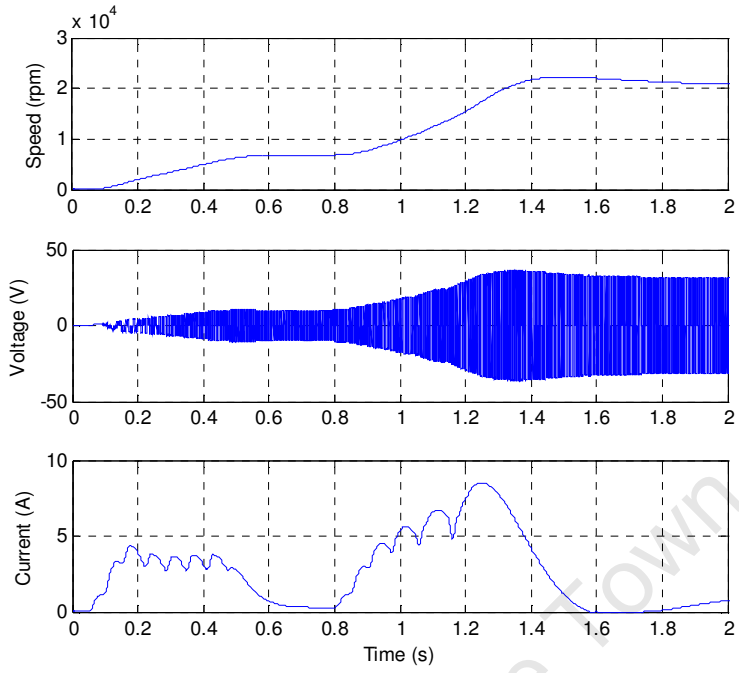

Figure 2.23: Start-up and motor mode of operation

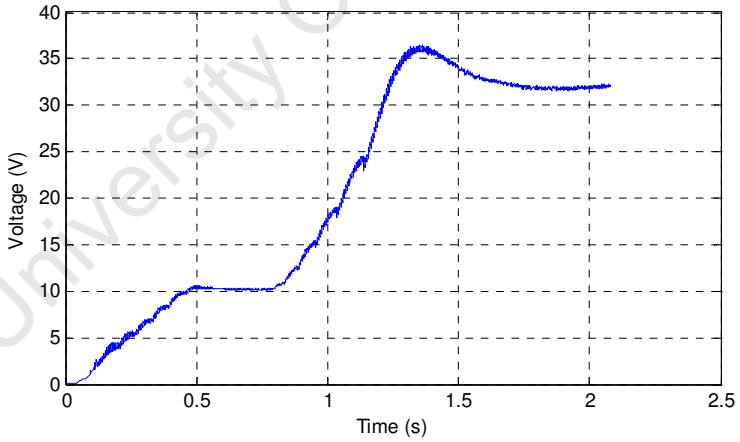

Figure 2.24: Output Voltage for start-up and motor mode of operation

Fig. 2.25-2.27 shows the system in the generator mode of operation. In this test, the speed is initially at 22,000 rpm, after which power is required at the load end. As power is drawn from the flywheel, the machine speed steadily decreases until it reaches 8,000 rpm, as shown in Fig 2.25. At 8,000 rpm, the system is disconnected

from the load. Fig 2.26 shows the voltage at the BLDC drive-end of the DC-DC converter. As power is drawn, the machines speed decreases and so does the back-emf. As this decreases, the control attempts to maintain an output voltage at the consumer-end of 12V, as shown in Fig. 2.27.

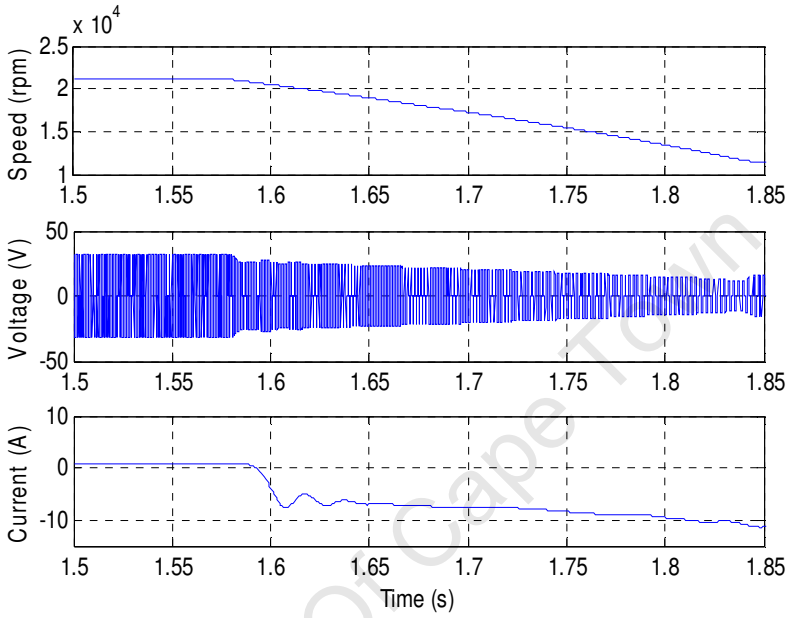

Figure 2.25: Generator mode of operation

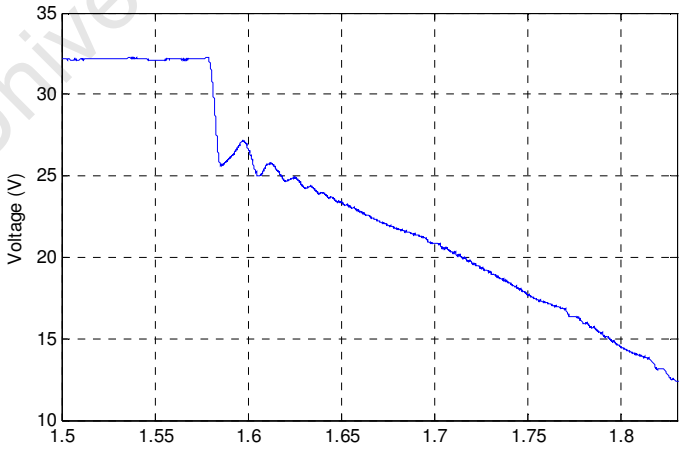

Figure 2.26: DC voltage at terminals of BLDC drive for generator mode of operation

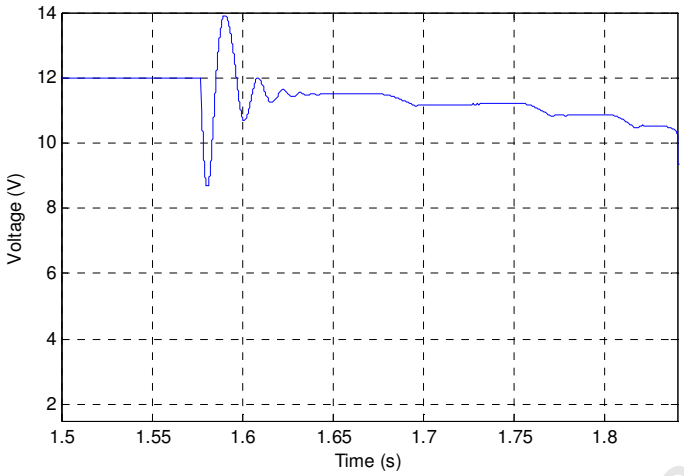

Figure 2.27: Consumer voltage for generator mode of operation

2.10 Practical Drive System

The simulated drive system was partially implemented due to prototyping time constraint and safety concerns. The DC-DC converter was not considered instead a manual switch was used during the testing phase to ensure full control of the system as shown in Fig. 2.28.

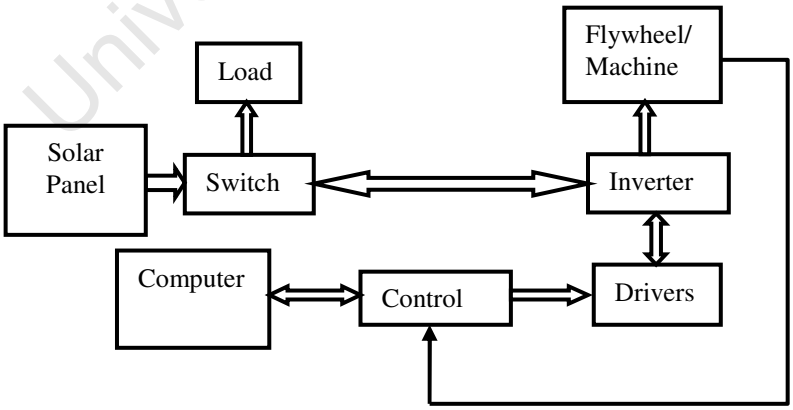

Figure 2.28: Practical drive system

2.11 Concluding Remarks

This chapter examined different machine topologies that should be considered for the flywheel system. The major driving factors of choice where ease of construction, compact and less cost. The axial flux machine with brushless mode of operation was considered. A bi-directional DC-DC converter and drive system were designed and simulated in MATLAB simulink. The results showed the ability of the converter to transfer power in both directions. The flywheel drive simulations showed its ability to control the machine during motor and generator mode. I acknowledge the contributions by Dave Johnson, Mac Stuart and Paul Barendse on the DC-DC converter and the drive system. Conventional bearings were considered for this research due to cost and time constraint.

2.12 References

[2.1] G. Genta, *Kinetic energy storage, Theory and practice of advanced flywheel systems*, Butterworth & Co. Ltd, 1985.

[2.2] P. I. Tsao, "An integrated flywheel energy storage system with a homopolar inductor motor/generator and high-frequency drive," PhD Thesis, fall 2003.

[2.3] J. Lahteenmaki, "Design and Voltage Supply of High-Speed Induction Machines," PhD Thesis, Helsinki University of Technology, 2002.

[2.4] N. Bianchi, S. Bolognani and F. Luise, "Analysis and Design of a PM Brushless Motor for High-Speed Operations," *IEEE Transactions on Energy Conversion*, vol. 20, no. 3, September 2005

[2.5] Z.Q. Zhu, K.Ng, D. Howe, "Design and analysis of high speed brushless permanent magnet motors," in *Proc*. EMD97, No 444, 1-3 September 1997.

[2.6] M.Aydin, S.Huang, T.A. Lipo, "Axial flux permanent magnet disc machines: review, " Research report, 10-2004.

[2.7] R. Qu, M. Aydin and T. A. Lipo, "Performance comparison of dual rotor radial flux and axial flux permanent magnet BLDC machines,"

[2.8] J. F. Eastham, M. J. Balchin, T. Betzer, H.C. Lai, and S. Gair. "Disk motor with reduced unsprung mass for direct EV wheel drive," *IEEE Int. Symp. On Industrial Electronics*, vol. 2, pp. 569—573, 1995.

[2.9] F. Sahin, "Design considerations of the flywheel mounted axial-flux permanent magnet machine for a hybrid electric vehicle," EPE, Lausanne, 1999.

[2.10] K.R. Pullen, M.R. Etemad, and M.R. Fenocchi. "The high speed axial flux disk generator unlocking the potential of automotive gas turbine," *IEE colloquium on Machines and Drives for Electric and Hybrid Vehicles*, pp. 1—4, June 1996.

[2.11] P. R. Upadhyay, K.R. Rajagopal, B.P. Singh, "Effect of armature reaction on the performance of the axial field permanent magnet brushless dc motor using FE method," *IEEE Transactions on Magnetic*, vol.40, no 4, July 2004.

[2.12] P. Campbell, "Principles of a Permanent-Magnet Axial-Field D.C. Machine," *In Proceedings of the IEE*, vol. 121, no. 12, pp. 1489-1494, 1974

[2.13] D. Platt. "Permanent magnet synchronous motor with axial flux geometry. *IEEE Trans. on Magnetics,*" vol. 25, No. 4, pp. 3076—3079, 1989.

[2.14] J. F. Gieras, R. Wang and M. J. Kamper, *Axial Flux Permanent Magnet Brushless Machines*, Dordrecht, Kluwer Academic Publishers: 2004.

[2.15] P. Kurronen, Torque Vibration Model of Axial-Flux Surface-Mounted Permanent Magnet Synchronous Machine. Dissertation. Lappeenranta University of Technology, Finland, pp. 123, 2003.

[2.16] R. Wang and J. Kamper, "Calculation of Eddy Current Loss in Axial Field Permanent Magnet Machine with coreless Stator, " *Energy Conversion,* vol. 19, No. 3, pp. 39, 2000.

[2.17] D. Johnson, "Design Considerations and Implementation of an electromechanical Battery System, PHD thesis, " University of Cape Town. 2007.

[2.18] S. Mac William, "Design of a drive system for a flywheel battery," Bsc thesis, University of Cape Town, 2008.

[2.19] N. Mohan, T.M. Undeland and W.P. Robbins. *Power Electronics, Converters, Applications, and Design*, John Wiley and Sons Inc, Third Ed., 2003.

[2.20] Symmetrical DC/DC converter, http://www.freepatentsonline.com/6636431.html. Last visited 21 September 2008

[2.21] K. Otmar, *Switched Mode Power Supplies in Practice*, John Wiley and Sons Ltd, 1989.

[2.22] Atmel AVR492: Brushless DC Motor Control using AT90PWM3/3B, http://www.atmel.com/dyn/resources/prod_documents/doc7518.pdf. Last visited 14 October 2008

[2.23] J. Dixon, Position Estimator and Simplified Current Control Stratergy for Brushless –DC Motors, Using DSP Technology, (2002)

[2.24] T. Siostrzonek, S. Pirog, "The Flywheel Energy Storage with Brushless DC Motor- The Practical Results," *IEEE Transactions on Power Electronics*, vol. 21, no. 4, pp. 1541-1545, 2006,

[2.25] H.C. Chen, C.M Liaw, "Current-Mode Control for Sensorless BDCM Drive With Intelligent Commutation Tuning, " *IEEE Transactions on Power Electronics*, vol. 17, no. 5, pp. 747- 756, 2002

Chapter 3

Flywheel rotor design

This chapter discusses the rotor configurations and design for the flywheel rotor profile. The various configurations are described and selection is made for the most suitable type. The rotor designs and results are presented. The analyses include stress, modal, fatigue and windage models developed for the profiles.

3.1 Flywheel Rotor Configurations

There are three main types of rotor configurations as mentioned in section 1.3.1. Two rotor configurations are considered in this thesis, the inside out and the conventional design. The details of each configuration are discussed in the following sections.

3.1.1 Inside-Out Configuration

The inside-out configuration is also referred to as the vertical axis concentric system. The configuration is shown in Fig. 3.1 with an electrical machine embedded in the flywheel. This configuration was considered due to the choice of the Halbach array machine because of its high efficiency and low cost [3.1]. This configuration ensures safety of the machine during high speed rotation.

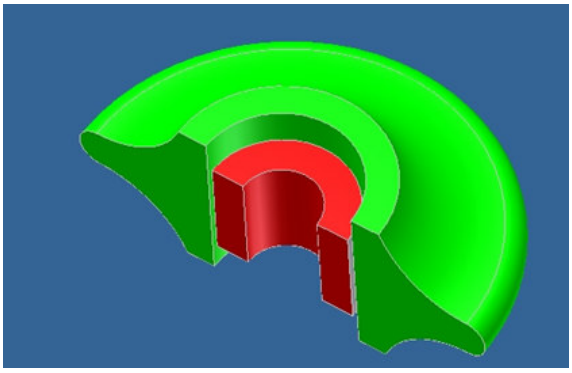

Figure 3.1: Inside out design

The major disadvantage of this configuration for this specific application is the thermal considerations. The evacuation of the heat from the machine is complex especially in the vacuum unit. A heat pipe is required in the shaft as the heat accumulation in the flywheel material would induce thermal stresses, reducing the integrity of the flywheel. The heat stored in the central hole would reduce the efficiency of the machine. The testing of the machine which is embedded in the flywheel as shown in Fig. 3.2 is challenging. This follows from the machine being embedded in the middle of the entire system.

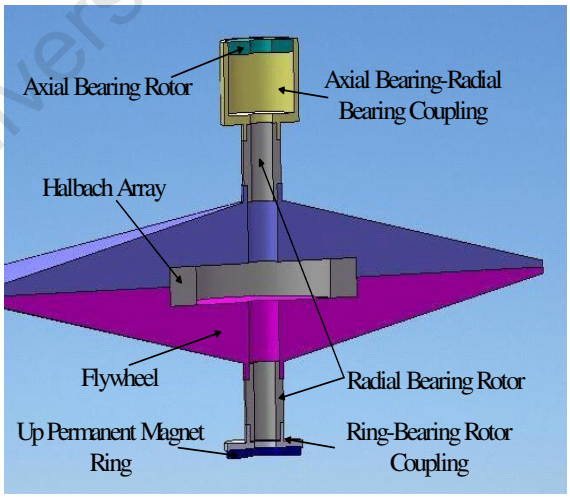

Figure 3.2: Levitating system

In addition, the various components of the system are design dependent. For example, a change in the radius of the machine would spiral down to affect the flywheel, bearing and containment designs. This complexity in design makes the prototyping even more difficult.

As shown in Fig. 3.2, the inside-out type was also designed with magnetic bearings, which has advantages to the design, that is, low losses and high efficiency however; this increases the cost of the system [3.2]. The total system and the hollow shaft are fixed in between two plates to ensure the stability of flywheel system. The electric machine is inside the flywheel which is levitated and the stator winding are fixed on the shaft.

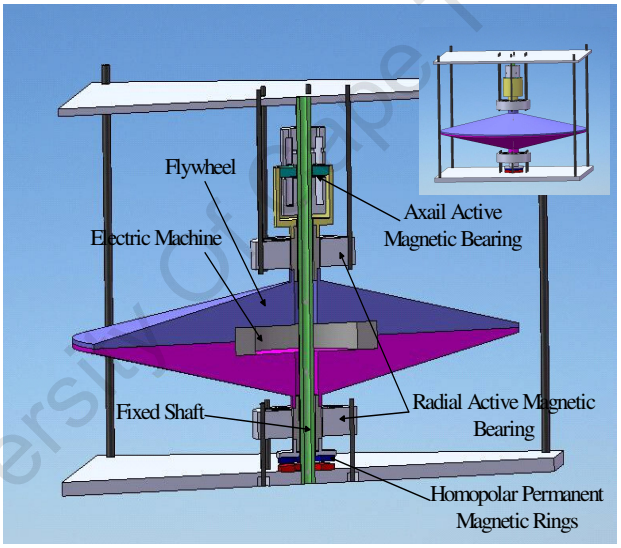

Figure 3.2: Levitating and stationary parts

The levitation and stationary parts are as shown in Fig. 3.3 and include the upper magnet ring, ring-bearing rotor coupling, radial bearing rotor, flywheel, Halbach array (Rotor of Electric Machine), axial bearing radial bearing coupling and axial bearing rotor. The magnet ring pairs provide repulsive magnetic force to suspend the total weight of these parts. The radial active magnetic bearing provides the balance force to counteract the centrifugal force of these parts. The axial active magnetic

bearing provides the axial magnetic force to offset the axial direction vibration of this part.

The magnet ring pairs at the bottom of system are applied to levitate the total weight of flywheel and other bearing components. The magnet ring is formed by a Neodymium Iron Boron (NdFeB) material, which is brittle. In order to protect the ring pairs against large pressures imposed, the lower and upper magnet ring is encased into the lower steel plate.

In order to keep the magnet ring in the centre of the shaft and reduce the difficulty in the assembly, the inner radius of ring-bearing rotor coupling is 1.5 mm larger than the shaft. In case the radial active magnetic bearing malfunctions, the ring-bearing rotor coupling will detach and rotate along the shaft, rather than destroy the permanent magnet ring pairs.

The stator of radial active magnetic bearing is suspended by six suspension steel to ensure the stability of the stator. The rotor, levitated and rotating with the flywheel, is in the centre of the stator. The air gap between rotor and stator is 1.5 mm and this is the same for the air gap between the rotor and shaft. This ensures that there is no contact between stator and rotor which could damage the stator in the case of radial magnetic bearing failures. The junction of the flywheel and rotor is 15 mm and is reserved for the displacement sensor.

In order to keep the axial stability of the flywheel, an axial magnetic bearing is applied in the system. The rotor of the axial magnetic bearing is connected to the rotor of the radial magnetic bearing by the axial bearing radial bearing coupling. All these three parts are levitated and rotate with the flywheel. The two stators of the axial magnetic bearing are fixed onto the shaft while the lower one is enwrapped by the axial bearing-radial bearing coupling. The air gap between the rotor, axial bearing-radial bearing coupling and shaft is 1.5mm to prevent interference between the embedded stator and axial bearing-radial bearing coupling.

The radial bearing coupling and ring bearing rotor coupling were designed using non-magnetic stainless steel to avoid interruption of the flux circuit and to reduce the hysteresis losses in the steel. This configuration and design was not pursued beyond the design due to a time cost factor especially in South Africa where the magnets have to be imported.

3.1.2 Conventional Configuration

The conventional rotor design is the most commonly used configuration as presented in [3.3-3.5]. Most of the energy is stored in the rotor which is attached to a shaft used by the motor to spin the flywheel. The horizontal axis cascaded flywheel/machine system topology is shown in Fig. 3.4. The main features of this topology include:

- Horizontal axis rotation
- Flywheel rotor attached directly to shaft
- Free choice of machine
- Ability to use conventional bearings

The main advantages of this system include:

- The machine and flywheel design are independent of each other
- Limited heat problems from machine to flywheel
- The machine and flywheel are compact
- Possibility of a low cost design

This is the simplest configuration; however, the complications arise from the shaft and flywheel attachment. The major problems are the radial elongation at the connection point and the dynamic stability of the flywheel.

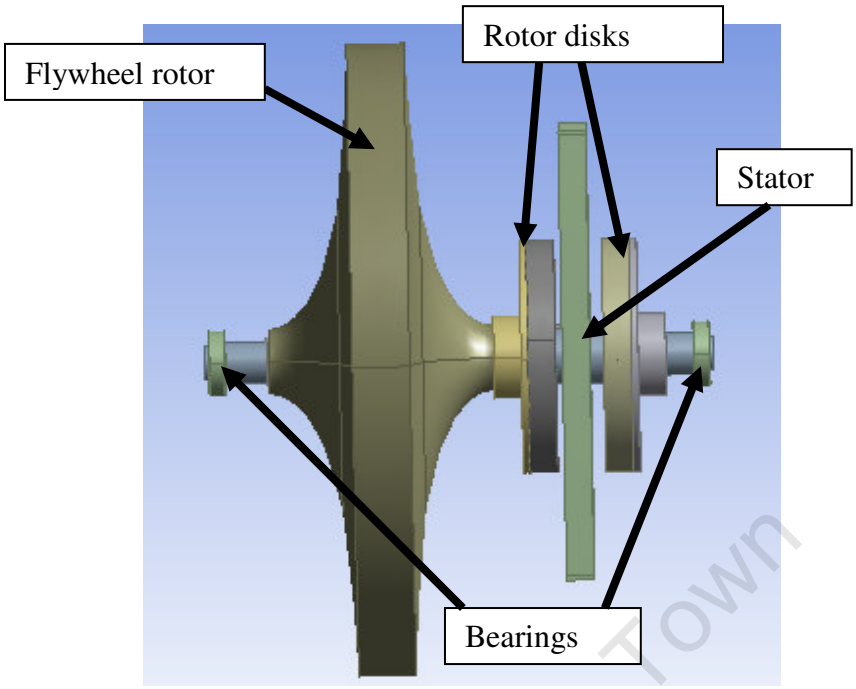

Figure 3.3: Conventional configuration

The radial elongation differences are represented by the relationship:

$$U = \rho\omega^2 r^3 / E \tag{3.1}$$

Where U is the radial displacement, E is the young's modulus, r is the radius of connection interface, ρ is the mass density and ω is the angular speed.

The E glass composite material will exhibit higher elongation than the stainless steel shaft. The impact of the radial elongation is different for a thin or thick rim. The thin rim is dependent on the inner radius while the thick rim is dependent on the density of Young's modulus ratio.

The dynamic stability of a flywheel rotor depends on the material to inner damping of a system. As presented in [3.6], various solutions are suggested, for example, for thin rim, a disc or a spoke system can be used but for a thick rim, an elastomeric layer can be used. Generally, the press fit is more reliable because it curbs the radial

elongation and also solves the problem of dynamic stability. The press fit in the thick rim is possible by shrink fitting, conical interfaces and by pre-tension winding techniques. The two options are explored in the prototyping phase in chapter 4.

3.2 Choice of Flywheel Rotor Material

Steel has been in used in flywheel rotor design for over 20 years [3.6]. Arguably, the reason for this is better predictable dynamic performance, homogeneous characteristics, ease of mass production and low manufacturing cost with typical values of $0.25/kg. This may be low but so is the J/kg of metallic flywheels. High power density metal flywheels require expensive and difficult processes and materials to create pre-stressed flywheels. However, their low energy densities and poor failure criteria raise concerns of safety and hence increase the cost of the containment structure. Massive containment structures made from reinforced concrete/metal is required to contain these steel systems in case of failure. In addition, these systems are bulky and difficult to handle and are usually fixed installations. The mode of metal failure is elastic, which stores large amounts of elastic energy into the fragments before severing off the structure. During failure, these steel structures will typically break into 3 main fragments and some smaller pieces with high translational energies and this can cause severe damage to equipment and personnel around if not contained.

Composite flywheels, on the other hand, are much smaller and are lightweight because of their high specific kinetic energy. Their physical properties are not homogeneous, like metals, and these have to be taken into consideration. Composites failures occur differently and the main causes are debonding, fibre pullout and delamination [3.7]. For example, delamination is prevented in current filament wound designs by using a multi-rim approach, which is a function of wall thickness. The process of filament winding and separating the rims with an elastomer and balancing the resulting structure is cumbersome and reflected in the

price of commercial flywheels. Various flywheel manufacturing techniques with benign failure are further elaborated in chapter 4.

3.3 Flywheel Rotor Profile

Conventional shape profiles have been widely used in rotor design as presented in [3.3] [3.5] [3.8]. These shapes are used because of existing analytical approaches to establish profile parameters. However, in order to increase the energy stored, high speeds have to be exerted on the rotor which necessitates high strength materials. These materials are expensive [3.9], hence there is need to optimize the shape [3.10] used in the flywheel in order to reduce subsequent costs from extra material required when using conventional shapes. Literature in material and shape optimization is limited.

As presented in [3.11], the best thickness distribution along the radius of a centrally bored flywheel is investigated. Stodola's solution for an evenly stressed turbine disk without a hole is used to examine the shape for even stress distribution with a central hole. A numerical shape optimization of the shape with a FEM based structural model was used. A simplified model was developed and found that an even stress shape does not exist for a hole radii greater than the square root of one third of the radius flywheel. The optimum shape predictions are in agreement only when the radius of the bore does not exceed the approximately one third of the radius of the disk.

JM Chern [3.12] investigates the optimal design of the rotating disks with the radial displacement as a prescribed value. In this work, a sufficient optimal condition is derived and used to determine the optimal disk profiles. The resulting disks were found to be far from satisfying the uniform strength condition despite the weights being almost similar.

David Eby [3.13] discusses the optimal design of elastic flywheels using a genetic algorithm to search for the shape variations to optimize the specific energy density. The use of genetic algorithm was due to decreased process time and better search space. The limitation to this technique is that it's not implemented with a central hole, making it complex for the flywheel application in this thesis.

In section 3.4, Berger and Porat's work on the flywheel rotor is investigated and section 3.5 discusses Stodola's work using non-uniform solutions for flywheel rotor design with a central hole. Considerable contributions from design work in [3.14] made this section of this work possible. Further, high level mathematical analysis using maple soft by Michael Nlandu made this work achievable.

3.4 Optimal Design of a Rotating Disk -Ultimate shape

This section discusses the derivation of the general shape for optimal design of the flywheel rotor and is based on work by Berger and Porat with a central hole. Partial differential equations theory is used with a piecewise differentiable disk built with five shapes. In [3.10] piecewise optimal shapes are used to create the ultimate shape.

Berger does not provide for a central hole however, this hole is required to attach the shaft on which the machine will also be placed. As shown in Fig. 3.5, the five shapes are considered with the central hole (P_1-P_2), exponential (P_2-P_3), minimum thickness (P_3-P_4), maximum slope (P_4-P_5), and maximum thickness profiles (P_5-P_6)

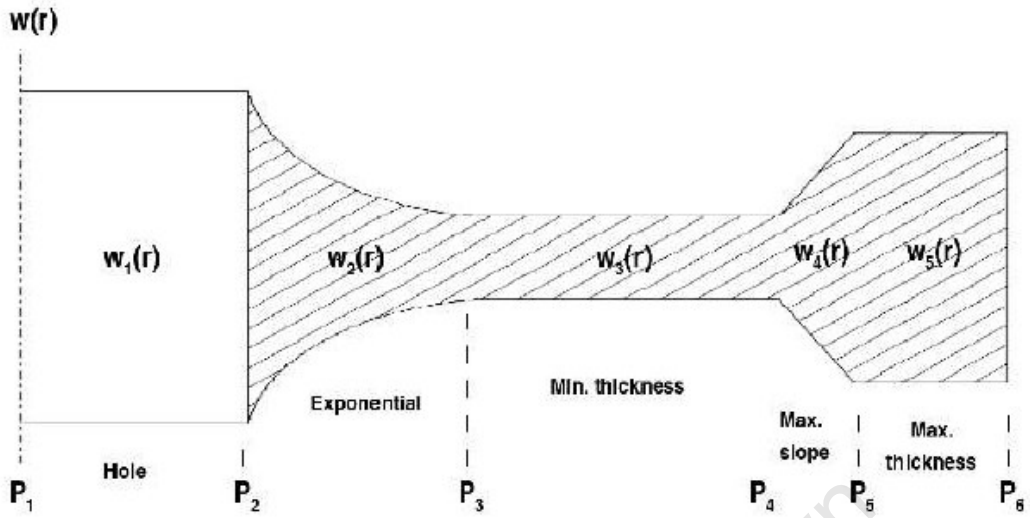

Figure 3.4: Five shapes used to derive the ultimate shape

In the derivation of the ultimate shape, dimensionless equations are considered as shown in equations (3.2) to (3.5)

$$r = \frac{R}{R_o} \tag{3.2}$$

$$W(r) = \frac{W(R)}{R_o} \tag{3.3}$$

$$S_R(r) = \frac{S_R(R)}{S_{Max}} \tag{3.4}$$

$$S_T(r) = \frac{S_T(R)}{S_{Max}} \tag{3.5}$$

A solid disk of homogeneous isotropic material of mass density ρ is considered. A thin ring of the same diameter and material properties is added with respect to the different locations. A hole is created in the centre and allows for the disk to rotate about its axis attaining a continuously varying hole and bounded thickness W(r) which will be axi-symmetrical and symmetrical with respect to the centre plane. The variable and different thickness are bounded in the closed interval [0, 1] which can be subdivided into five thickness called shapes W(r) in our case.

A general optimal analytical shape is made possible by locating different points along the shape. The thickness is bounded in relative sizes as well as in profile slope so that the disk can be treated as a two-dimensional axisymmetrical problem. As the disk rotates, the curve of the shape acquires a new location as it changes in the XY direction.

The structural configuration of the system is fully specified by the design parameters which may be fixed or varied. The fixed parameters are called geometrical constraints and the varying parameters are called strength constraints but these vary within a specified range in a closed interval [0, 1]. A thin homogeneous rotating disk of a variable thickness is considered for the purpose of storing kinetic energy.

The exact optimal shape is one with piecewise smooth derivatives. Applying a parametric study in which optimal designs for a sequence of rotational speeds are observed reveals the existence of three speed intervals, each characterised by a common type of optimal design.

3.4.1 Description of Flywheel Rotor Profile

The homogeneous disk shown in Fig. 3.5 has five basic shapes: the hole at the centre, the exponential constant (maximum) stress shape, the minimum thickness shape, the maximum slope shape and the maximum thickness shape which are defined analytically. This is represented by general equation (3.6).

This part describes the rotating disk process starting from low to high speed. While

$$w(r)=\begin{cases} w_1(r)=0 & p_1\le r\le p_2 \\ w_2(r)=\delta L\exp[(k^2/2)(p_3^2-r^2)] & p_2\le r\le p_3 \\ w_3(r)=\delta L & p_3\le r\le p_4 \\ w_4(r)=\delta L+2\delta'(r-p_4) & p_4\le r\le p_5 \\ w_5(r)=\delta U & p_5\le r\le p_6 \end{cases} \qquad (3.6)$$

observing this evolving process of this optimal design as function of the speed *k*, it is realised that from the low speed, the optimal design appears to accumulate the bundle of mass at the rim as we choose the location of P_4. The maximum mass at the rim will shrink as the speed increases. In the medium speed range, a constant (maximum) stress shape with exponential profile develops in this region, the size of which extends both in thickness and in length.

In the high speed range, the exponential constant stress shape in this section, retreats back towards the hole in the centre and covers a shorter inner section of the disk. The parameters which contribute on the design variables are geometrical and behavioural constraints;

The geometrical constraints are imposed on the disc dimension as in equation (3.7) and (3.8).

$$\sigma_L \le W(r) \le \sigma_U \tag{3.7}$$

$$\left|W^{'}(r)\right| \le 2\sigma \tag{3.8}$$

The structure of the configuration is given below in respect to the geometrical constraints:

- P_1 and P_6 are fixed
- $P_1 \le \ldots\ldots \le P_6$
- $P_1 \ldots P_6$ are all fixed during low speed
- $P_2 \ldots P_5$ are variable in medium to high speed
- $\delta_L \le \delta_U$ are fixed but can be modified
- $w_2(r) = \delta_L \exp\left(\left(p_3^2 - r^2\right)k^2 \big/ 2\right)$ is variable
- $w_4(r) = \delta_L + 2\delta^{'}\left(r - p_4\right)$ is variable

3.4.2 A General Exact Optimal Shapes

The general exact optimal shape is shown in Fig. 3.6. The five basic shapes do not slope but show different shape that are functions separated by different locations from P_1 to P_6.

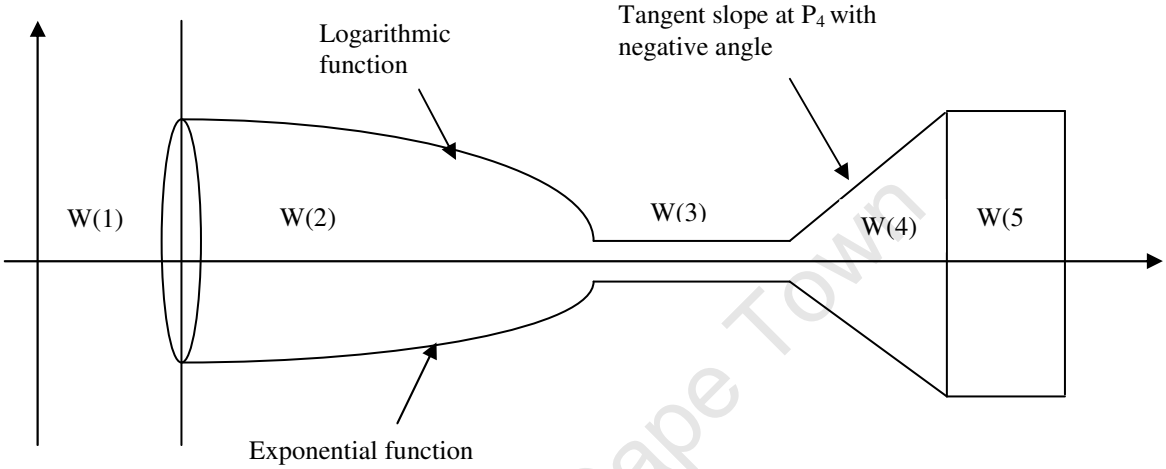

Figure 3.5: Optimal shape for medium speed with five basic shapes

3.4.2.1 Creating the Hole: First Profile

The differentiable configuration of piecewise disk profile is a hole when the Specific Kinetic Energy (SKE) *e(k,w)* that provides the shapes is zero, this implies that the first shape $W_1(r)$ is zero.

The first shape is illustrated by equation (3.9).

$$e(k,w) = k^2 \frac{\int_0^1 r^3 w_1(r)dr}{\int_0^1 r w_1(r)dr} = 0 \qquad (3.9)$$

3.4.2.2 Finding the Exponential Shape $W_2(r)$: Second Shape

The configuration of the profile provides the exponential shapes at the location [P_2, P_3] in the medium speed range. The SKE is isolated and reduced at this interval [P_2, P_3] which results into the two axis-symmetrical function problems, the exponential curve on both sides of the r-axis. This is defined in equation (3.10).

$$e(k,w) = k^2 \frac{\int_r^{p_3} r^3 w_2(r) dr}{\int_r^{p_3} r w_2(r) dr} \tag{3.10}$$

The solution in equation (3.11) is given by integrating equation (3.10)

$$e(k,w) = \frac{1}{2}(p_3{}^2 + r^2)k^2 \tag{3.11}$$

When P_3 is extended to the left, we have

$$w_2(r) = e^{\frac{1}{2}\left(p_3^2 + r^2\right)k^2} \tag{3.12}$$

Where $p_3^2 = -2In(\sigma)/k^2$ and $w_2(r) = w_3(r)$

The resulting solution for the second shape is

$$w_2(r) = w_3(r)\, e^{\frac{1}{2}(p_3^2 - r^2)k^2} \tag{3.13}$$

3.4.2.3 Finding the Minimum Thickness Line $W_3(r)$: Third Shape

The third shape is an ordinary point and the tangent at this point is the straight line which is a constant. The solution at this interval for $(P_3, r), r \to P_4$ is:

$$w_3(r) = \frac{1}{2}\left(r^2 + P_3^2\right)k^2 \tag{3.14}$$

Where $w_3(r) = \delta_L$ for $\delta_L = 0.01$

3.4.2.4 Finding the Slope Shape $W_4(r)$ that Maximises the SKE*:* Fourth Shape

This case is reduced only in the interval (P_4, P_5) where $r \to P_4$ from the geometrical restriction we know $\left|\frac{\partial w(r)}{\partial r}\right| \leq 2\sigma$ and by the theory of non-linear differential equation, $\frac{\partial w(r)}{\partial r} = 2\sigma(r \to p_4)$, where $P_4 = P_3 + d$.

At the point P_4 is given by equation (3.15).

$$w_4(r) = \delta_L + 2\sigma\ (r - p_4) \tag{3.15}$$

Therefore, this result shows how the maximum thickness shrinks from the outer section of the ring to a certain point in the inner section.

3.4.2.5 Find the Maximum Thickness Shape $w_5(r)$: Fifth Shape

The same analysis for the minimum thickness is made here, with the only difference being the interval (P_5, P_6), and the infimum provided by the set of the smallest *r*, *k* in this closed interval are bigger than the one provided at the minimum shape. When solving the piecewise shape, it is assumed that other locations are zero and their integrals are zero. Hence $w_5(r = \delta_u)$ where $\delta_u = 0.1$

3.4.3 The Optimum Design Problem

The objective of the design is to maximize the SKE subject to certain geometrical restrictions and strength requirements for a given rotational speed defined in equation (3.16).

$$\delta_L, \delta_u, \sigma, \mu\left(0 \le \delta_L \le \delta_u; \sigma > 0\right) \tag{3.16}$$

The continuous function W(r) for which the SKE occurs as $e(k, w) \to Max$, where $r \in [0,1]$. The following constraints hold for $\delta_L \le w(r) \le \delta_u$ resulting in equation (3.17).

$$\left|\frac{\partial w(r)}{\partial r}\right| \le 2\sigma,\ S_R \le 1,\ S_\tau \le 1 \tag{3.17}$$

With the constraints defined, the stress behaviour of the shapes can be analysed for high speed operation.

3.4.4 Optimal Shape for High-Speed Operation

During high speed rotation, the mass moves from the rim towards to the central hole to increase the strength as shown in Fig. 3.7. The centre thickness must therefore be guarded from violating both stress and maximum thickness constraints. The optimal shape of this rotating free-disk is terminated at its slope as it converges to the upper bound less than the given limit.

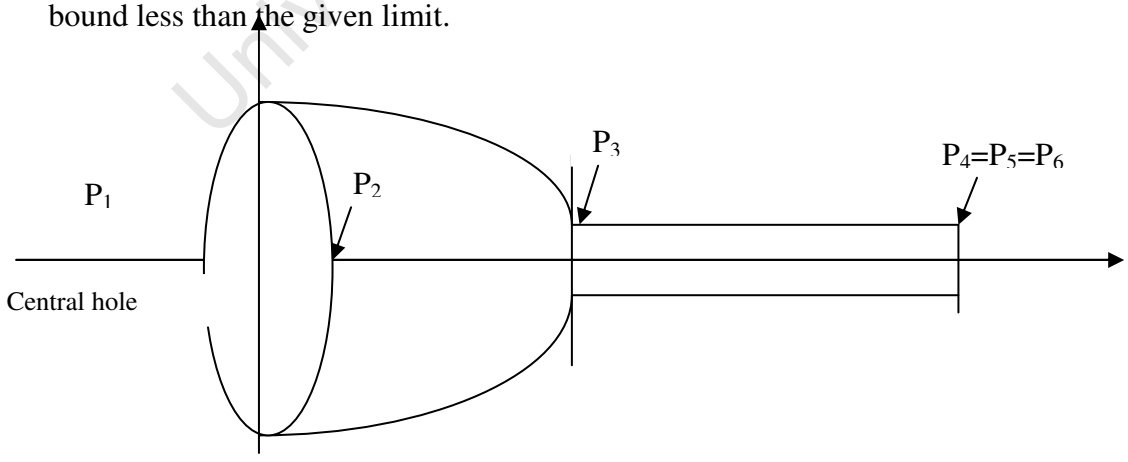

Figure 3.6: The optimal shape for the ultimate high speed profile

The joining of many finite smooth curves is a path created by the radius *r* with the parameter interval [P_1, P_6]. This interval was subdivided into five parts and at each interval a continuous function is seen as the SKE attains its maximum on the boundary of that subinterval. This is defined in equation (3.17).

$$\frac{dw(r)}{dr} = -w(r)rk^2 \tag{3.17}$$

This gives a solution in equation 3.18

$$\log w(r) = -\frac{1}{2}r^2k^2 + A \tag{3.18}$$

Where $A = \log w_3(r)$

Considering the focus is for P_2 to P_3, solution becomes

$$\frac{w_2(r)}{w_3(r)} = e^{-\frac{1}{2}r^2k^2} \tag{3.19}$$

The table 3.1 below shows the specifications of the optimal flywheel profile developed as shown in Fig. 3.8.

Table 3.1: Specifications of the optimal flywheel

	Results
Inertia	0.299kg.m^2
Mass	12.04 kg
Outer radius	0.255m
Height	0.09 m

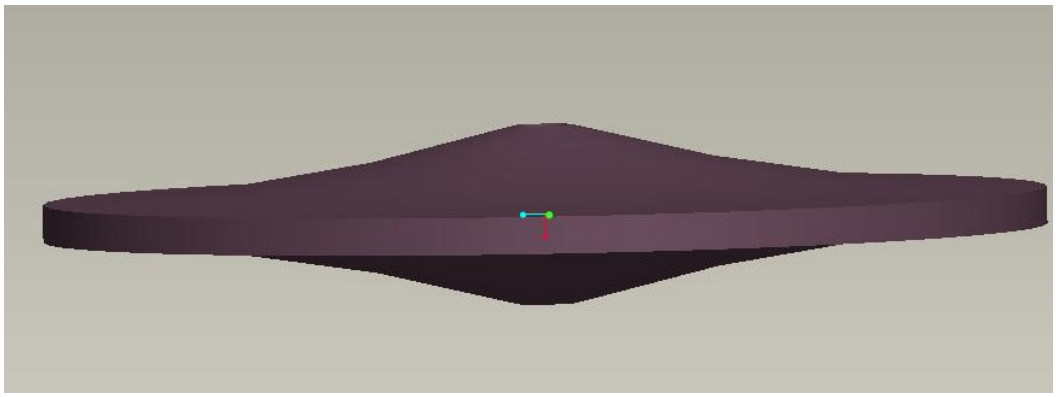

Figure 3.7: Optimal flywheel profile for 25,000 rpm

3.5 Hyperbolic Approach

This is the second profile design approach. Analytical stress solutions for isotropic materials are used to derive the profile. In principle, the amount of energy stored in a flywheel is given by equation (3.20) [3.6];

$$E = \frac{1}{2} J \left(\omega_{\max}^{2} - \omega_{\min}^{2} \right) \tag{3.20}$$

Where J is the moment of inertia and ω is the rotational speed of the flywheel rotor.

The moment of inertia can hence be derived from equation (3.20) given the rotational speed and amount of energy required from the storage system. The initial mass of the flywheel system can be estimated given the volume required to store the energy requirement and the density of the material [3.1] [3.6]. The volume is derived from equation (3.21) below.

$$E = \alpha' \alpha'' \alpha''' \, k \sigma Vol \tag{3.21}$$

Where E is the energy required, α' is the safety factor, α'' is the depth of discharge, α''' is the ratio between mass of the flywheel and mass of the system, σ is the maximum tensile strength of the material and Vol is the volume of the profile required to store the required energy

The initial mass is calculated from the mass, volume, density relation. As the energy stored is proportional to the moment of inertia, the outer radius of the flywheel is required and this can be derived from the relationship in equation (3.22) below, which is used for estimating the moment of inertia of a cylinder. The final moment of inertia for the required profile is approximately 90% of that of a cylinder.

$$J = \frac{1}{2} m\left(r_o^2 + r_i^2\right) \tag{3.22}$$

Where J is the moment of inertia, m is the mass of the flywheel, r_o is the outer radius and r_i is the inner radius.

The approximate values considered up to this point are for a cylinder, that is, mass, height and radius; however the real profile values are a percentage of the cylinder values as some material is sliced to generate the profile. Thus for various rotational speeds, different factors should be used to derive optimized results.

3.5.1 Design Literature

This design work is developed from solutions in [3.15-3.18] on steam and gas turbine work on variable disks. Due to problems associated with stresses and deformation in flat disks rotating at high speeds in steam and gas turbines, a methodology of increasing the thickness at the centre to increase the strength of the turbine was established. This approach was used to develop a non-uniform stress approach to flywheel profile design.

By writing all forces acting on an element of unit thickness gives;

$$\frac{d}{dr}(r\sigma_r) - \sigma_h + \rho\omega^2 r^2 = 0 \tag{3.23}$$

Where r is the radius, σ_r is the radial stress and σ_h is the hoop stress.

A new equilibrium equation can be derived from equation (3.23) giving;

$$\frac{d}{dr}(hr\sigma_r) - h\sigma_h + h\rho\omega^2 r^2 = 0 \tag{3.24}$$

From Hooke's law, the displacement can be established from equations (3.25) and (3.26).

$$\frac{du}{dr} = \frac{1}{E}(\sigma_r - \mu\sigma_h) \tag{3.25}$$

$$\frac{u}{r} = \frac{1}{E}(\sigma_h - \mu\sigma_r) \tag{3.26}$$

Where u is the displacement (strain) and E is the *Young's* modulus

Eliminating u from equations (3.25) and (3.26) gives a compatibility equation (3.27) which holds for variable thickness.

$$\frac{d}{dr}(\sigma_h) - \mu\frac{d}{dr}(\sigma_r) + \frac{1+\mu}{r}(\sigma_h - \sigma_r) \tag{3.27}$$

Eliminating the hoop stress from equation (3.23) and (3.27) we obtain a result that is variable of the radial stress only. Differentiating equation (3.23) and substituting into equation (3.27) gives a differential equation (3.28) as shown below.

$$r^2(hr\sigma_r)'' + r(hr\sigma_r)' + (hr\sigma_r) - \frac{rh'}{h}\left[r(hr\sigma_r)' - \mu(hr\sigma_r)\right] + (3+\mu)\rho\omega^2 r^3 h = 0 \tag{3.28}$$

For disks of variable thickness, the radius and thickness are related by the thickness function

$$h = \frac{h_i}{r^q} \tag{3.29}$$

Where q is any positive number.

As the outer height of the flywheel varies with radius to cope with varying rotational speeds, the equation is modified to;

$$\frac{h_i}{h_o} = \left(\frac{r_o}{r_i}\right)^q \tag{3.30}$$

Hence, substituting equation (3.29) into equation (3.28) gives a linear equation as shown below;

$$r^2(r\sigma_r)'' + r(r\sigma_r)' - (r\sigma_r) + (3+\mu)\rho\omega^2 r^3 = 0 \tag{3.31}$$

Equation (3.31) has variable coefficients so that a reduced equation (3.32) can be derived when $\rho\omega^2 = 0$

$$hr\sigma_r = r^n \tag{3.32}$$

Where *n* is a solution to a generated quadratic equation.

The values of *n* are solved from the quadratic equation

$$n_1 \,\&\, n_2 = \frac{-q}{2} \pm \sqrt{\left(\frac{q^2}{4} + \mu q + 1\right)} \tag{3.33}$$

To solve for the radial stress, two simultaneous equations are generated from equation (3.34) with the assumption that for non-uniform stress profiles, the radial stress at the inner radius and the outer radius is zero; hence two simultaneous equations can be generated and solved.

$$hr\sigma_r = C_1 r^{n_1} + C_2 r^{n_2} - \frac{(3+\mu)\rho\omega^2}{8-(3+\mu)q} r^3 h \tag{3.34}$$

The hoop stress can hence be derived from equation (3.35)

$$\sigma_h = r\sigma_r' + \rho\omega^2 r^2 \tag{3.35}$$

And the displacement can be derived from equation (3.28).

The solutions from Hartog's work neglect the coefficients of C_1 and C_2 when divided by *hr,* however, this work proceeds to take into account the impact of *hr* on the integration constants.

3.5.2 Application of the Technique to Flywheel Design

This technique focuses on selecting a profile which gives the required energy and its ability to handle high stresses. This technique also meets the ever varying characteristics of the machine which is tagged on the energy demands.

From equation (3.29), for different values of q, various profiles can be derived giving different radial, hoop stress and displacement. These values are analyzed and the profile giving lower radial stress with non-negative and optimally low values of hoop stress is selected and used for flywheel design. This value is then validated in ANSYS [3.19] with the resulting profile as shown in Fig. 3.9 and design parameters in table 3.2.

Table 3.2: Design parameters of profile two

	Analytical	**Numerical**	**% error**
Height	0.15 m	0.15 m	0.00
Outer radius	0.2309 m	0.2309 m	0.00
Mass	13.090 kg	14.987 kg	12.66
Inertia	0.3504 kg.m^2	0.348 kg.m^2	0.69

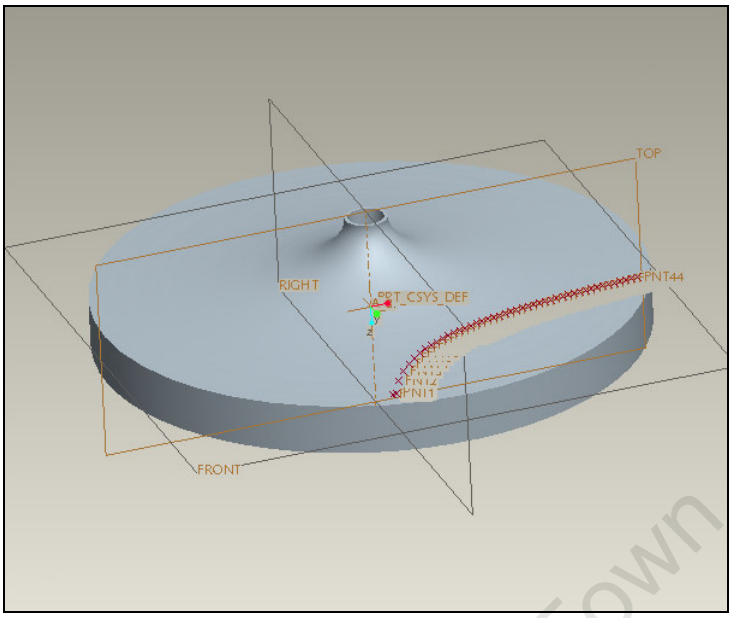

Figure 3.8: 3-D view of flywheel profile

3.6 Modal Analysis

In high-speed flywheel design, emphasis must be taken in accurately predicting the natural frequencies of the rotor at the design stage so as to minimize high vibration when operating through resonant frequencies [3.20]. Accurate prediction also lowers the probability of failure [3.21]. Modal analysis is also used to predict critical speed and damage of structures [3.22] using mode shapes and natural frequencies. Analytical and FE analyses are used to establish the natural frequencies and modes of the flywheel rotor and to verify the influence of the shaft length, shaft diameter, the bearings, and the material properties. In this work, the shaft length and bearings are varied while the material properties are kept constant.

In [3.21], the shaft frequencies are calculated using equation (3.36) below [3.23] and the analytical results were compared to the numerical results with a close correlation. However, the simplifications in the analytical models may cause undesirable errors [3.24].

$$\omega_n = a_n \sqrt{\frac{EI}{\mu_1 l^4}} \tag{3.36}$$

Where *E, I,* μ_1*, l* are the Young's modulus, inertia, mass per unit length, and length of the shaft, respectively, and a_n is a numerical constant calculated by the Rayleigh method, which is dependent on the problem boundaries.

FE solutions on the other hand can be used to ascertain the natural frequencies and accurately predict the modes [3.21] [3.24]. For example, cylindrical and conical modes introduced by mounting of the rotor in bearings require FEA to accurately predict.

A modal analysis was done to ensure that the flywheel system design operates in the sub-critical region and also to ascertain the natural mode shapes and frequencies during free and pre-stressed vibration. Residual unbalance in the flywheel, which is inevitable, can excite critical speeds in the rotor-bearing systems and are a function of unbalance and shaft speed.

To ensure a safe operating point from the design stage, the shaft length was varied and the results observed. Initially, a 500mm long shaft with 25mm diameter was considered however a preliminary analysis indicated low natural frequencies. A 365mm long shaft with 30mm shaft diameter was later considered giving more desirable results. The variation of the shaft diameter and length was limited by the by the peripheral speed of the commercially high speed ceramic and energy efficient bearings. After manufacture of the flywheel, static and dynamic balancing was performed to ensure reduction of residual unbalance.

3.6.1 Analytical Approach

The symmetric rotor model developed in [3.25] is used to calculate the analytical natural frequencies. The rigid body translational frequencies, γ_1, γ_2 for the X and Y are derived from equation (3.37) below.

$$\gamma_1 = \gamma_2 = \sqrt{\frac{2k}{m}} \tag{3.37}$$

The angular frequencies γ_3, γ_4 are defined by equation (3.38)

$$\gamma_3 = \gamma_4 = \frac{1}{2}\frac{J_p}{J_d}\omega \pm \sqrt{\left(\frac{1}{2}\frac{J_p}{J_d}\omega\right)^2 + \gamma_5^2} \tag{3.38}$$

Where $J_p = \left(\frac{m}{2}\right)\left(\frac{R_o^2}{4}\right)$ and $J_d = \frac{m}{4}\left(\frac{R_o^2}{4} + \frac{1}{3}h^2\right)$

$$\gamma_5 = \sqrt{\frac{2kh^2}{4J_d}} \tag{3.39}$$

J_p is the polar inertia, J_d is the diametral inertia, m is the Mass of the flywheel rotor, k is the stiffness of one bearing mount and h is the height of the flywheel.

3.6.2 Numerical Approach Using ANSYS

In FE there are various mode extraction methods used to solve for natural frequencies and mode shapes. In ANSYS, the main ones are;

Block Lanczos method – typically used for large symmetric eigenvalue problems, this method utilizes a sparse matrix solver. PCG Lanczos method - used for very large symmetric eigenvalue problems (500,000+ DOFs), and is especially useful to obtain a solution for the lowest modes to learn how the model will behave. Subspace method - used for large symmetric eigenvalue problems, though in most cases the Block Lanczos method is preferred for shorter run times with equivalent accuracy. Reduced (Householder) method – This is faster than the subspace method because it uses reduced (condensed) system matrices to calculate the solution, but is normally less accurate because the reduced mass matrix is approximate. Unsymmetrical method - used for problems with unsymmetrical matrices, such as fluid-structure interaction problems. Damped method - used for problems where damping cannot be ignored, such as journal bearing problems. QR damped method - faster than the

damped method, this method uses the reduced modal damped matrix to calculate complex damped frequencies.

3.6.3 Profile One Results

The profile one represents the ultimate shape profile. The results of the analytical and FE simulations are shown in Fig. 3.10 and 3.11.

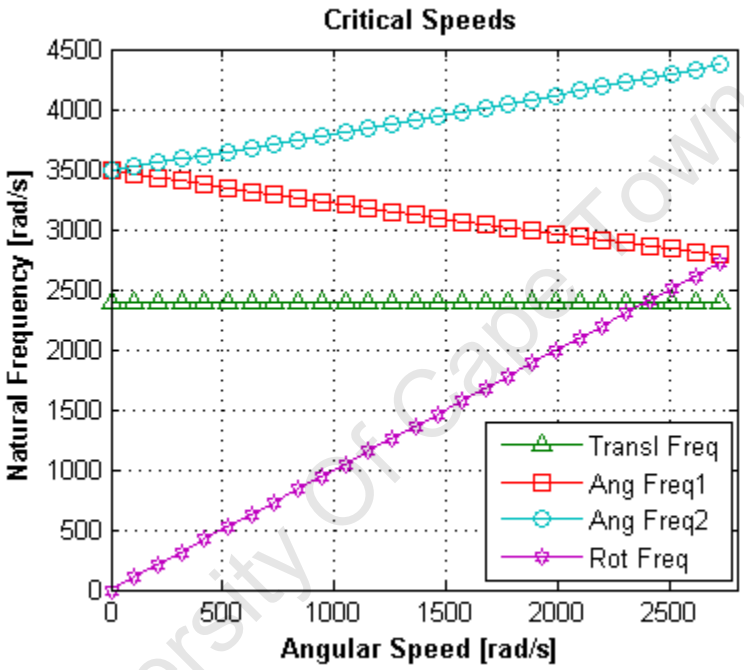

Figure 3.10: Modal analysis results

Fig. 3.10 plots these natural frequencies as a function of angular speed in rad/s and the resonances which occur when the natural frequencies intersects with ω. From this plot it can be seen that the all three of these resonance speeds fall above 24,000 rpm.

The FE results for profile one is given in Fig. 3.11. A vector deformation plot provides the relative magnitude and orientation of displacement in response to the loading environment.

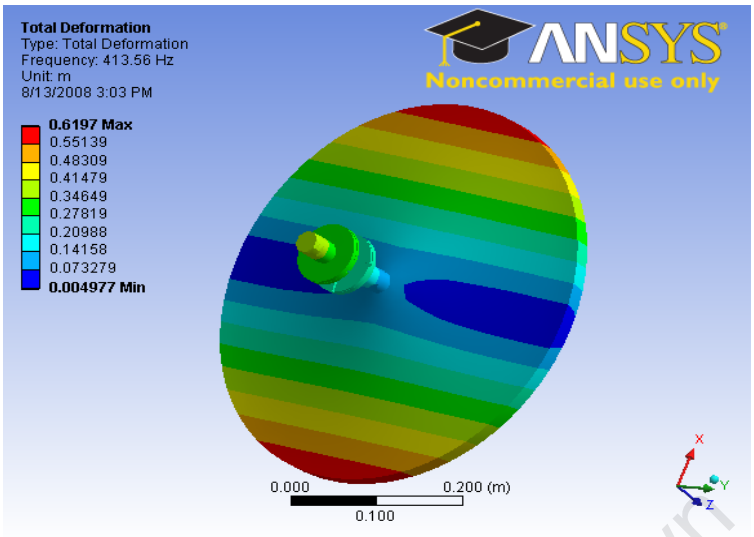

Figure 3.11: FE results

The first critical speed occurs at 413.65HZ which represents 2,597 rad/s. A comparison was considered between the analytical and FE and presented in Table 3.3.

Table 3.3: Comparison of analytical and FEA results for profile one

Critical speed (Rad/s)		
Mode	Analytical	Finite Element
First	2,590	2,597
Second	2,650	2,715

There is a correlation between the analytical and FE results which shows the system will be able to ramp to speed without passing through a critical speed. However, in reality, this is not possible as the manufactured components have numerous anomalies resulting from non-linearity of the materials.

3.6.4 Profile Two Results

Profile two represents the hyperbolic shape profile and the results of the analytical and FE simulations are shown in Fig. 3.12 and 3.13.

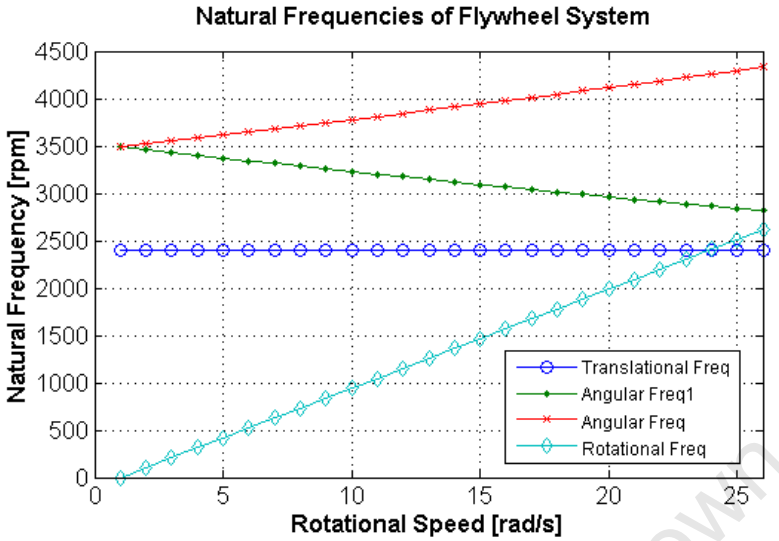

Figure 3.12: Analytical results of the critical speed for hyperbolic approach

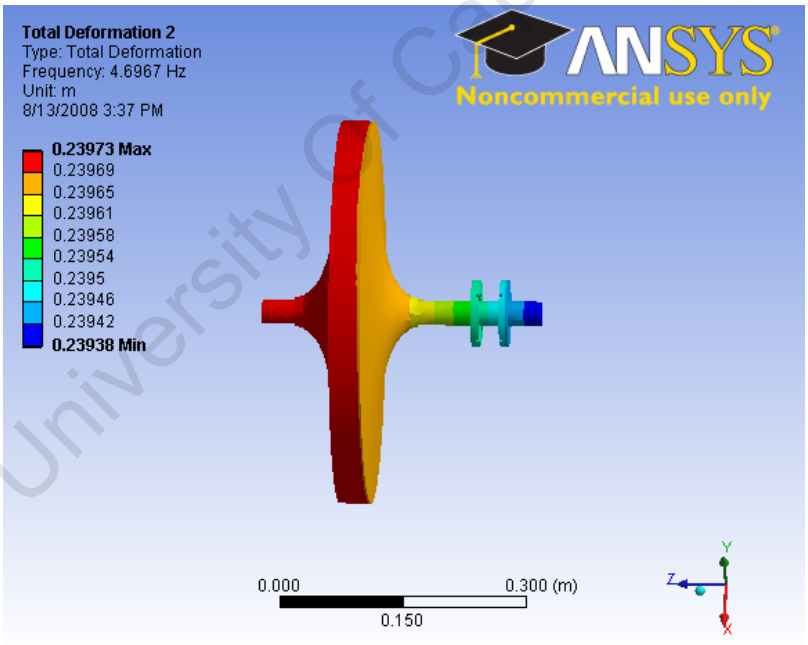

Figure 3.13: FEA results of the first and second natural modes for hyperbolic approach

Table 3.4: Comparison of analytical and FEA results for profile two

Critical speed (Rad/s)		
Mode	Analytical	Finite Element
First	0	25
Second	0	29
Third	2,490	2,433
Fourth	-	2,474
Fifth	2,750	2,709

The results of profile two also show a close correlation for the resonant frequencies.

3.7 Numerical Stress Analysis

Numerical stress analysis was performed to ensure that the entire system withstands the static and dynamic forces applied to it. The FE analysis was performed using the ANSYS package on both flywheel profiles. This is achieved when the determined stress from the applied forces is less than the known maximum strength of the material. A safety factor is considered in the design process as shown in section 3.4. The solutions of the stress-strain relationship for orthotropic materials are an extension of the isotropic solution.

For a uniform thickness ring, the stress distribution is given by equation (3.40):

$$\frac{d\sigma_r}{dr} + \frac{\sigma_r - \sigma_\theta}{r} + \rho\omega^2 r = 0 \tag{3.40}$$

For orthotropic materials, the stress-strain relationship in the r and θ direction is given by equations (3.41) and (3.42) [3.7] [3.26].

$$\sigma_r = \frac{E_r}{1-\upsilon_{r\theta}\cdot\upsilon_{\theta r}}\varepsilon_r + \frac{E_r\upsilon_{\theta r}}{1-\upsilon_{r\theta}\cdot\upsilon_{\theta r}}\varepsilon_\theta \tag{3.41}$$

$$\sigma_\theta = \frac{E_\theta\upsilon_{r\theta}}{1-\upsilon_{r\theta}\cdot\upsilon_{\theta r}}\varepsilon_r + \frac{E_r}{1-\upsilon_{r\theta}\cdot\upsilon_{\theta r}}\varepsilon_\theta \tag{3.42}$$

Solving equation (3.42) and equation (3.40) gives a differential equation solution in equation (3.43).

$$r^2\frac{d^2u_r}{dr^2} + r\frac{du_r}{dr} + \frac{E_\theta}{E_r}u_r = -\frac{1-\upsilon_{r\theta}\cdot\upsilon_{\theta r}}{E_r}\cdot\rho\omega^2 r^3 \tag{3.43}$$

Solving equation (3.43) with the boundary conditions being $[\sigma_r]_{r=a} = 0$ and $[\sigma_r]_{r=b} = 0$ gives:

$$\sigma_r = -\frac{(3+\upsilon_{\theta r})\rho\omega^2 b^2}{9-N^2}\left\{\left(\frac{r}{b}\right)^2 - \frac{1-\left(\frac{a}{b}\right)^{N+3}}{1-\left(\frac{a}{b}\right)^{2N}}\left(\frac{r}{b}\right)^{N-1} - \frac{1-\left(\frac{a}{b}\right)^{-N+3}}{1-\left(\frac{a}{b}\right)^{-2N}}\left(\frac{r}{b}\right)^{N-1}\right\} \tag{3.44}$$

$$\sigma_\theta = -\frac{(3+\upsilon_{\theta r})\rho\omega^2 b^2}{9-N^2}\left\{\left(\frac{r}{b}\right)^2\frac{N^2+3\upsilon_{\theta r}}{3+\upsilon_{\theta r}} - N\frac{1-\left(\frac{a}{b}\right)^{N+3}}{1-\left(\frac{a}{b}\right)^{2N}}\left(\frac{r}{b}\right)^{N-1} - N\frac{1-\left(\frac{a}{b}\right)^{-N+3}}{1-\left(\frac{a}{b}\right)^{-2N}}\left(\frac{r}{b}\right)^{N-1}\right\} \tag{3.45}$$

$$u_\theta = \frac{1}{E_r}\frac{(3+\upsilon_{\theta r})\rho\omega^2 b^3}{9-N^2}\left\{\begin{array}{l} -\dfrac{1}{3+\upsilon_{\theta r}}\left(\dfrac{r}{b}\right)^3 + \dfrac{1}{N+\upsilon_{\theta r}}\dfrac{1-\left(\dfrac{a}{b}\right)^{N+3}}{1-\left(\dfrac{a}{b}\right)^{2N}}\left(\dfrac{r}{b}\right)^N - \\ \dfrac{1}{-N+\upsilon_{\theta r}}\dfrac{1-\left(\dfrac{b}{a}\right)^{-N+3}}{1-\left(\dfrac{b}{a}\right)^{-2N}}\left(\dfrac{r}{b}\right)^{-N} \end{array}\right\} \tag{3.46}$$

Where N is an orthotropic parameter and $N^2 = E_\theta / E_r$

In the numerical package considered the stress analysis principle is the similar to that mentioned. The stress-strain relationship is given by

$$\{\sigma\} = [D]\{\varepsilon^{el}\} \tag{3.47}$$

Where $\{\sigma\}$ is the stress vector, [D] is the elastic stiffness matrix and $\{e^{el}\}$ is the elastic strain.

Equation (3.47) can be resolved into

$$\{\varepsilon\} = \{\varepsilon^{th}\} + [D]^{-1}\{\sigma\} \tag{3.48}$$

Where $\{\varepsilon\} = \{\varepsilon^{th}\} + \{\varepsilon^{el}\}$ is the total strain vector, $\{\varepsilon^{th}\}$ is the thermal strain vector.

For a symmetric system, the matrix is given such that

$$\frac{\upsilon_{yx}}{E_y} = \frac{\upsilon_{xy}}{E_x} \tag{3.49}$$

$$\frac{\upsilon_{zx}}{E_z} = \frac{\upsilon_{xz}}{E_x} \tag{3.50}$$

$$\frac{\upsilon_{yz}}{E_z} = \frac{\upsilon_{yz}}{E_y} \tag{3.51}$$

This gives resulting solution for stress and strain as shown

$$\sigma_x = \frac{E_x}{h}\left(1-(\upsilon_{yz})^2\frac{E_z}{E_y}\right)(\varepsilon_x-\alpha_x\Delta T)+\frac{E_y}{h}(\upsilon_{xy})+\upsilon_{xz}\upsilon_{yz}\frac{E_z}{E_y}\overrightarrow{AB}(\varepsilon_y-\alpha_y\Delta T)+$$
$$\frac{E_z}{h}(\upsilon_{xz}+\upsilon_{yz}\upsilon_{xy})(\varepsilon_z-\alpha_z\Delta T) \tag{3.52}$$

$$\sigma_y = \frac{E_y}{h}\left(\upsilon_{xy}+\upsilon_{xz}\upsilon_{yz}\frac{E_z}{E_y}\right)(\varepsilon_x-\alpha_x\Delta T)+\frac{E_y}{h}\left(1-(\upsilon_{xz})^2\frac{E_z}{E_x}\right)(\varepsilon_y-\alpha_y\Delta T)+$$
$$\frac{E_z}{h}\left(\upsilon_{yz}+\upsilon_{xz}\upsilon_{xy}\frac{E_y}{E_x}\right)(\varepsilon_z-\alpha_z\Delta T) \tag{3.53}$$

$$\sigma_z = \frac{E_z}{h}(\upsilon_{xz}+\upsilon_{yz}\upsilon_{xy})(\varepsilon_x-\alpha_x\Delta T)+\frac{E_z}{h}\left(\upsilon_{yz}+\upsilon_{xz}\upsilon_{xy}\frac{E_y}{E_x}\right)(\varepsilon_y-\alpha_y\Delta T)+$$
$$\frac{E_z}{h}\left(1-(\upsilon_{xy})^2\frac{E_y}{E_x}\right)(\varepsilon_z-\alpha_z\Delta T) \tag{3.54}$$

$$\sigma_{xy} = G_{xy}\varepsilon_{xy} \tag{3.55}$$

$$\sigma_{yz} = G_{yz}\varepsilon_{yz} \tag{3.56}$$

$$\sigma_{xz} = G_{xz}\varepsilon_{xz} \tag{3.57}$$

Where $h = 1-(\upsilon_{xy})^2\frac{E_y}{E_x}-(\upsilon_{yz})^2\frac{E_z}{E_y}-(\upsilon_{xz})^2\frac{E_z}{E_x}-2\upsilon_{xy}\upsilon_{yz}\upsilon_{xz}\frac{E_z}{E_x}$

For axisymmetrical models, the transformation is given by

$$[D_{x-y-z}]^{-1} = \begin{bmatrix} 1/E_x & -\upsilon_{xy}/E_x & -\upsilon_{xz}/E_x \\ -\upsilon_{yx}/E_y & 1/E_y & -\upsilon_{yz}/E_y \\ -\upsilon_{zx}/E_z & -\upsilon_{zy}/E_z & 1/E_z \end{bmatrix} \tag{3.58}$$

Rearranging the transform into 3D elements using polar coordinate system gives

$$\left.\begin{aligned} E_x &= E_R \\ E_y &= E_Z \\ E_z &= E_\theta \\ \upsilon_{xy} &= \upsilon_{RZ} \\ \upsilon_{yz} &= \upsilon_{Z\theta} \\ \upsilon_{xz} &= \upsilon_{R\theta} \end{aligned}\right\} \quad (3.59)$$

It assumes that all the Poisson's ratios are major Poisons ratios.

In presenting the results for orthotropic materials, the most common failure criteria are the maximum stress, maximum strain and distortional energy. More results for profile one and two are given in the Appendix B.

3.7.1 Profile One Stress Analysis Results

For a specific structural load, the analysis predicts the stresses, strains, and displacements given the model and material of a part or an entire assembly. In this case, a rotational load of the maximum rotational speed of 25,000 rpm is applied. A general three-dimensional stress state is calculated in terms of three normal and three shear stress components aligned to the part or assembly world coordinate system. The simulated flywheel structure contains a 12.04 kg flywheel rotor, rotor disks with OD of 80mm, shaft length of 365 mm which contains hinges.

The shear stress is represented by σ_{xy} in equation (6.20) is shown in Fig. 3.14.

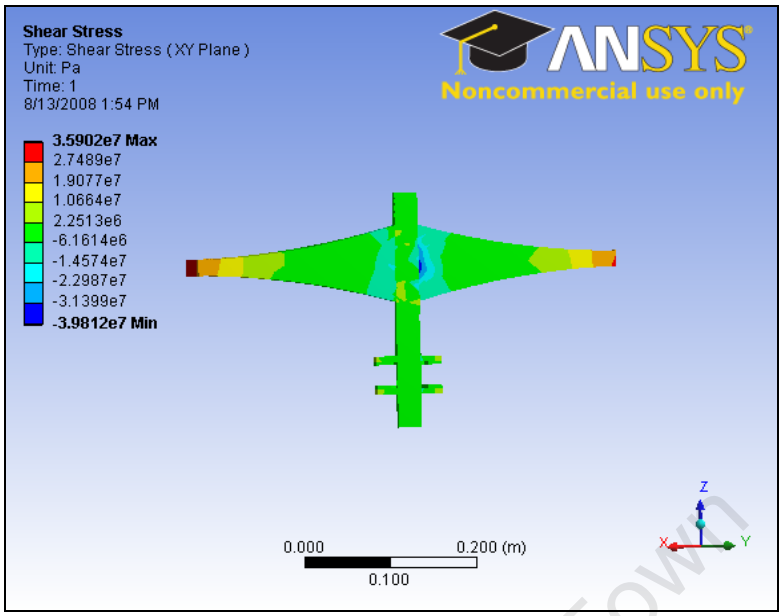

Figure 3.14: Shear stress distribution on XY plane for profile one

The shear stress was found to be 35.9MPa. This value is lower than the maximum tensile strength of the flywheel components used, that is, steel, composite fibre and the magnets.

According to elasticity theory, the principal stresses are the three normal stresses remaining after an infinitesimal volume of material at an arbitrary point on or inside the solid body can be rotated such that only normal stresses remain and all shear stresses are zero. This is represented in Fig. 3.15 which shows the normal stress.

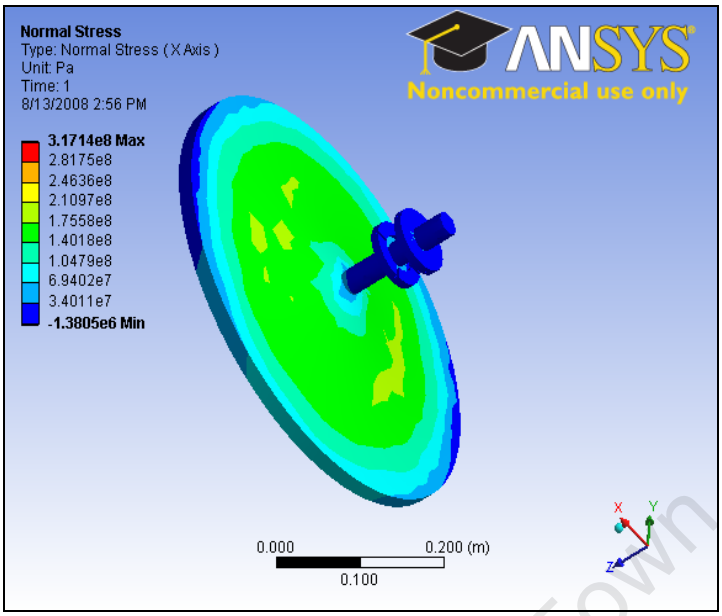

Figure 3.15: Normal stress of profile one

3.7.2 Profile Two Stress Analysis Results

An analytical stress approach was considered when designing this profile as shown in chapter 2. This profile is based on the inertial mass and angular speed required to store a specific amount of energy without failure. A numerical stress analysis was performed to ensure the maximum allowable strength was not exceeded. Fig. 3.16 and 3.17 show the normal shear stress exerted on the flywheel system when a rotational load of 25,000 rpm is applied. The simulated flywheel structure contains a 14.987 kg flywheel rotor, rotor disks with OD of 170 mm, shaft length of 365mm, spacers in between the rotor disks.

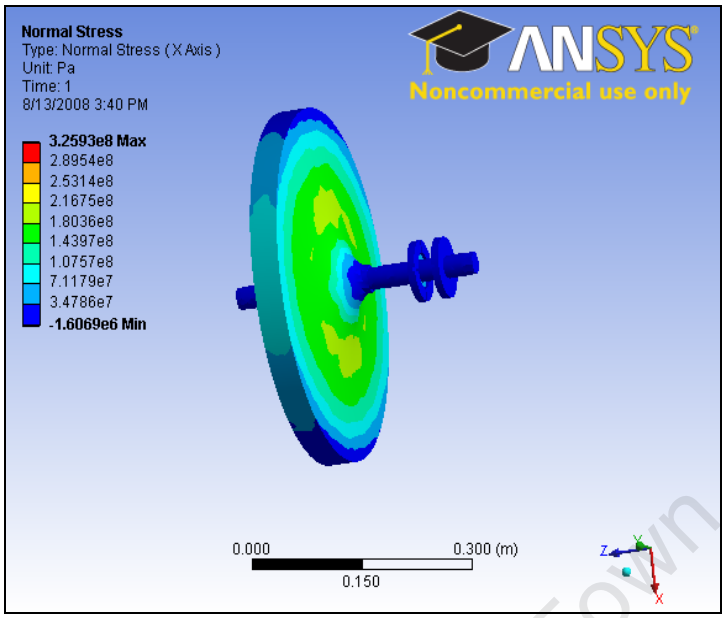

Figure 3.16: Normal stress of profile two

The maximum normal stress occurs between the centre of the flywheel rotor and the shaft. This results from the radial elongation between the shaft and flywheel as these two adjoined components have different young's modulus. This could result into dynamic instability of the system as the shaft could create excessive unbalanced forces on the bearing structure.

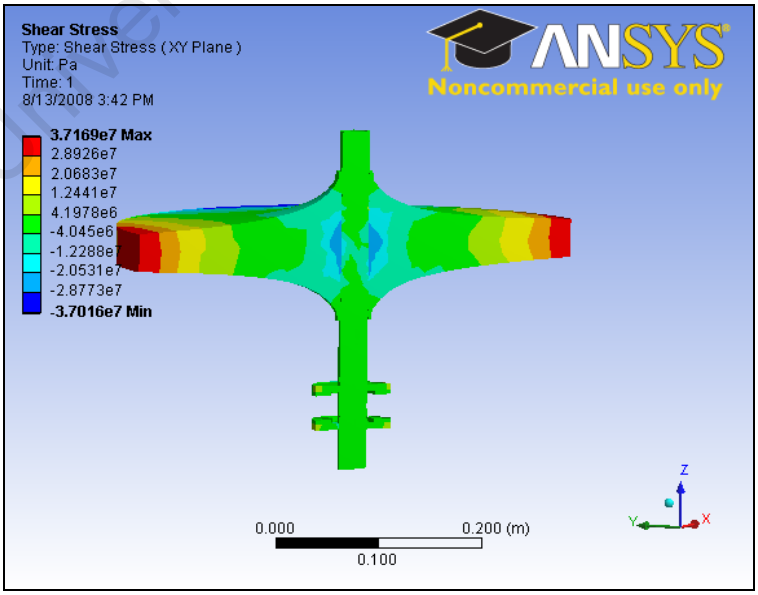

Figure 3.17: Shear stress distribution of profile two

The maximum shear stress occurs at the peripheral of the flywheel rotor. The magnitude, given as 37 MPa is low as compared to the maximum strength of the system. From the numerical stress analysis, it can be noted that the profiles one and two can withstand the high stresses exerted during high speed operation.

3.8 Analysis of Profile Two with Modifications

During the prototyping phase, a few adjustments were made to the flywheel rotor profile two. This was done to ease on the manufacturing as elaborated in chapter 4. This hence required new simulations. Other modifications made include:

- Central hole made larger from 1mm to 3mm
- Elastomeric layer used for shaft to reduce on the flywheel radial elongation. Central hole was changed from 30mm to 35mm to accommodate the layer.
- A new machine (500W) was used to run the flywheel. The system consists of rotor disks with OD of 170mm with an overhang with grub screw and two aluminium retainer rings.
- A new stainless steel shaft with a key way and spacers was also considered.
- The modified flywheel rotor changed from 14.987kg to 17.6kg mass.

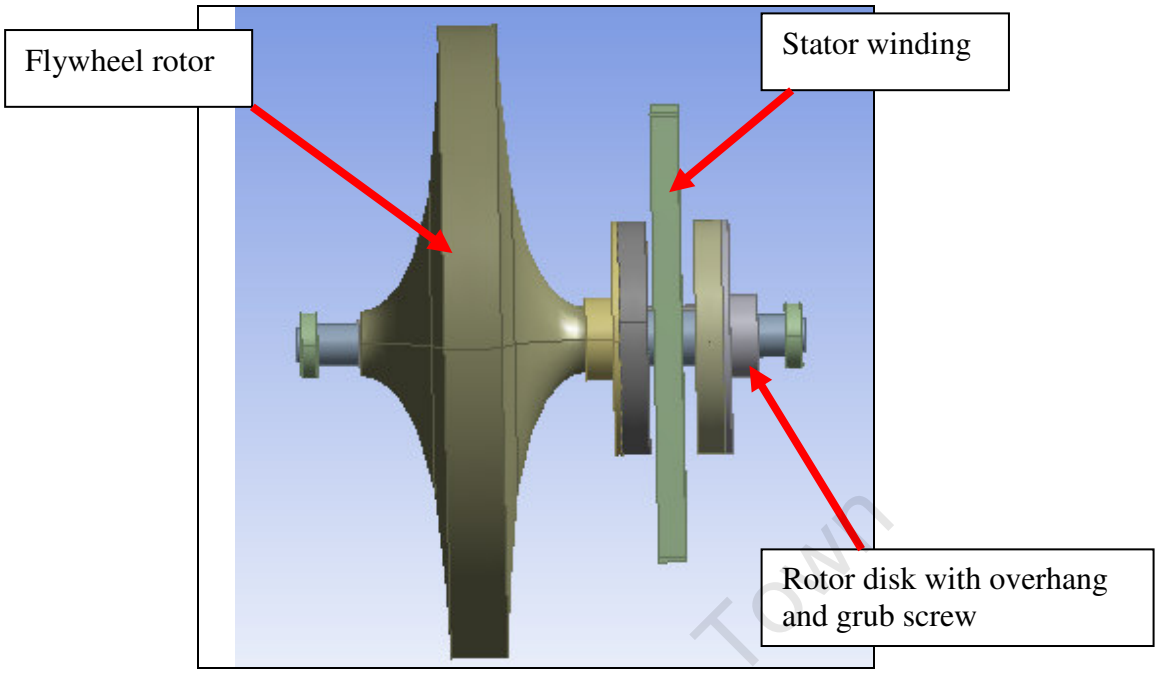

Figure 3.18: Profile two with modifications

Stress and modal analysis were performed on the modified integrated flywheel, shaft and machine. The results are discussed below. The combination of both isotropic and orthotropic materials in the combined system means that Von Mises failure will not be used for predicting failure. Maximum stress, maximum strains among others are commonly used failure criteria [3.27] and will be used to predict structural performance of the flywheel system. The simulated flywheel structure contains a 20 kg flywheel rotor, rotor disks with OD of 170mm, shaft length of 365mm, spacers in between the rotor disks

3.8.1 Numerical Stress Analysis

The two stress and strain results used for post processing are the maximum shear stress and maximum principal stress. More of the results are given in the Appendix B and these include the maximum principal strain, normal stress, shear stress.

The maximum shear stress τ_{max}, is given as in equation (3.60) [3.19].

$$\tau_{max} = \frac{\sigma_1 - \sigma_3}{2} \tag{3.60}$$

Where σ_1 is the first principal stress and σ_3 is the third principal stress.

The derivation of the maximum shear stress can also be explained using Mohr's circle. The simulation results from applying a rotational load on the modified systems are shown in Fig. 3.19-3.20.

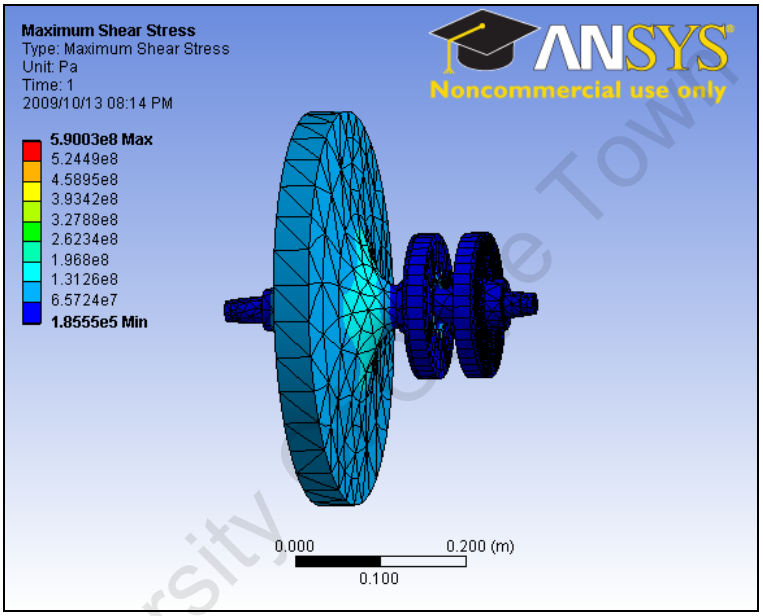

Figure 3.19: maximum shear stress of modified profile two

The maximum tensile strength of the material used in the flywheel is 484 MPa with a safety factor. The 3D result shows a maximum shear stress of 590 MPa which is higher than the nominal strength. However, on closer observation as shown in Fig. 3.20, the high stresses originate from the centre of the flywheel system.

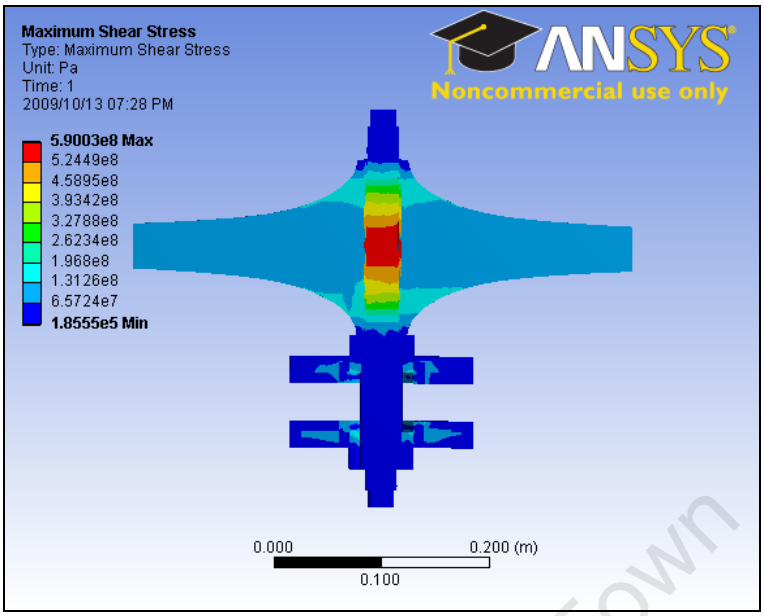

Figure 3.20: 2D maximum shear stress of modified profile two

This is attributed to the modelling of the elastomeric layer and interference fit. In addition, the increased mass of the flywheel rotor stretches the shaft. Fig.3.21 and 3.22 show the maximum principal stress.

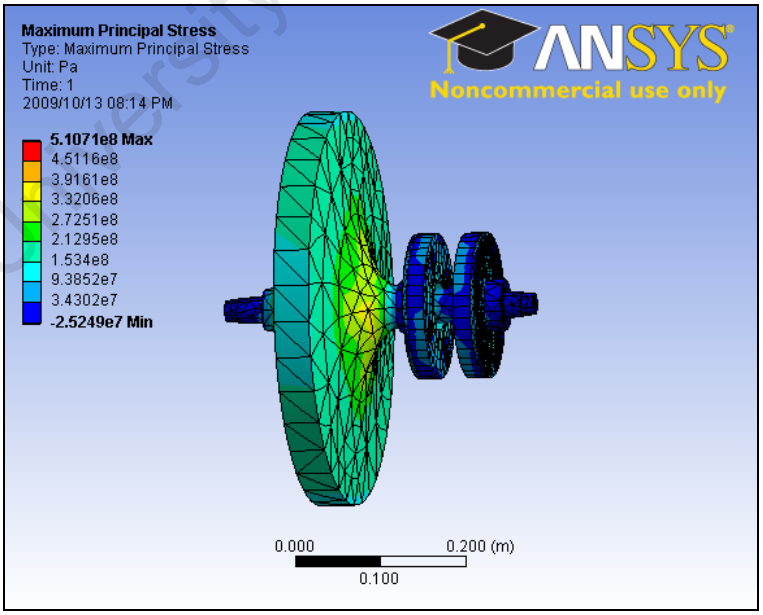

Figure 3.21: maximum principal stress of modified profile two

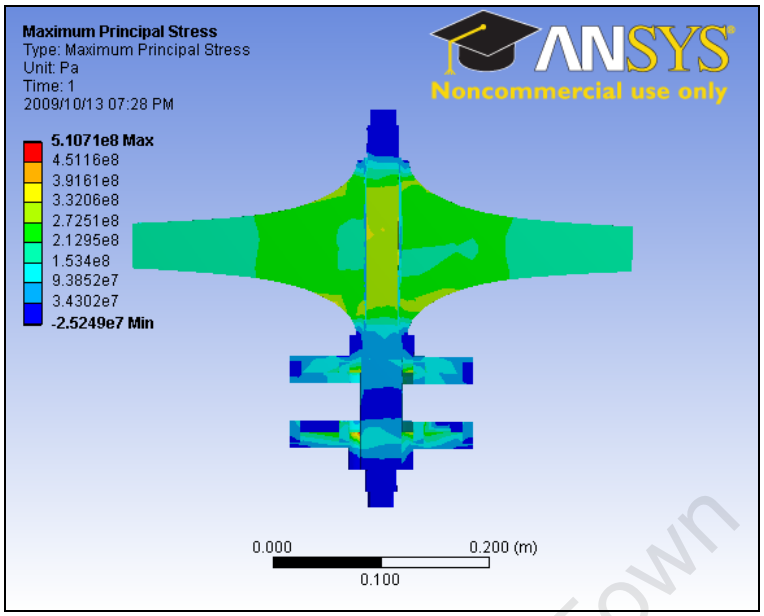

Figure 3.22: Maximum principal stress of modified profile two

It is observed from Fig. 3.22 that the maximum stress is higher than the nominal strength however; the average stress all over the flywheel system is approximately 332 MPa. The sporadic high stresses are a result of modeling and non-linearity which could occur experimentally.

From the simulations, it was observed that a more high strength with adjoining Young's modulus be considered to reduce the high stresses at the interface of the rotor and shaft. Most importantly, the design parameters used for simulations are for 66% glass content yet the final product was manufactured with 70-74% fibre content. This was possible using the technique mentioned in the prototyping section.

3.8.2 Numerical Modal Analysis

The results of the numerical modal analysis for the modified system are presented in the Fig. 3.23 and 3.24. The free vibration and pre-stressed modal analysis results are presented. The first significant deformation is the fourth mode happening at 232.58HZ.

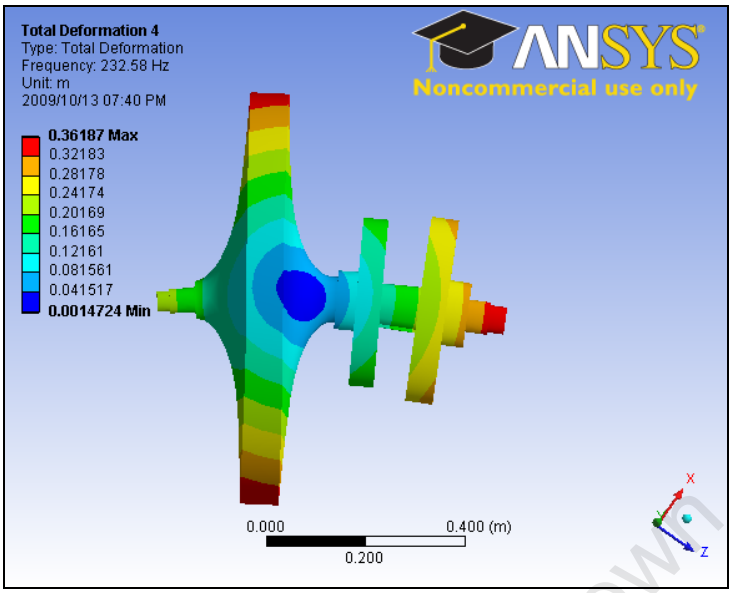

Figure 3.23: Free vibration total deformation at 232.58HZ

The fifth mode happens close at 235.87HZ which corresponds to an angular speed of 1,481 rad/s. This means as the system accelerates through to the maximum operating speed; it would ramp through a resonant. For the pre-stressed modal analysis, the first significant resonance happens at 369.72HZ as shown in Fig. 3.24.

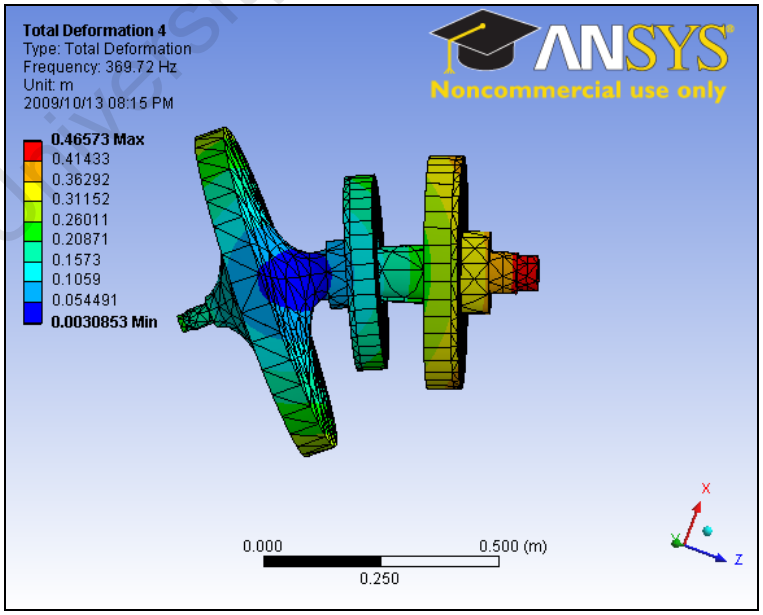

Figure 3.24: pre-stressed total deformation at 369.72HZ

There is a significant difference in the simulation results of the two systems. The modifications in the flywheel, shaft and electrical machine resulted in changes in the system. The first resonances happen in the operating speed range of the flywheel system. However, the deformation and strain do not interfere with the containment structure as this was designed with a good clearance. This can be solved by expanding the operating speed range to avoid resonance. The advantage of this is the following resonances occur far beyond the maximum operating speed. However, this would mean reducing the safety margin of the system.

The discrepancy from the previous design results arise from:

- Increased mass portions on the flywheel rotor
- Increased shaft mass, rotor disks and magnets
- Change in stiffness of the bearing structure used
- Also, the inclusion of the key way
- Change in material properties

3.9 Concluding Remarks

This chapter explains the various flywheel system topologies. The pros and cons of each are given. The flywheel rotor profiling, which is a critical element in flywheel design is given. Two methodologies are given to derive the profiles with low stress rotors. The parameters and shapes are used to manufacture the flywheel rotors as shown in chapter 4.

3.10 References

[3.1] P. I. Tsao, "An integrated flywheel energy storage system with a homopolar inductor motor/generator and high-frequency drive," Ph.D Thesis, U.C. Berkeley, September, 2003.

[3.2] G. Rui, "Magnetic bearings for flywheel energy storage," MSc Thesis, Clarkson University, 2008.

[3.3] S. Robert, Wesibach, G.G. Karady and R. G. Farmer, "A combined uninterruptible power supply and dynamic voltage compensator using a flywheel energy storage system," *IEEE Transactions on Power Delivery*, vol. 16, April 2001.

[3.4] F. J. M. Thoolen, "Development of an Advanced High speed Flywheel for Energy Storage System," PhD thesis, Eindhoven University of Technology, 1993.

[3.5] F. N. Werfel, U. Floegel-Delor, T. Riedel, R. Rothfeld, D. Wippich, B. Goebel, G. Reiner, and N. Wehlau, "A compact HTS 5 kWh/250 kW flywheel energy storage system," *IEEE Transactions on Applied Superconductivity*, vol. 17, No. 2, June 2007.

[3.6] G. Genta, *Kinetic Energy Storage, Theory and Practice of Advanced Flywheel Systems*, Butterworth & Co. Ltd; 1985.

[3.7] S. Kitade, "Comprehensive composite materials," chapter 6: flywheel, vol. 6, *Elsevier*, pp.571-580, 2000.

[3.8] S. Ginter, G. Gisler, J. Hanks, D. Havenhill, W. Robinson and L. Spina, "Spacecraft energy storage systems," NAECON, 1997.

[3.9] R. F. Post, T. K. Fowler, S. F. Post, "A high efficiency electromechanical battery," in *Proceedings of the IEEE*, vol. 81, No.3, March 1993.

[3.10] M. Berger and I. Porat, Optimal design of rotating disk for kinetic energy storage, Faculty of mechanical engineering, Technikon-Israel institute of technology, Haifa Israel.

[3.11] G.R. Kress, "Shape optimization of a flywheel," *Struct. Multidisc. Optim*, vol. 19 No.1, pp. 74-81, 2000.

[3.12] J.M. Chern, W. Prager, "Optimal design of rotating disk for given radial displacement of edge," *Journal of optimization theory and applications*, vol. 6, no. 2, 1970.

[3.13] D. Eby, RC Averill, "An injection island GA for flywheel design optimization," Artificial Intelligence in Engineering, design, analysis and manufacturing, vol. 13, pp. 389-402, 1999.

[3.14] D. Johnson, "Design considerations and implementation of an electromechanical battery system," Ph.D. dissertation, Dept. Electrical Engineering, University of Cape Town, 2008.

[3.15] S.Timoshenko, *Strength of Materials*. Huntington, N.Y: R. E. Krieger Pub. Co, 1976.

[3.16] J.H. Faupel, F.E Fischer. Engineering Design, a Synthesis of Stress Analysis and Materials Engineering. 1st ed. New York: Wiley; 1964.

[3.17] D. Hartog, J. Pieter. *Advanced strength of materials*. Network McGraw-hill: 1952.

[3.18] A. Stodola. *Steam and gas turbines*. McGraw-Hill Book Company, Inc; 1927.

[3.19] ANSYS, Inc *Theory Reference*, ANSYS Release 9.0.002114. SAS IP Inc

[3.20] B. T. Murphy, J. R. Kitzmiller, R. Zowarka, J. Hahne and A. Walls, "Rotordynamics and test results for a model scale compulsator rotor, " *IEEE Transactions on Magnetics*, vol. 37, issue 1, pp. 310-313, 2001.

[3.21] J. D. Ede, Z. Q. Zhu, and D. Howe, "Rotor resonances of high-speed permanent-magnet brushless machines," *IEEE Transactions on Industry Applications*, vol. 38, No. 6, Nov/Dec. 2002.

[3.22] R.J. Wang, D.G. Shang , L.C. Li, and C.S. Li, "Fatigue damage model based on the natural frequency changes for spot-welded joints," *International Journal of Fatigue*, vol.30, pp. 1047–1055, 2008.

[3.23] D. Hartog, *Mechanical Vibrations*, 4th ed., New York: McGraw-Hill, 1956, pp.285-337

[3.24] W. Cai and P. Pillay,"Resonant Frequencies and Mode Shapes of Switched Reluctance Motors," *IEEE Transactions on Energy Conversion*, vol. 16, no. 1, march 2001.

[3.25] E. Kramer. *Dynamics of Rotors and Foundations*. New York: Springer-Verlag, 1993.

[3.26] E. L. Danfelt, S. A. Hewes, T. W. Chou, "Optimization of composite flywheel design," *Int. J. Mech sci*, vol.19, pp. 69-78, 1977.

[3.27] G. Genta, *The shape factor of composite material filament wound flywheels. Composites*, IPC Business press Ltd, April 1981.

Chapter 4

Prototyping of System Components

This chapter discusses the procedure manufacturing the flywheel rotor, rotor disks and stator windings of the system.

4.1 Introduction

In chapters two and three, the designs of the flywheel components were discussed. This chapter describes the manufacturing procedure of the flywheel rotor and electrical machine. The major problems faced during construction are described.

4.2 Flywheel Rotor Construction

There are various methods that have been used in manufacturing composites for flywheel rotors [4.1-4.3]. The failure of these structures is dependent on a number of parameters. For example, the single-material, circumferentially-wound composite rims suffer from limited inner to outer radius ratio range. The solid disks with single or multi-oriented fibres with radial profiles are hindered by stress concentrations on the surfaces, have complex shaft attachment and are expensive to manufacture.

Composite structures with radially thin rims made by winding high strength fibres in the circumferential direction which achieve higher specific energy than other composite structures [4.4]. These rims are easily manufactured with low cost

however thicker rims cannot be achieved due to limited radial strength [4.5]. In addition, the radial growth of the flywheel against the shaft is essential especially with a metallic shaft. With this technique, the successive layers can be oriented differently from the previous layer to vary performance of the composite structure.

Circumferentially wound rings can be improved by reducing the radial stress and also by improving the radial strength. In the single rim, the energy density can be increased by:

- Increasing the ratio of circumferential Young's modulus to mass density, Eh/q, with increasing radius.
- Pre-stressing the filament wound rims to induce residual radial compressive stresses.

Thicker rims can be achieved in this technique by increasing the radial strain to failure and decreasing the radial Young's modulus of a filament wound composite rim. The radial stress can be reduced by using multi ring filament wound rims. These are the most commonly used for commercial flywheel rotors and achieve high energy densities. In addition, these multi-ring rotors exhibit natural frequencies far beyond the operating speed range [4.6]. Choosing two rings of different materials can change the stress distribution enormously. However, residual thermal stresses are often a sizeable percentage of the radial tensile strength of the composite and must be accounted for [4.5] [4.7].

The radial strength can also be improved by using layered laminates, woven fabrics among others; however this complex fibre laying can lead to delamination and micro cracking at relatively low stress levels [4.8] [4.9].

A woven ribbon was developed in ETH Zurich for small power application flywheels [4.3]. With this technique, unidirectional fibres under large pretension on the hub is pre-stressed by winding the fibres. Stress distribution is optimized by

varying the pretension. Energy densities to a tune of 100Wh are realised with this approach.

In this particular research, the profiles of the flywheels are liable to homogeneity problems, balancing concerns and inclusion of a central hole which creates a dynamic instability problem. The two approaches considered in this thesis include casting and the layered and are discussed in the following sections.

4.2.1 Development of the Cast Flywheel Rotor

This process was considered using chopped fibre which results in better homogeneity of the end product. However, the length of the fibre is critical as short fibres do not reinforce as effectively as long or continuous fibres [4.10]. The advantages of short fibre composites are that they can be easily formed into complex shapes, by casting, injection, layering and spraying [4.11]. Fibres longer than the minimum critical length are only marginally weaker than a continuous fibre composite and were not considered for this design. This is particularly of interest in this research as complex shapes are used to derive the required stress distributions and material optimization. In addition, the critical length of a fibre is determined by evaluating the process of load transfer**.** The load transfer mechanism results in end effects which may reduce the fibre stress as shown in Fig. 4.1.

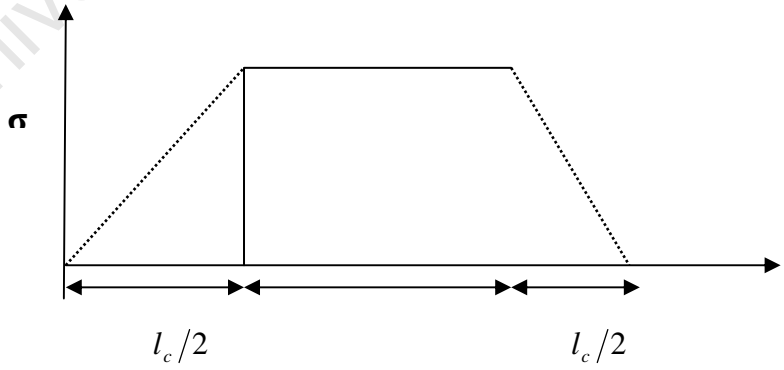

Figure 4.1: Stress distribution over a short fibre

The alignment of the short fibres is also difficult to control and randomly-oriented short fibres cannot be packed at such high volume fractions as continuous fibres. At fibre ends, the strain in the matrix is higher than in the fibre and the load to the fibre is transferred through the shear strength between the fibre and the matrix interface.

When a stiff fibre is embedded in a relatively flexible matrix, shear stress and strain are a maximum at the fibre ends. The tensile stress, on the other hand, is zero at the fibre end and increases towards the centre. A fibre is said to be of the critical length if it is just long enough for the tensile stress to reach its maximum value. Considering a half fibre, the maximum tensile force in the fibre with a diameter, D is balanced by the shear force at the fibre/matrix interface giving:

$$\sigma_f^{\max} \frac{\pi D^2}{4} = \frac{\tau \pi D L_c}{2} \tag{4.1}$$

$$L_c = \frac{\sigma_f^{\max} D}{2\tau} \tag{4.2}$$

$$\lambda_c = \frac{L_c}{D} = \frac{\sigma_f^{\max}}{2\tau} \tag{4.3}$$

Critical fibre as defined in [4.12] thus depends on τ, the interfacial or matrix shear strength, and varies according to both fibre and matrix and because of the low stress at fibre ends, the average stress in the fibre will be lower than that in a continuous fibre, even if it is longer than the critical length. The interface between fibre and matrix is crucial to the performance of the composite. For example, weak interfaces provide a good energy absorption mechanism however the composite results having low strength and stiffness with high fracture toughness. Strong interfaces on the other hand provide strong, stiff but brittle composites.

There are various mechanisms that explain the nature of adhesion between fibre and matrix and these can be explained as follows. *Adsorption and wetting* involves accumulation of atoms or molecules on the surface of the material and this depends

on the surface energies of the two surfaces. Glass and carbon are readily wetted by epoxy and polyester resins, which have lower surface energies. *Interdiffusion (autohesion)* - diffusion and entanglement of molecules: *Electrostatic attraction* - important in the application of coupling agents. Glass fibre surface may be ionic due to oxide composition: *Chemical bonding* - between chemical group in the matrix and a compatible chemical on the fibre surface: *Mechanical adhesion* - depending on degree of roughness of fibre surface.

In this process, a high strength rotor design with a good safety factor can be achieved as the resulting strength of the shape which is approximately half of the unidirectional laminate. For an even fibre distribution and orientation, the main cause of failure is fibre pullout which is defined as:

$$W_{fp} = \left(\frac{l_c}{l}\right)\frac{\pi d \tau\, l_c^2}{24} \tag{4.4}$$

Where W_{fp} is the fibre pullout work, l_c is the critical fibre length, l is the fibre length, d is the fibre diameter and τ is the maximum interface shear stress

The number of fibres per volume fraction can be written as.

$$N = \frac{V_f}{\pi \cdot d^2} \tag{4.5}$$

Where N is the number of fibres, V_f is the volume fraction and d is the fibre diameter.

Multiplying equation (4.4) with (4.5) gives the total amount of work as:

$$W_{fp} = \frac{\tau V_f l_c^3}{24ld} \tag{4.6}$$

The master plugs for the profiles designed in chapter two were machined from supawood as shown in Fig.4.2 and 4.3. Supawood is an inexpensive wood product which is often used for making plugs for composite manufacture.

Figure 4.2: Hyperbolic profile mould

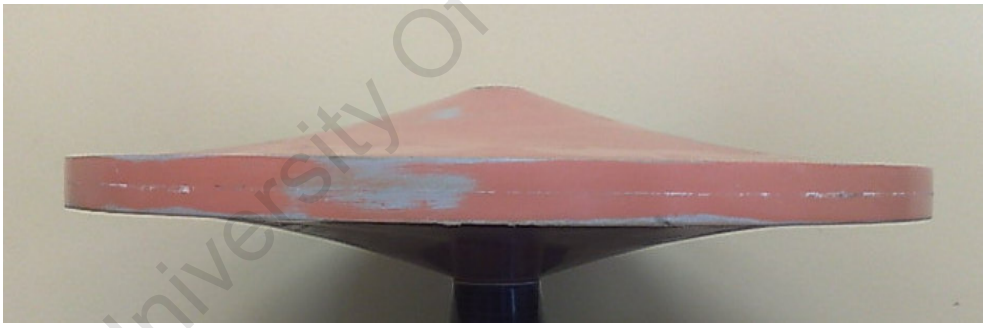

Figure 4.3: Optimal profile mould

The parts were over sized by 3mm, in order to allow for shrinkage. Two female moulds were then made using the master plugs as the manufacture of the flywheel rotor in one piece was cumbersome, especially with the heat generated during curing of the thick centre section as shown in Fig. 4.4.

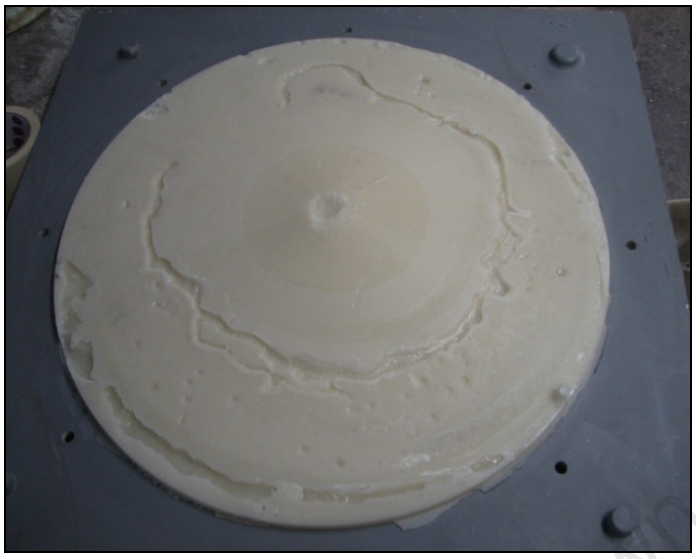

Figure 4.4: Failed manufacture of optimal shape

The mould surface was coated with a release agent, wax. The E-glass short fibres and epoxy resin were measured, mixed and poured into the moulds. The heating problem was solved partially by splitting the flywheel in two halves and this reduced the cracking significantly as in Fig. 4.5.

Figure 4.5: Optimal shape after completion without central hole

Once the E-glass/epoxy composite had cured, the two halves were surfaced and glued together with a milled fibre-epoxy composite. This did not affect the strength of the structure, as all the stresses were limited to the plane of rotation i.e. perpendicular to the axis of rotation. Using this method, other flywheels can be manufactured inexpensively, given the basic tools and skills. For a mass produced flywheel of unique profiles, the moulds can be inexpensively manufactured with aluminium moulds.

The benefits of this method of manufacturing the flywheel are that the special shape yields a higher SKE, reduced material cost and lower overall cost of production.
As a result of the complexity in manufacture, only 30-40% fibre was used. This significantly reduced the ultimate strength of the composite flywheel. For the casting profiles, the stainless steel shaft was press-fitted onto the flywheel as in Fig. 4.6.

Figure 4.6: Hyperbolic profile after manufacture with shaft

Further, during the manufacture, the areas around the flywheel cracked. This was attributed to the thin layer around the hole and the low percentage of fibre in the composite. Increasing the size of central hole wall was considered in the layered flywheel to eliminate the cracking.

4.2.2 Development of the Layered Flywheel Rotor

This is also called the laminating method and is mainly considered to improve the radial strength created when using the filament wound. This method makes use of a vacuum and autoclave assisted resin transfer moulding process. The flywheel was manufactured using layers of woven fibre glass and epoxy resin to a fibre to resin ratio of at least 70-74%. The woven fibre is layered in several directions to improved strength in all directions with acceptable thickness levels. The final geometry is then CNC machined to specification.

In the first instance, the fibre was layered and resin injected. Due to the viscosity of the resin and compactness of the fibre, the resin was not able to penetrate the entire flywheel. This created voids in the product. To eliminate the reoccurrence of the voids, the profile was subdivided into six parts as shown in Fig. 4.7.

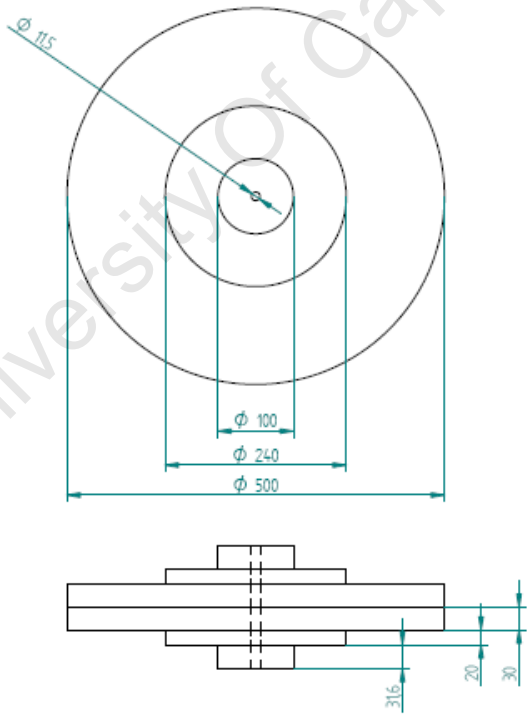

Figure 4.7: Six parts of hyperbolic profile for easy manufacture

The six parts were manufactured separately and joined using high strength adhesive. This was sufficient to withstand the axial forces exerted on the flywheel. The profile was then CNC machined to create the profile shown in Fig. 4.8.

Figure 4.8: Complete hyperbolic profile using layered technique

With this technique, a high fibre to resin ratio was achieved. The final product had an inner diameter of 35mm, outer diameter of 460mm with a mass of 17.6kg. The increased inner diameter meant a change in the shaft connection used. An elastomeric bushing was utilised to reduce on the radial elongation between the flywheel and shaft. These bushings for shaft-flywheel connections have been explored in [4.3] [4.10] with no inherent problems.

4.2.3 Static and Dynamic Balancing

In practice, constructing a well balanced rotor is difficult. There are usually residual masses which cause the centre of gravity not to coincide with the nominal geometrical centre and the rotational axis not to coincide with the principal axes of inertia. The unbalance occurs as static and dynamic unbalance. Static balancing is a state of balance existing such that the body exhibits equilibrium under the action of static forces. The unbalance due to static forces is expressed as $mu\omega^2$. Dynamic balance exists when a mass is distributed about an axis of rotation such that it does

not have a tendency to displace the axis of rotation when subjected to rotational forces. The dynamic results into a moment $(J_t - J_p)\chi\omega^2$.

Consider a rotor rotating about an axis at an angle χ. If the principal inertia is *z*, then the angular moment $\overline{H}$ is [4.13]:

$$\overline{H} = J_p \omega \cos\chi\, \bar{k} - J_t \omega \sin\chi\, \bar{i} \tag{4.7}$$

Differentiating with respect to time

$$\frac{d\overline{H}}{dt} = J_p \omega \cos\chi \frac{d\bar{k}}{dt} - J_t \omega \sin\chi \frac{d\bar{i}}{dt} \tag{4.8}$$

$$\frac{dH}{dt} = -\omega^2 (J_t - J_p) \sin\chi \cos\chi\, \bar{j} \cong -\omega^2 (J_t - J_p)\chi\, \bar{j} \tag{4.9}$$

Where $\frac{di}{dt} = \overline{\omega} \times \bar{i} = \omega \cos\chi\, \bar{j}$ and $\frac{dk}{dt} = \overline{\omega} \times \bar{k} = \omega \sin\chi\, \bar{j}$

This gives $\overline{M} = \frac{d\overline{H}}{dt} = \omega^2 (J_t - J_p)\chi\, \bar{j}$ (4.10)

Static and dynamic balance is achieved by adding or removing a mass from the flywheel in both planes perpendicular to the axis of rotation. In this case, the flywheel is considered as a rigid body. Static and dynamic balancing was done on both profiles to reduce vibrations, noise and maintain the bearing life as in Fig. 4.9.

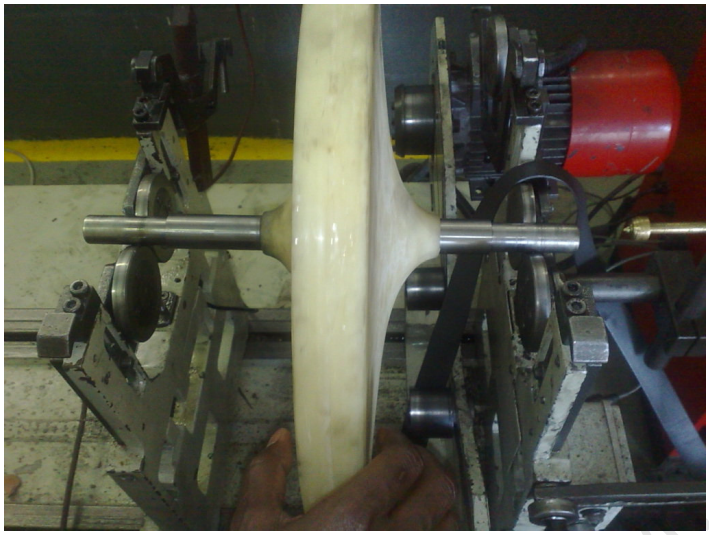

Figure 4.9: Flywheel with shaft being balanced

It was noted that profile two was more unbalanced and this was attributed to the poor fibre distribution at the thick edges of the profile. Table 4.1 gives the balancing results.

Table 4.1: Balancing results of the flywheel profiles

	Casting		**Layered**
Parameters	**Profile 1**	**Profile 2**	**Profile 2**
Specifications	ISO 1940		
Grade	G2.5		
Speed	2,000 rpm		1,000 rpm
Unbalance, left	14gr	35gr	10gr
Unbalance, right	0gr	0gr	0gr
Residual unbalance, left	0.02gr	0.02gr	0.1gr
Residual unbalance, right	0gr	0gr	0gr

gr- grams

4.2.4 Comparison of Casting and Layered Manufacturing Techniques

The two manufacturing techniques were considered so as to reduce the cost of the overall system without compromising on the structural integrity. Two flywheel rotors of different profiles were considered for the casting while only profile two was considered for the layered technique. The amount of fibre to resin ratio was found to be between 30 to 34% in the casting technique as compared to the layered technique with 70 to 74% fibre to resin ratio. It was realised that the casting approach was not able to withstand high stresses however, this technique was five times less expensive to manufacture as compared to the layered technique. Improvements in the casting technique can increase the strength of the composites for mass production. Use of aluminium moulds and vacuum bagging can considerably increase the strength. The stainless steel connections of the two profiles manufactured using the casting technique were pres-fitted while the shaft of the layered profile two flywheel was connected using an elastomeric layer.

4.3 Electrical Machine Construction

Two machines were constructed, a 100W, 36V and a 500W, 150V all with a current rating of 10A. Design and construction concerns realised in the 100W machine were used to improve on the structural integrity of the 500W machine. The details of the problems are mentioned in chapter 6. Both electrical machines are AFPM with BLDC mode of operation. The major components in the machine are the rotor disks containing PMs and the stator windings.

4.3.1 Rotor Disks

In the 100W machine, the rotor consists of two disks containing NdFeB magnets. The rotor disks were constructed with 300WA low carbon steel and are 84mm in diameter. The design is a four pole machine that uses arc magnet segments with a

thickness of 10mm, outer diameter of 80mm and inner diameter of 40mm. They are galvanized NdFeB magnets. These were glued onto rotor disks and epoxy resin was poured into the spaces between the PMs which improved the retention of the magnets. The position of the PMs is further reinforced by placing a stainless steel sleeve around the disk and the disks are press fitted onto the rotor shaft. The PMs are galvanized NdFeB as shown in Fig. 4.10.

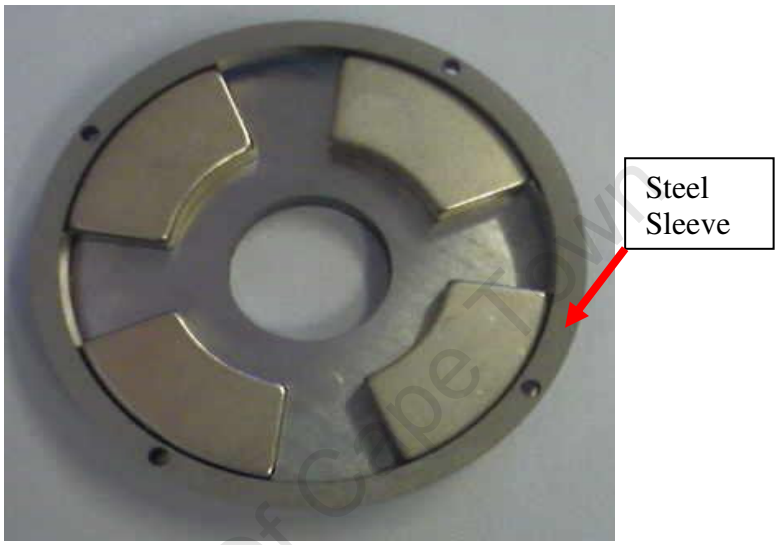

Figure 4.10: Rotor disks with PM and reinforced sleeve

The two disks are arranged to create a NS arrangement as stipulated in the design. The attractive forces from the magnets are contained with use of shoulders in the shaft design. The flux paths from the one pole through the windings to the second disk and through the back iron.

The rotor of the 500W machine is derived using the same methodology. The rotor disk is 150mm OD, 80mm ID, arc segment of 75^{o}, 10mm thick made from high strength carbon steel. The magnets are grade 40 (maximum energy product 40MGoe), NiCuNi plating with operating temperature of 120^{o}C.

Changes in the new rotor include:

- Key way to improve on rotor/shaft connection
- Aluminium sleeve to reduce weight
- Overhang with grub screw for improved balancing and adjustable air gap

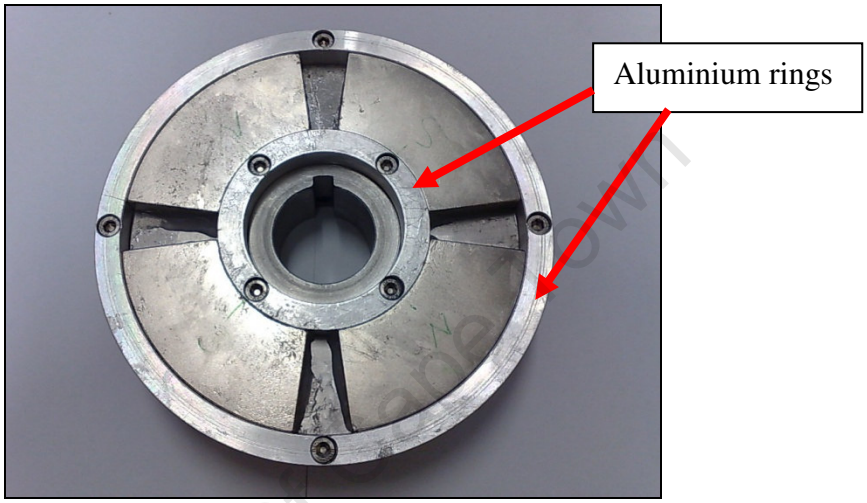

Figure 4.11: complete rotor disk structure

4.3.2 Stator Windings

A coreless stator was considered to eliminate core losses. Concentrated windings were used to produce a flat back EMF waveform. Two stators were considered for the two machines.

The 100W stator was wound using two strands of 0.8mm copper wire. This was considered as winding 1.6mm copper wire was found to be complex and could lead to voids in the windings. The stator is a double layer each with six coils each with 32 turns per coil. The each coil was wound separately, and then a star connection was made with two coils per phase in parallel. The stator windings were then placed in a mould and epoxy resin applied. The epoxy was left to cure at ambient temperature as shown in Fig. 4.12.

The stator for the 500W machine was constructed from a 1.6mm conductor size with class H insulation. It has the same number of coils per phase with 16 turns per coil with voltage of 150V. Thermal couples were placed on each phase before the epoxy was poured onto the winding.

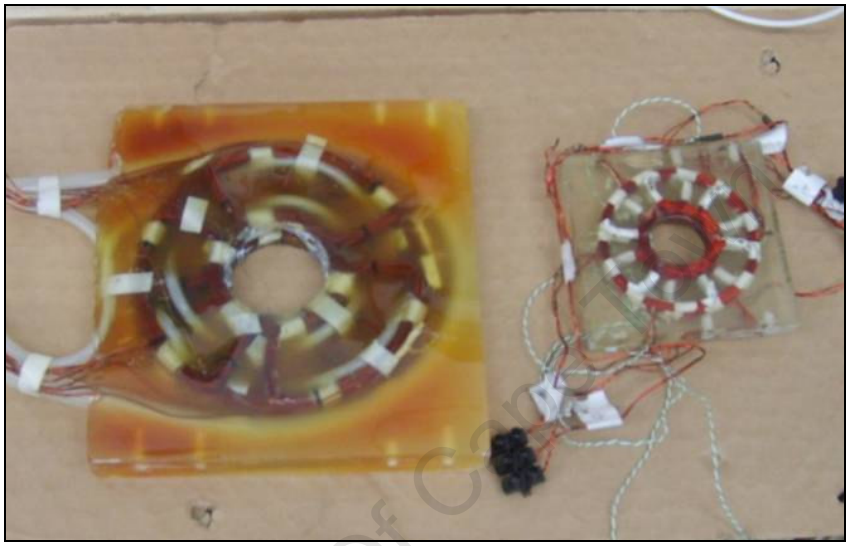

Figure 4.12: Comparison between two stators

4.3.2 Stator Holding Structure

In this system configuration, the rotor disks are fixed on to the stainless steel shaft coupled to the flywheel rotor. The levitating component is the stator winding hence the need for a holding structure. This was made from stainless steel to prevent interference of the magnetic path. This structure also acts as conductive path for the heat from the stator windings. Fig. 4.13 shows the structure.

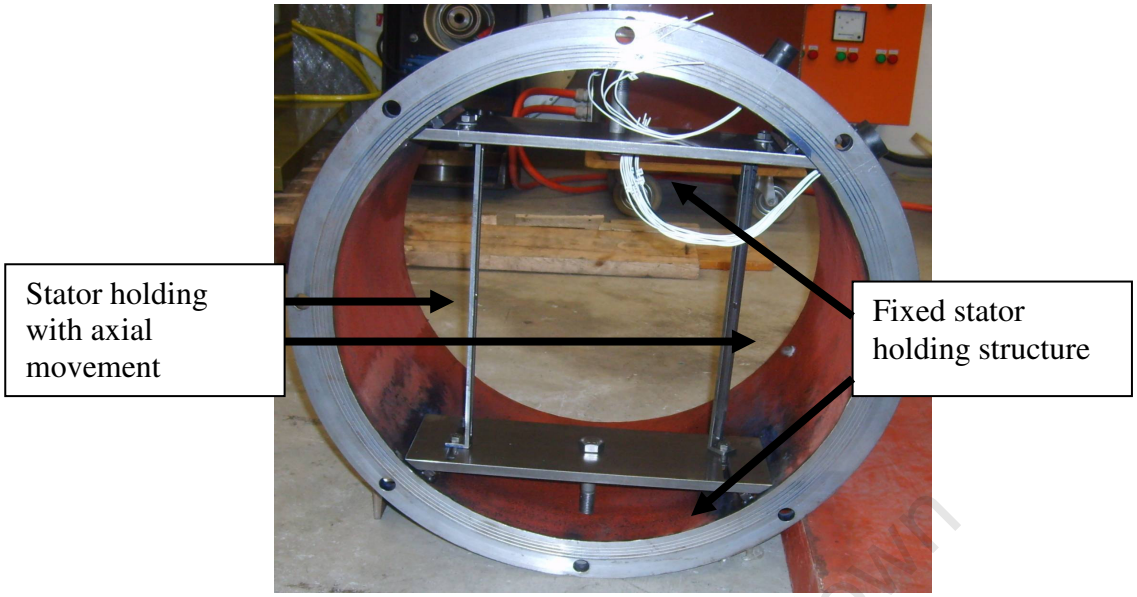

Figure 4.13: Stator holding structure

4.4 Assembly of Flywheel System

For safety concerns the flywheel system was tested in a vacuum containment system as shown in Fig. 4.14. All the assembly components are stand alone units. The power and signal cables are taken through circular connectors. The power cables are isolated from the signals to avoid interference. The details of the flywheel system combinations is shown in chapter 6 with the results.

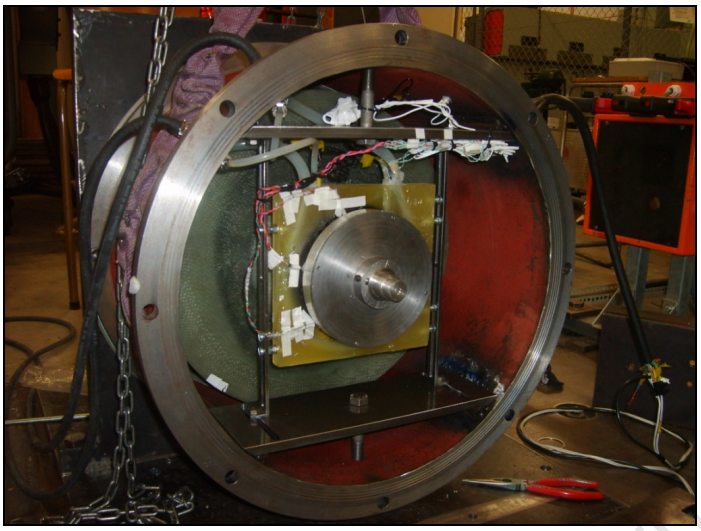

Figure 4.14: Assembly of the flywheel system.

4.5 Concluding Remarks

This chapter presented the prototyping of the different system components. A summary of the various flywheel rotor manufacturing techniques is explained. The construction of the machine rotor and stator windings is explained with photos. The assembly of the entire system is briefly explained and shown.

4.8 References

[4.1] G. Genta, "Spin tests on medium energy density flywheels," *Composites*. Butterworth & Co (Publishers) Ltd, January 1982.

[4.2] D. Johnson, "Design considerations and implementation of an electromechanical battery system," Ph.D. dissertation, Dept. Electrical Engineering, University of Cape Town, 2008.

[4.3] F.J.M. Thoolem, "Development of an advanced high speed flywheel energy storage system," Ph.D. dissertation, Eindhoven university of technology, December 1993.

[4.4] Y. Bai, Q. Gao, H. Li, Y. Wu, M. Xuan, "Design of composite flywheel rotor," *Mech. Eng*. Vol. 3, no. 3, pp. 288–292, China 2008.

[4.5] A. C. Arvin, C. E. Bakis, "Optimal design of press-fitted filament wound composite flywheel rotors," *Elsevier Composite Structures,* vol. 72, pp.47–57, 2006.

[4.6] E.L. Danfelt, S.A. Hewes and T.W. Chou, "Optimization of composite flywheel design," *Int. J. Mech. Sci*. vol. 19, pp. 69-78, 1977.

[4.7] S.K. Ha, D.J Kim, T.H.Sung, "Optimum design of multi-ring composite flywheel rotor using a modified generalized plane strain assumption," *Elsevier, International Journal of Mechanical Sciences*, vol.43, pp.993-1007, 2001.

[4.8] S. Kitade, Comprehensive composite materials, vol. 6. Elsevier, 2000, Chapter 6 Flywheel, pp.571-580.

[4.9] Giancarlo Genta, "The shape factor of composite material filament-wound flywheels," *Composites*, April 1981.

[4.10] S-Y Fu, B. Lauke and Y-W Mai, *Science and Engineering of Short Fibre Reinforced Polymer Composites*, Woodhead, July 2009.

[4.11] J. Epaarachchi, H. Ku and K. GOHEL, "A Simplified Empirical Model for Prediction of Mechanical Properties of Random Short Fiber/Vinylester

Composites," *Journal of Composite Materials Online*, First published on August 26, 2009

[4.12] P.J.E. Forsyth, *Composite Materials*, London: Institution of Metallurgists, British Crown Copyright, Illiffe Books LTD, 1966.

[4.13] G. Genta, *Kinetic Energy Storage, Theory and Practice of Advanced Flywheel Systems,* Butterworth & Co. Ltd, 1985.

Chapter 5

Test Rig Design and Thermal Analysis of the Flywheel System

The previous chapters discuss the design and prototyping of the system components. This chapter describes the design of the test rig for evaluating the flywheel system and a thermal model of the flywheel energy storage system. The calculated losses are used to establish the temperature behaviour of the system using a lumped parameter circuit model. The flywheel system is encased in a vacuum hence only conduction and radiation are considered, however, convection is also discussed.

5.1 Design of Test Rig and Containment Structure

High-speed electromechanical flywheel components carry an inherent risk of failure due to design errors or manufacturing anomalies specifically in the flywheel rotor where different manufacturing techniques suffer from different failure criteria [5.1] [5.2]. Each high speed rotating component contains a large amount of kinetic energy and component failure presents a danger to surrounding equipment and personnel. Proper design and construction of the test rig and burst containment is essential.

Facilities capable of testing high-speed electromechanical flywheels of this nature are not available in South Africa. The facilities that come close are limited by speed, inertia and the required outputs. Commercial testing facilities are quite expensive and in most cases are built with generic instrumentation requiring hardware to suite specific needs. Testing of high-speed machinery requires special attention regarding safety and accuracy. This section focuses on the development of a test rig for high-speed electromechanical flywheels. The rig will be capable of testing various flywheel diameter sizes, different machine types and has a computer based control desk to drive the systems under different operating environments.

5.1.1 Need for a Flexible and Safe Test Rig

A flywheel system may fail for any of the following reasons; failure of the controllers, fluctuation in the vacuum increasing the losses leading to loss in material strength, fatigue, creep, failure of other parts, bearing, machine, dynamic stresses due to vibrations among others [5.3]. Containment structures are hence required to avoid any fragments from damaging equipment and harming personnel in the surrounding environment. Various options have been considered for the flywheel containment systems and these include steel structures, aluminium, fibre composites or a combination of any of the materials [5.4] [5.5]. Steel structures have been used as in [5.6] and these are designed based on Crushing Fragment Containment Analysis (CFCA). These structures are reliable but are known to increase the weight of the entire system. This is particularly disadvantageous for applications where the weight is significant. The reduction of the containment thickness to reduce the weight is dangerous hence the use of combination designs is more attractive. These light weight systems are more feasible for mobile applications and makes transportation of standalone systems easy during purchase and for repair.

In [5.7], a transient model was developed for a metal containment for a flywheel system designed with a rotor diameter of about one-third of the full-scale locomotive flywheel diameter. The tip speed of the subscale rotor is equal to that of the full-scale rotor with a

stored energy of 500 MJ. The major issues include the ability to withstand a rotor burst and the strength of the containment joints.

Existing commercial test rigs are expensive and not built to particular design specifications. In one of the test facilities visited, a special hub was required each time a flywheel was to be tested. This facility is limited to speeds up to 15,000 rpm for a 3 kg flywheel and the entire system needs to be tested in a vacuum.

The design specifications for the test rig takes into consideration; safety, flexibility, the operating environment, proper alignment, drive system and data acquisition. The burst containment is designed with a large safety margin to ensure the safety of personnel. The operating environment can constitute a vacuum or helium/air mixture together with controls and level gauge.

5.1.2 Design of the Burst Containment for the Test Rig

The containment must be able to contain any fragment from penetrating. The system should be able to limit forces, moments and vibrations transferred outside during the failure process and also avoid the emission of pollutant substances. The approaches presented in [5.6] [5.8] [5.9] are used to design the burst containment used in this rig. In this test rig, the containment design for isotropic materials is used. These materials burst into few particles with high translational forces as compared to orthotropic materials which exhibit higher rotational forces.

Consider a cylinder of thickness t, inner radius of Rci, with clearance of rotor c, with isotropic flywheel rotating at angular speed of ω. During failure, the rotor will disintegrate as shown in Fig. 5.1.

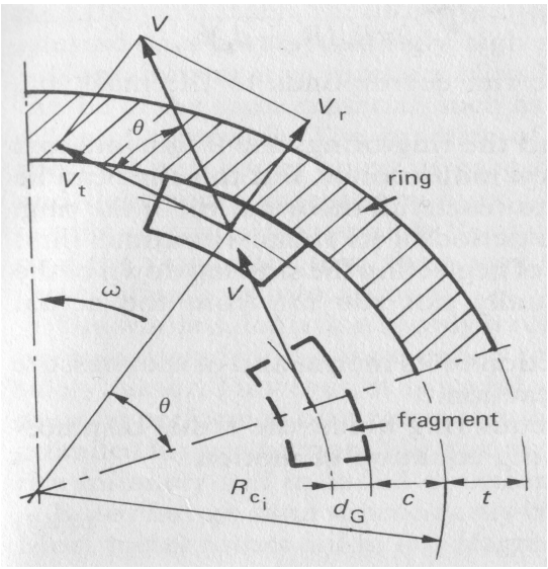

Figure 5.1: Failure of isotropic flywheel (Source: Genta)

The angle, θ the centre of mass the fragment displaces before it contacts the ring is given by:

$$\theta = ar\cos\left[1 - \frac{c}{\left(R_{C_1} - d_G\right)}\right] \tag{5.1}$$

Where d_G is the half-length of the fragment after rupture.

The radial velocity at instant of impact is given by

$$V_r = V\sin\theta = \omega(r_o - d_G)\sin\theta \tag{5.2}$$

Where V is the tip speed of the fragment.

On impact, total radial kinetic energy of the fragment becomes;

$$e_r = \frac{1}{2}m_r V_r^2 = \frac{1}{2}m_r\omega^2(r_o - d_G)^2\sin^2\theta \tag{5.3}$$

The energy dissipated during impact is given by

$$e_d = \frac{m_f m_c V_r^2}{2(m_f + m_c)} \tag{5.4}$$

This results into a centrifugal pressure given as;

$$P_c = \frac{m_f V^2 \cos^2\theta}{2\pi R_{C_1}(R_{C_1} - d_G)h} = \frac{m_f \omega^2 (r_o - d_G)^2 \cos^2\theta}{2\pi R_{C_1}(R_{C_1} - d_G)h} \tag{5.5}$$

Hence the radial kinetic energy and work done by the pressure is converted to elastic then plastic strain energy

$$\frac{1}{2}(m_f + m_c)V_1^2 < 2\pi R_r ht\left[\delta_u\left(\varepsilon_u - \frac{1}{2}\frac{\delta_u}{E}\right) - P_c\varepsilon_u\, r/t\right] \tag{5.6}$$

References [5.6] [5.8] give an empirical formula for calculating the minimum required ring thickness as in (5.7).

$$t = V\sin\theta\sqrt{\frac{m_f}{2lT}} \tag{5.7}$$

Where t is the containment thickness, V is the velocity of the particle, θ the centre of mass the fragment displaces before it contacts the ring, m_f is the mass of the fragment, and l is effective length

In [5.9], the containment thickness is investigated using the temperature of the containment after burst conditions. The total energy before fracture should be equal to the total energy after fracture. The mass of the containment, m_e is shown as in (5.8).

$$m_e = \frac{\pi H\rho(R_o^2 - R_i^2)}{2} \tag{5.8}$$

Where H is the height of the containment, ρ density of the material used and R_o and R_i are the outer and inner radius respectively.

The containment structure dimensions were calculated as in equation (5.7) however purchase of such structures with specific dimensions is very costly. This is because a solid rod is considered and bored through to get the required dimensions. The containment was manufactured from an old pipe and transformed as shown in Fig. 5.2.

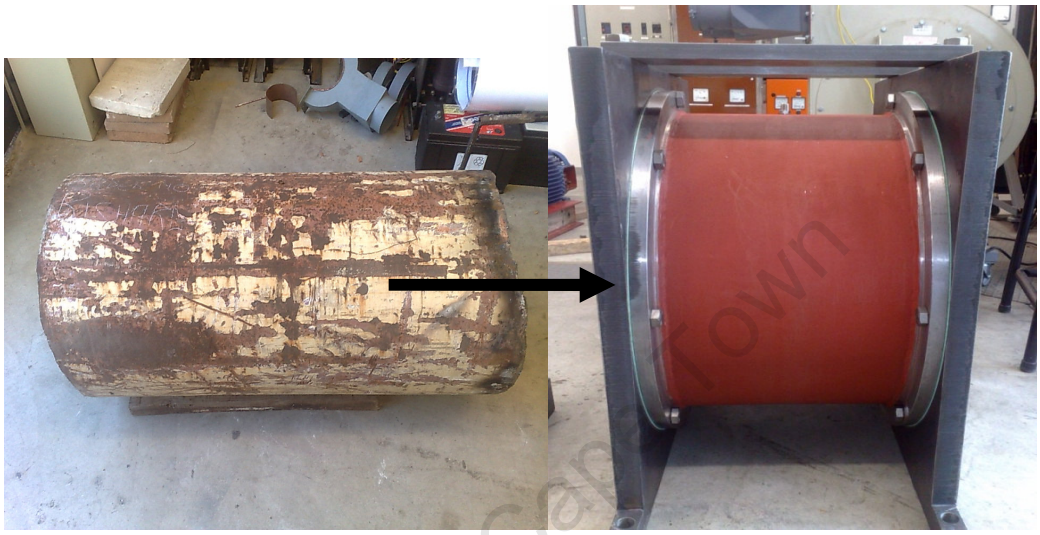

Figure 5.2: Transformation of old pipe to containment

The mechanical integrity of the old pipe was checked. Two flanges were fitted to hold the containment on the Tee plates. For increased safety, the containment was reinforced with a steel box.

5.1.3 Mechanical Specifications

For flexibility, the rig is built with flexible Tee plates and flat base plate. As shown in Fig. 5.3, the shaft length can be adjusted to correspond to the system specifications. A top plate is hinged onto the top plates to increase stiffness of the rig.

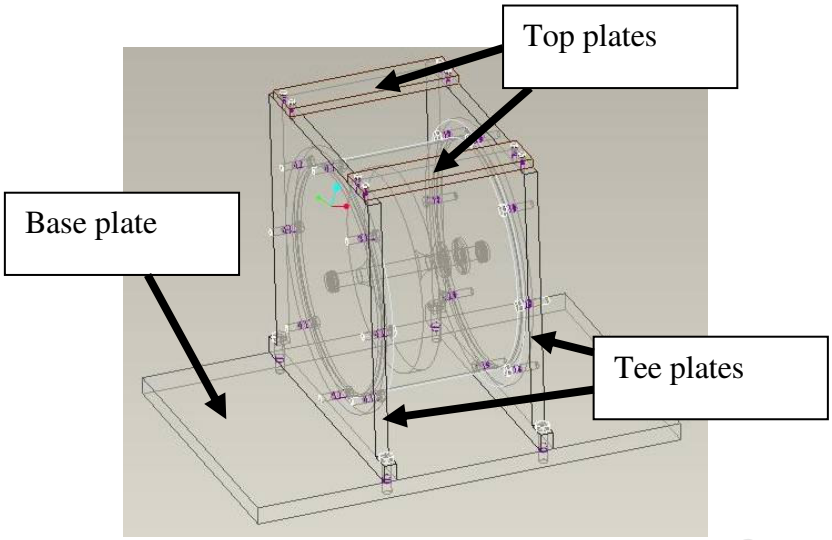

Figure 5.3: Test rig structure.

A machined base plate of 1,000mm by 700mm is used as a reference point. It's bolted onto a flat test bed. Tee plates are used to hold the rotating structure as this reduces the radial forces as compared to when the end plates are hinged onto the pipe. The first set of Tee plates are 200mm by 700mm with 50mm shoulders of 70mm thickness as shown in Fig. 5.4. They are held onto the base plate with M20 bolts. The second set of Tee plates are 660mm by 700mm with 50mm shoulders and 50mm thickness with shaft distance of 365mm.

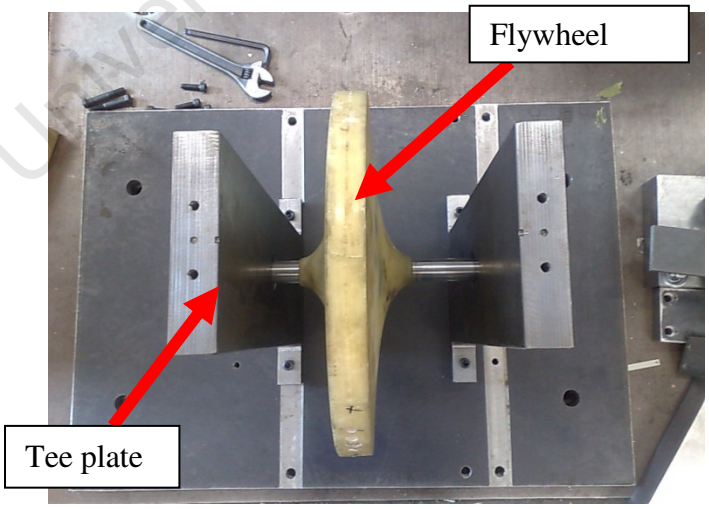

Figure 5.4: Tee and base plates as viewed from above.

The lower ends of the Tee plates are machined for improved alignment and the face plate was machined with a PCD of 660mm. M16 bolts are placed on the face plate for the containment and four M8 bolts were used to increase stiffness of the structure. The containment was fitted with 3mm rubber gasket to enhance the vacuum. A flange of 20mm by 40mm was used with M16 bolts to hold the containment as shown in Fig. 5.5.

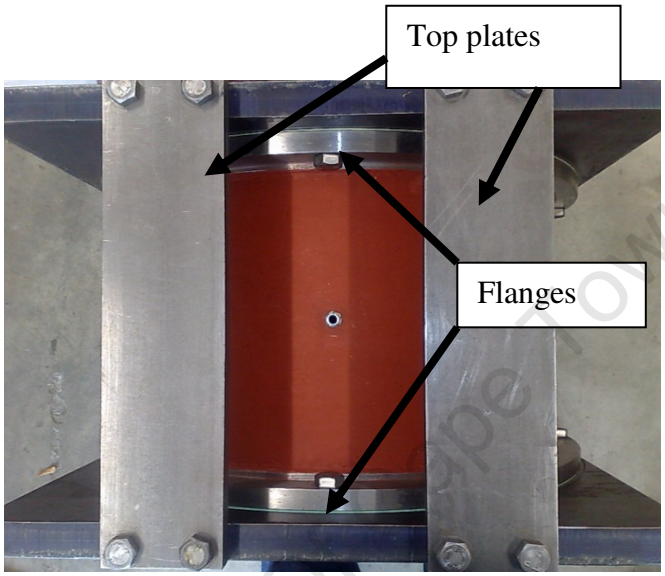

Figure 5.5: High speed test rig

The shaft length can be varied by using either of the two Tee plate sets. The sets provide for either 365mm shaft length or 275mm shaft length. This allows the rig to be used for flywheel system testing, flywheel rotor or testing of an electrical machine without flywheel rotor. The shorter shaft provides for a stiffer system. Other shaft dimensions can be considered with adjustments on the base plate.

5.1.4 Flywheel Rotor Testing Specifications

The inner diameter of the existing containment is 500 mm. This implies the maximum flywheel rotor can be up to 465 mm depending on the deformation expected on the system. Numerical analysis can be used to predict the expected deformation on the flywheel rotor. The containment size is sufficient for testing prototypes especially for high speed where the rotor diameter would generally be much smaller due to the ultimate

strength limit. Various configurations can be considered, that is the inside-out and conventional as shown in Fig. 5.6.

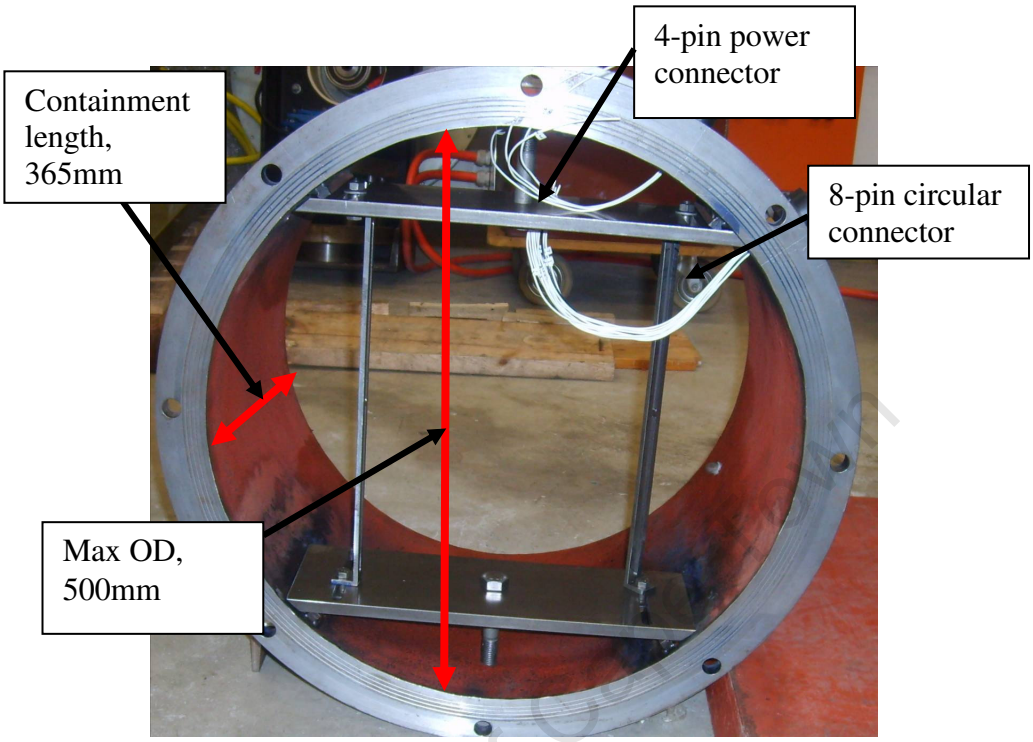

Figure 5.6: Containment structure limits with accessories.

Different flywheel rotors can be tested, that is, cast, laminated, filament wound etc. The shaft thickness can be varied depending on the bearings utilised. The existing bearing structure houses 47mm OD bearings with 25mm inner diameter. In this thesis, two flywheel rotors are considered, a cast rotor with profile one characteristics and laminated flywheel with profile two characteristics.

Other accessories include four and twelve pin circular connectors used for power and signals respectively. These connectors are special as they can be used in vacuum environments with the ability to contain 8 bar pressure levels. They are built with O-rings to prevent leakage in vacuum.

5.1.5 Electrical Machine Test Specifications

The test rig has two electrical machines rated at 100W and 500W. The system can be assembled in normal air pressure or reduced air pressure. The 100W machine has a voltage rating of 36V and can be used to test light weight rotor systems or validate friction coefficients of bearings and also test drive prototypes. The 500W machine has a voltage rating of 150V with stator wound from class H insulation and is able to withstand up to 200°C. This means the stator has the ability to over load due to its high temperature tolerance. The stator has an option of water cooling through silicon tubing placed in the hot spot and peripheral areas of the stator. This tubing has a temperature rating of 200°C which matches the stator windings. This further allows for increased current loading of the machine.

Structural analysis was performed on the electrical machine structure to ensure mechanical integrity. Some additions to improve integrity include a key way and grub screw, which act as secondary protection in case of a short circuit on the load side. The 500W electrical machine is shown in Fig. 5.7.

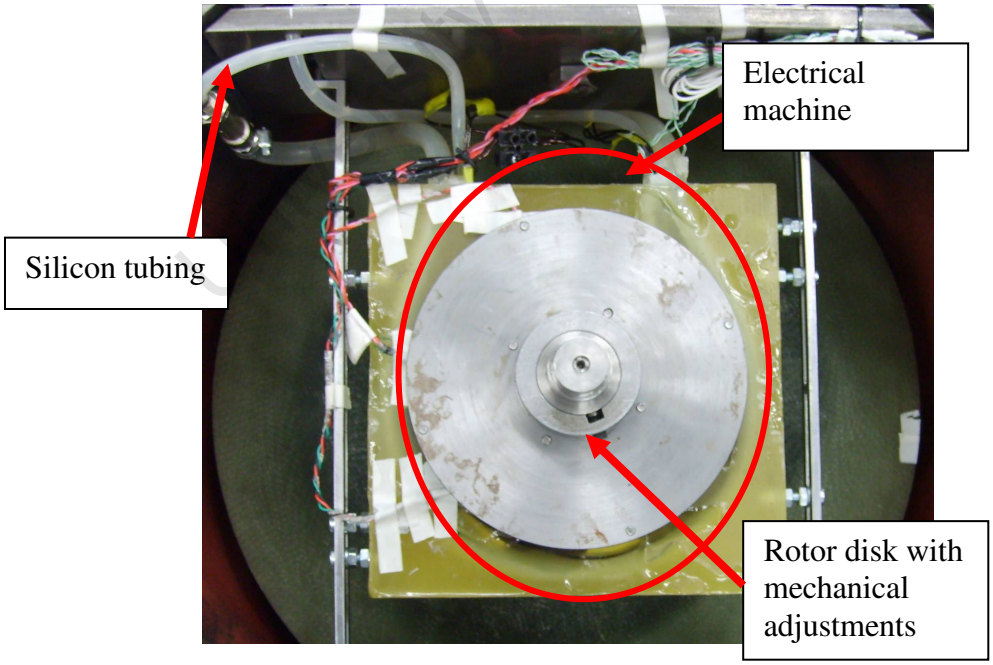

Figure 5.7: 500W electrical machine for flywheel testing.

From experimental verification, the 500W machine has accelerating torque of 0.758Nm at start up and this is measured through the run up time of the prototyped flywheel system.

This test rig also has the ability to test other high speed machine types. The current system is able to test AFPM machines up to an OD of 465mm. The bearing structure is restricted to 47mm OD however the shaft size is flexible. As shown in section 5.1.6, the test rig has hall sensors driven from a dSPACE control desk which can be programmed for any machine. The stator holding structure for any AFPM is available. For the case of machines with a radial configuration, a new stator holding structure needs to be built. The axial length of the test machine is dependent on whether it's tested with the flywheel rotor or not.

5.1.6 Drive System Specifications

The control system used is shown in Fig. 5.8. The system consists of power supply from the mains, 100A rectifier and a switch that is manually used to change from motor mode to generator mode in case a load is connected. Also included is an inverter driven by dSPACE PWM switching, data acquisition system which is performed by a power analyser, control desk (PC) and signals from the flywheel system. It's envisioned that a solar panel would act as the power source for a fully functional system and a DC-DC converter to regulate the voltage on the reference DC bus.

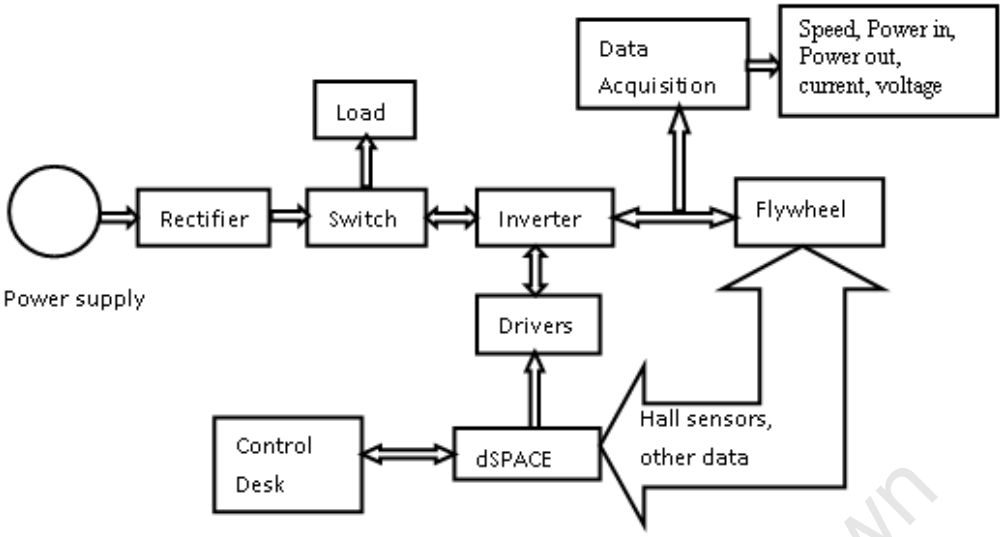

Figure 5.8: Schematic of Drive System

During motor mode, the mains supplies the system which ramps up in speed and in generator mode, the switch is changed, power supply is shut down and the load is supplied. This was done manually during the testing process. The current set up is able to test BLDC machines and this can be programmed to test any other type of machine. The full set up of the drive system is shown in Fig. 5.9 below.

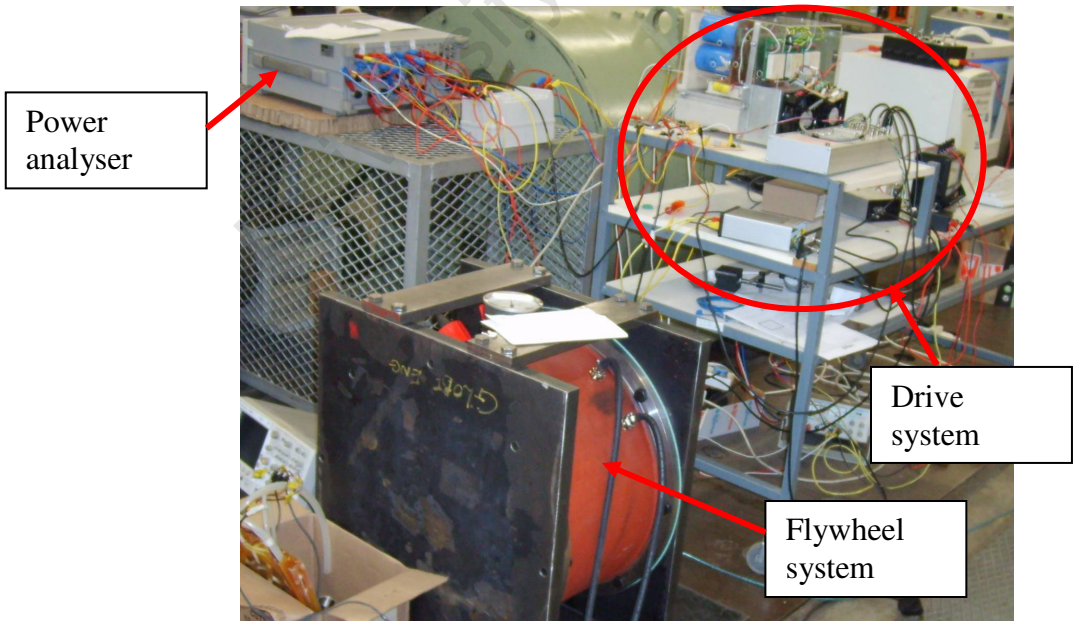

Figure 5.9: Overall flywheel system

5.1.7 Thermal, Bearing and Vacuum Specifications

The temperature acquisition is provided by eight probes available on a Pico logger system. The thermal parameters are essential in predicting failure, malfunction and performance of the system. Temperature prediction is also essential especially for vacuum enclosed systems where the major medium of heat transfer is radiation and conduction. This system is able to store up to a million seconds worth of data.

The bearing structure is limited to an outer diameter of 47mm, but the inner can be adjusted. Hybrid ceramic bearings and energy efficient bearings are currently being used in this test rig and are capable of reaching 40,000 rpm and 18,000 rpm respectively. The friction loss moments of these bearings are given and based on the rolling frictional moment, sliding frictional, from the seals and drag coefficient. This is essential in loss analysis of a new machine or a flywheel system to be tested. The friction moment for 6005 hybrid ceramic bearings with a radial force of 210N is given in table 5.1. The base oil viscosity is given as 15.8 at 80^{o}C.

Table 5.1: Frictional Components of the Bearings

Moment	Calculated value (Nm)
Rolling friction	0.0139
Sliding friction	0.0748×10^{-3}
Seal friction	3.7×10^{-3}
Drag friction	45.34×10^{-3}

This moment translates into a loss of 164W for the hybrid ceramic bearings and 82W for the energy efficient bearings of the same dimensions.

The vacuum has the capability of reaching up 1 mbar using a one stage single phase vacuum. The single stage rotary vane pump used has low sound levels of 50 dB, pumping speed of 10 m3 per hour, reaching an ultimate vacuum of 99.9 %. The performance of the vacuum is sensitive to leaks in the containment structure.

5.2 Modal Analysis of Test Rig

A modal analysis of the test rig was performed to ascertain the vibration characteristics, that is, the natural frequencies and mode shapes of the test rig when the flywheel rotates. In determining the vibration characteristics, suitable initial conditions are set causing the rig to vibrate at one of its natural frequencies and the shape of the vibration will be a scalar multiple of a mode shape.

The mode and Eigen values represent the natural frequency of a system and the eigenvector is the mode shape shown by displacements of the structure [5.10] and this is expressed as seen in equation (5.9)

$$[M]\{\ddot{u}\}+[C]\{\dot{u}\}+[K]\{u\}=\{F\} \tag{5.9}$$

Where M, C and K are mass, damping and stiffness matrices are constant with time respectively and F is the unknown nodal displacements varying with time. A continuous structure has an infinite number of degrees of freedom (DOF). The finite element method approximates the real structure with a finite number of DOFs. N mode shapes can be found for a FEM having N DOFs.

At a single degree of freedom

$$u=\phi\cos(\omega t) \tag{5.10}$$

u is the vector of nodal displacements and $\{\phi\}$ is the vector of amplitudes for each DOF.

For the entire structure the structural vibration is:

$$\{u\}=\{\phi\}\cos(\omega t) \tag{5.11}$$

$\{u\}$ is the displacement of a nodal DOF and ϕ is the amplitude

Considering a multi DOF system assuming the system is undamped and not excited by any external forces, then;

$$[M]\{\ddot{u}\}+[K]\{u\}=\{0\} \tag{5.12}$$

If system vibrates according to a particular mode shape and frequency as shown in equation

$$\{u\}=\{\phi\}_i \cos(\omega_i t) \tag{5.13}$$

Where $\{\phi\}_i$ is the i^{th} mode shape and ω_i is the i^{th} natural frequency.

The first and second derivatives are inserted into equation (5.12) resulting into equation (5.14).

$$(-[M]\omega_i^2+[K])\{\phi\}_i=\{0\} \tag{5.14}$$

Solving the equation gives

$$\{\phi\}_i=\{0\} \tag{5.15}$$

$$\det(-[M]\omega_i^2+[K])=0 \tag{5.16}$$

Hence the Eigen problem is solved giving the results as in (5.17-5.20).

$$[A]\{x\}=\lambda[I]\{x\} \tag{5.17}$$

$$(-[M]\omega_i^2+[K])\{\phi\}_i=\{0\} \tag{5.18}$$

$$[K]\{\phi\}=\omega_i^2[M]\{\phi\} \tag{5.19}$$

$$[M]^{-1}[K]\{\phi\}=\omega_i^2[I]\{\phi\} \tag{5.20}$$

Hence the natural frequencies are Eigen values ω_i^2 and the mode shapes are Eigen vectors $\{\phi\}$.

The mesh controls and solver algorithm are preselected by the ANSYS workbench and this is done automatically. The analysis was based on two varying initial conditions, the free vibration analysis and the other based on pre-stressed static structural analysis.

5.2.1 Free Vibration Analysis

In this free vibration analysis, only one constraint was applied on the base plate. The rest of the system was left to vibrate freely. The fifth mode had an impact on the rig as shown in Fig. 5.10 and 5.11. This happened at 266.2Hz which corresponds to 15,900 rpm.

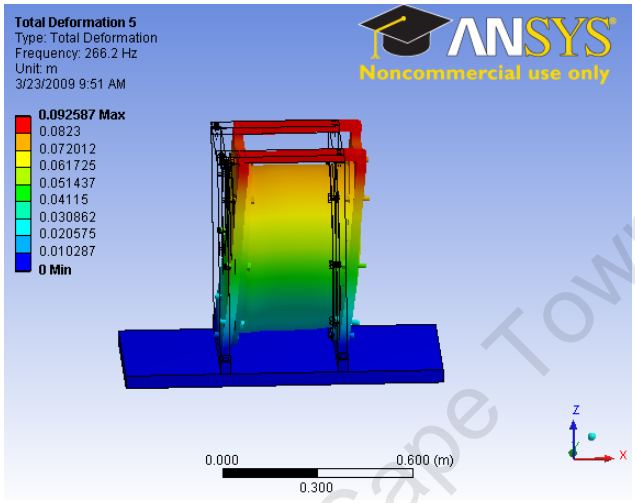

Figure 5.10: Fifth mode shape with displacement

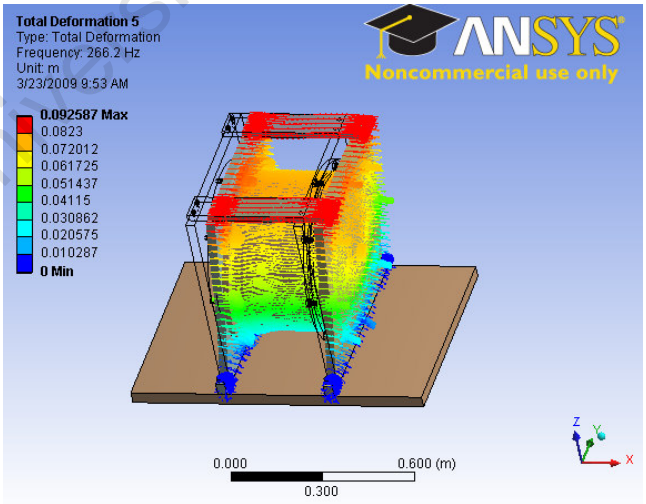

Figure 5.11: Fifth mode shape with direction of displacement

The forces on the rig represent lateral movement at the top of the test rig. This can be mitigated by reinforcing the top plates with hinges bolted onto the flat base. This would increase the stiffness of the entire structure.

5.2.2 Pre-Stressed Modal Analysis

In this analysis, the initial condition is set as the static structural analysis. A direct solver was considered and pre-stressed selected as input to the modal analysis. The fourth mode was found to be significant to the rig structure and this occurred at 336.12Hz as in Fig. 5.12, corresponding to approximately 20,000 rpm.

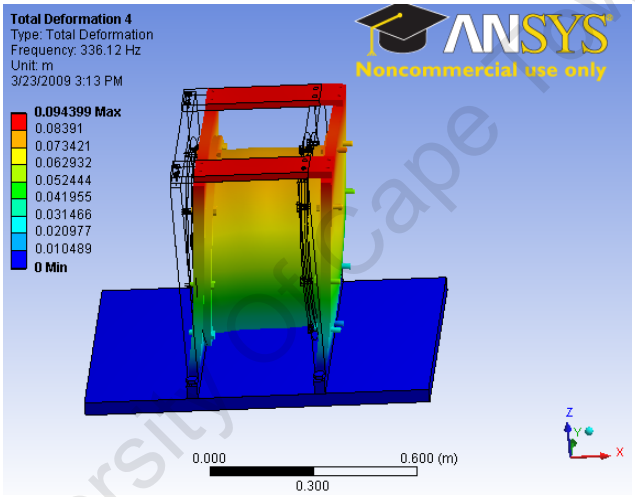

Figure 5.12: 4th Mode shape at 336.12Hz

The occurrence of the fourth mode shape can be increased by reinforcing the top plates to increase the stiffness and rigidity. Considering the rig was constructed for up to 40,000 rpm testing, further modes were extracted. The eighth mode shape was shown to form a deformation at approximately 40,000 rpm. The same solution as mentioned earlier would extend the mode occurrence further.

5.3 Thermal Analysis

An electromechanical flywheel system represents a very intricate thermal system and this can be attributed to the various components and different materials used in its construction [5.11]. The system consists of a machine, composite rotor, bearings and its environment which contribute to losses transforming into heat. The temperature tolerance of the materials used in the system, such as the glass fibre composite, permanent magnets, winding insulation and rotor disks, determine the safe operating limits of the system [5.12]. It is difficult to determine the thermal behaviour of the complete system due to many variable factors, which include unknown loss components and their distribution, and the three-dimensional complexity of the problem [5.13]. Therefore, prior knowledge of the temperature rises in various parts of the system especially for high speed operation is crucial. Investigating the thermal behaviour of the system ensures that appropriate cooling or heat conductivity path is designed to provide for an increased operating temperature range [5.13] [5.14].

The flywheel system is operated in a vacuum containment to eliminate the windage loss resulting from the large diameter of the flywheel rotor. The inextricable link between the heat accumulation in the containment and the windage losses from the flywheel rotor results into temperature rise during high speed operation. This heat can cause high thermal stresses in the rotor causing early failure [5.15]. The windage loss is a major loss factor from the flywheel rotor as it increases exponentially with angular speed.

In addition, the stator windings are covered in epoxy resin for increased structural integrity and robustness of the stator; however, epoxy is a poor conductivity of heat with average of 0.35 W/mK. The evacuation of the heat from the stator is vital in ensuring a long life of the system. The energy efficient bearings also produce a significant amount f heat and this needs to be accounted for. It is therefore essential to develop models that predict the thermal performance of the system in order to re-adjust designs, and put in place measures to curb the heat problem. For example, the selection of the bearings can be influenced by the results of an accurate model used. These aspects can be dealt with

before prototyping. Also, the model can be used in ascertaining the over load capability of the system. This study considers the lumped parameter thermal model.

5.3.1 Heat Sources

The flywheel system consists of various heat sources that are expressed as electrical and mechanical losses. The electrical losses can be categorised into copper, eddy current, magnet losses and were discussed in the chapter 3. The mechanical losses are frictional losses from the bearings, windage from the flywheel and machine.

5.3.1.1 Frictional Losses

The frictional losses due to the bearings are evaluated using a new approach [5.16] which considers all the sources of loss in the bearing. There are mainly four distinctive sources as expressed in equation (5.21).

$$M = M_r + M_{sl} + M_{se} + M_d \tag{5.21}$$

Where M is the total frictional moment, M_r is the rolling frictional moment, M_{sl} is the sliding frictional moment and M_d is the drag frictional moment in Nmm

The rolling frictional moment is calculated from the equation (5.22).

$$M_r = G_r(\nu n)^{0.6} \tag{5.22}$$

Where Gr is a variable depending on, bearing type, bearing mean diameter dm, radial load (Fr), axial load (Fa); n is the rotational speed (rpm) and v is the kinematic viscosity of the lubricant at the operating temperature (mm^2/s).

The sliding frictional moment is calculated from the equation (5.23).

$$M_{sl} = \mu_{sl} G_{sl} \tag{5.23}$$

Where G_{sl} is a variable that depends on the bearing type, bearing mean diameter, radial and axial load; μ_{sl} is the sliding friction coefficient

The frictional moment of seals on both sides can be estimated using the following empirical equation (5.24).

$$M_{se} = K_{S1} d_s{}^{\beta} + K_{S2} \tag{5.24}$$

Where K_{S1} is the constant depending on the bearing type, K_{S2} is the constant depending on the bearing and seal type, d_s is the seal counter diameter and β is the exponent depending on the bearing and seal type.

For one seal only, the friction generated is 0,5 M_{se}, however, for RSL seals for deep groove ball bearings with an outside diameter over 25 mm, the moment of friction is constant for either one or two seals.

The drag frictional moment as in equation (5.25).

$$M_d = V_M K_{ball} d_m{}^5 n^2 \tag{5.25}$$

Where K_{ball} is the bearing related constant, K_{roll} is the rolling bearing related constant; d_m is the bearing mean diameter.

The ball bearing related constant is defined as in equation (5.26).

$$K_{ball} = \left(i_{rw} K_Z \left(D + d\right)\right) / \left(D - d\right) 10^{-12} \tag{5.26}$$

and the roller bearing related constant is defined as in equation (5.27).

$$K_{roll} = \left(K_L K_Z \left(D + d\right)\right) / \left(D - d\right) 10^{-12} \tag{5.27}$$

Where i_{rw} is the number of ball rows, K_Z is the bearing type related geometry constant, K_L is the roller bearing type related geometry constant, d is the bearing bore diameter and D is the bearing outside diameter.

The total power loss was calculated using the equation (5.28).

$$N_R = 1.05 \times 10^{-4} Mn \tag{5.28}$$

Where M is the total moment of frictional in Nmm and n is the rotational speed.

For the case of the energy efficient bearings only 50% of the loss is considered and as shown in Fig. 5.13 below, the total losses would be 80W from the energy efficient bearings.

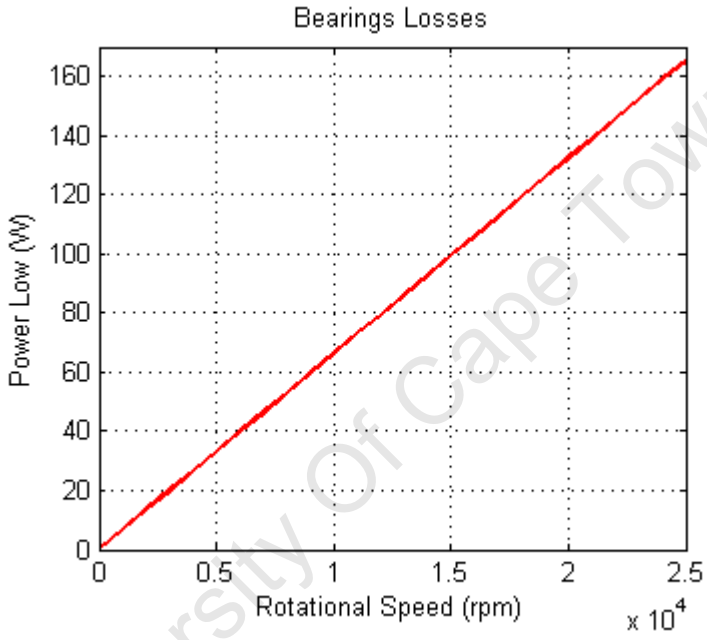

Figure 5.13: Hybrid bearing losses with speed

5.3.1.2 Flywheel Windage Loss

The flywheel windage losses are largely dependent on the angular speed, magnitude of the air pressure and the radius of the profile as well as the axial and radial gap clearance of the profile from the containment. Windage losses have been investigated as presented in [5.17] [5.18] where the use of a vacuum is suggested to reduce the air frictional losses and in [5.19] where a mixture of helium with air is used to reduce the windage losses.

Windage losses in the flywheel translate to:

- Reduced efficiency of the overall system.

- Power absorbed is converted into heat which increases the temperature of the rotor

In [5.17], the model was developed to predict windage loss in rotating electrical machines and an equation for a cylindrical rotor was developed and modified to suite the homopolar inductor alternator. This model will henceforth be considered as model one. The following assumptions were made;

- No axial flow exists
- The gap is small compared to the radius and length
- The fluid in the gap is homogeneous, and no pressure differential exists across the top
- The flow in the air gap is laminar

Hence the windage power loss is

$$W = \frac{2\pi\rho R^4 \omega^3 L}{R_e} \tag{5.29}$$

As Reynolds number increases, turbulence occurs hence relation between C_d and Re no longer exists.

$$\frac{1}{\sqrt{C_d}} = B + 1.768 In\left(R_e \sqrt{C_d}\right) \tag{5.30}$$

For the case of this study, new assumptions are described:

- The air gap over the whole flywheel is large as compared to the radius hence the pressure difference across the gap is significant.
- The flow of air is turbulent hence increased value of Reynolds number

In the model discussed in [5.18], the aerodynamic torque is given by

$$T = \rho\omega^2 R^5 C_m \tag{5.31}$$

Where C_m is non-dimensional coefficient and a function of Reynolds number R_e, Mach number M and Knudsen number K_n.

In the analysis made in this model, for a flywheel operating in atmospheric pressure conditions, the Knudsen number is very small and hence the gas surrounding it is said to be in continuous medium and for high values of Knudsen number, free molecule stream can be assumed.

High values of Knudsen number are chosen in this instance the containment has reduced air pressure. The solution for this is given in equation (5.32) and is considered the second model and henceforth called model two:

$$W = \frac{\rho \omega R^4}{\sqrt{\frac{2KT}{m}}} \tag{5.32}$$

Reynolds number is defined by $R_e = \frac{R^2\omega}{\upsilon} = \frac{\rho R^2 \omega}{\eta}$

Another model used for the estimation of windage loss is found in [5.19]. This model was used to accurately the predict windage loss for an ultimate shape flywheel system as in [5.2]. This model is considered as model three. The flywheel windage loss is given by

$$W = 2C_{df}\rho R^5 \omega^3 \tag{5.33}$$

A comparison of the three models gives varying results for reduced air pressure as shown in Fig. 5.14.

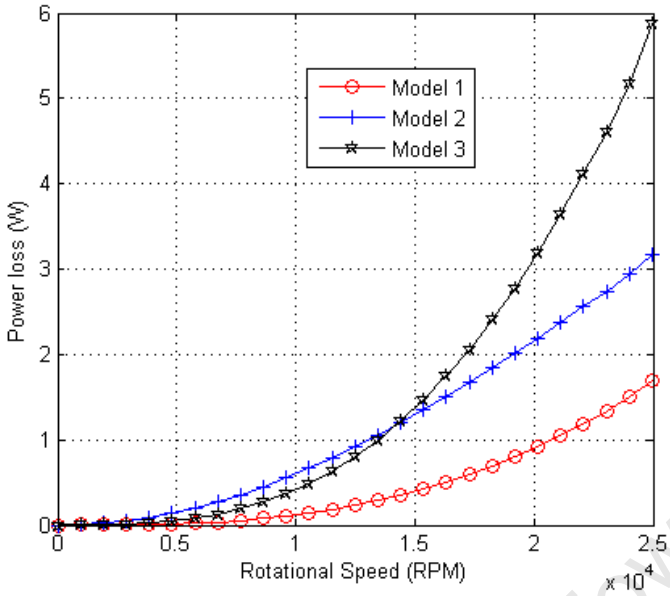

Figure 5.14: Windage loss model for the flywheel system

The selection of the required model is only possible with experimental verification. In this case, the windage loss is expected to be small. Considering the worst case scenario, model three is selected. This result is used in the loss prediction to study the thermal behaviour of the system during its operation. Different scenarios can be predicted based on the models mentioned.

5.3.1.3 Machine Windage Loss

The windage loss of machine is expressed as shown in equation (5.34).

$$P_{wind} = \frac{1}{2} C_f \rho (2\pi n)^3 \left(R_{out}^5 - R_{in}^5\right) \tag{5.34}$$

Where R_{out} is the outer radius, R_{in} is the inner radius, n is the speed of the rotor, C_f is the windage coefficient, ρ is the density of the medium through which the rotor rotates.

5.3.2 Heat Transfer

As mentioned, the thermal complexity of the system presents a unique and formidable difficulty. Heat is transferred or removed from the system by conduction, convection and radiation into the atmosphere.

There are three main methods of thermal modelling; exact analytical solution (distributed loss model), lumped parameter equivalent (concentrated loss model) and numerical analysis. The lumped-parameter thermal method is the most commonly used method to approximate the temperature behaviour in systems with internal losses [5.21]. Generally, the lumped-parameter thermal model is composed of thermal conduction resistances, thermal capacitances and power losses inside the system. Such a model is based on the hypothesis that the system, under the thermal point of view, can be divided into several parts that are connected to each other by means of thermal resistors and capacitors.

5.3.2.1 Conduction

In solids, heat is transferred from a high temperature region to low temperature region, taking into account the temperature gradient. The Fourier's law explains the heat transfer as shown.

$$Q = -\kappa A \frac{\partial T}{\partial x} \tag{5.35}$$

Where Q is the rate of heat conduction, A is the area of the flow path, k is the thermal conductivity and x is the length of the conduction path.

There are other laws that describe the steady-state conditions of heat conduction. The first law states that the energy is conserved and the second law states that the heat flux at any point in an isotropic region is proportional to the temperature gradient at the point. The two laws result into poison's equation given by equation (5.36).

$$\nabla^2 T = -\frac{\omega}{\kappa} \tag{5.36}$$

Equation (5.36) has similarity to electrostatic solutions and can be used to solve thermal conduction problems.

5.3.2.2 Radiation

In radiation, heat transfer transpires using electromagnetic waves. The transfer of radiant energy between surfaces is proportional to absolute temperature, emissivity and the geometry of each surface. Consider two surfaces at different temperatures T_1 and T_2 with surfaces areas A_1 and A_2 respectively. The transfer of heat is described by equation (5.37).

$$Q = \left[\frac{\sigma\left(T_1^4 - T_2^4\right)}{\frac{1-\varepsilon_1}{\varepsilon_1 A_1} + \frac{1}{A_1 F_{12}} + \frac{1-\varepsilon_2}{\varepsilon_2 A_2}} \right] \tag{5.37}$$

Where σ is the Stephan Boltzmann constant, ε denotes the emissivity of each surface, F_{12} is the view factor which is the orientation of the two surfaces and Q is the heat transfer.

5.3.2.3 Convection

Heat transfer occurs in fluids and can happen from surface to fluid. This is by either natural or forced convection. With natural convection, no artificial means of cooling are considered and the process of heat dissipation is governed by Newton's law of cooling as shown below.

$$Q = hA\left(T_1 - T_2\right) \tag{5.38}$$

Where *h* is the convection heat transfer coefficient.

The main difficulty with this equation is the calculation of the heat transfer coefficient, which depends on many variables such as the temperature differences between the heated body and air, the geometry and properties of the surface. In addition, the complex construction of the flywheel system makes the calculation of the values even more complex.

A fan or a pump can be used in forced while in natural convection, buoyancy forces induced by density gradients cause the fluid to flow across a solid surface. The heat transfer coefficient is dependent on; Reynolds number, Nusselts number and Prandtl number. Reynolds number describes the characteristics of the velocity boundary layer, that is, laminar, transition, turbulent. Nusselts number provides the measure of the convective heat transfer at the surface. Prandtl number is the ratio of the rate at which momentum is transported to the rate at which thermal energy is transported in the laminar boundary layer. This number is an indication of relative rates of growth of the velocity and thermal boundary layers.

Heat transfer coefficient between the rotor discs

For Reynolds number,

Laminar flow $\text{Re} \leq 2300$

Transition $2300 < \text{Re} < 10{,}000$

Turbulent $\text{Re} \geq 10{,}000$

It's assumed the flow is turbulent with natural convection

$$\text{Re} = \frac{U_m D}{\nu} \tag{5.39}$$

$$h = \frac{k}{R} N_u \tag{5.40}$$

Where $N_u = 0.015 R_e^{4/5} - 100\left(\frac{r_c}{R}\right)^2$ and $r_c = \left(2.5\times10^5 \nu/\Omega\right)^{1/2}$

Heat transfer coefficient around flywheel is similar to equation (5.40) where the Nusselts number is given as in equation (5.41).

$$N_u = 0.023 R_e^{4/5} P_r^{\,n} \tag{5.41}$$

Where n is 0.4 for heated fluid, $0.7<Pr<160$ and Re>10,000. It's noted that for gases, Prandtl is approximately zero [5.20].

5.3.3 Thermal Equivalent Circuit

The thermal equivalent circuit is an analogy of the electrical circuit where the heat is represented by a current source and the temperature by a voltage. All thermal resistances and capacitances are represented as resistors and capacitors respectively. The elements in the system are described by nodes. The nodes are hence used to develop a thermal equivalent circuit with respect to the system.

In the lumped parameter approach, the system is divided into various lumped components which are meshed to other components through a series of thermal resistors. The lumped parameters are derived from geometry information, the thermal properties of the materials used in the design, and constant heat transfer coefficients. The thermal circuit in steady-state condition consists of thermal resistances and heat sources connected between the component nodes. For transient analysis, the heat thermal capacitances are used additionally to take into account the change in the internal energy of the body with the time. In the simulation, the

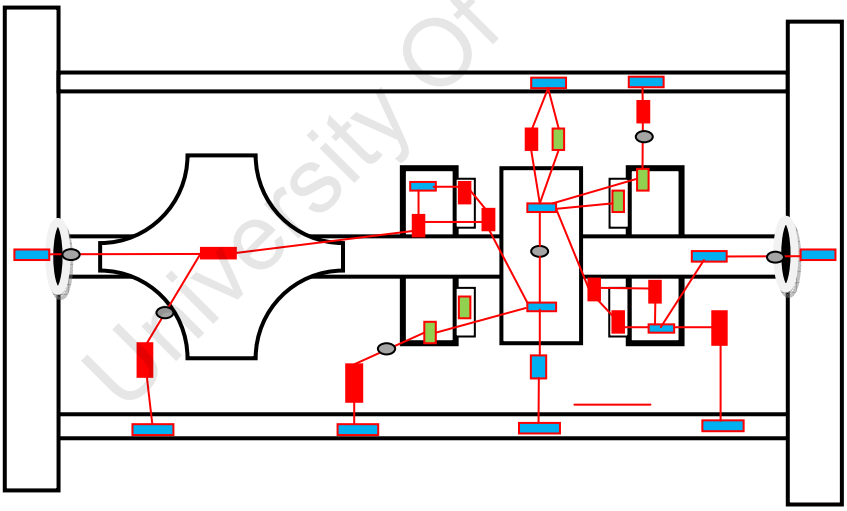

Figure 5.15: Cross section of the flywheel system with loss sources and resistors

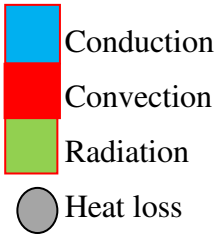

5.3.4 Thermal Parameters

Accurately estimating the corresponding resistances and capacitances of the different nodes is a very complex process. The geometry must be well established and to ensure good results, a major assumption that the heat flows in the radial and axial directions are independent is made. Other assumptions are; Capacity and heat generation are uniformly distributed and no circumferential heat flow.

The thermal capacitances and conduction resistance is calculated as shown in equations (5.42) and (5.43).

$$C = \rho V c \tag{5.42}$$

Where c is the heat capacity of the material, V is the volume of the material and ρ is the density.

$$R = \left(\frac{l}{kA} \right) \tag{5.43}$$

Where k is the thermal conductivity of the material, l is the length and A is the cross sectional area.

The more complex parameters is the thermal convection resistances as this depends on the angular speed, air nature of the flow, turbulent or laminar as well as distance of the flywheel and containment among others. The thermal resistance is given by equation (5.44).

$$R = \frac{1}{(\alpha A)} \tag{5.44}$$

Where A is the surface area of the convective heat transfer between areas and α is the heat transfer coefficient.

For radiation, the thermal radiation resistance is given by equation (5.45).

$$R_r = \frac{\frac{1-\varepsilon_1}{\varepsilon_1 A_1} + \frac{1}{A_1 F_{12}} + \frac{1-\varepsilon_2}{\varepsilon_2 A_2}}{\sigma\left[(\theta_1 + 273) + (\theta_2 + 273)\right]\left[(\theta_1 + 273)^2 + (\theta_2 + 273)^2\right]} \tag{5.45}$$

Where ε is the emissivity of the material, F_{12} is the view factor and A is the respective emitting surface.

There are two unknowns in equation (5.45) and hence to ascertain the values of the thermal radiation resistance, an iterative process is performed. The material properties used in calculating the thermal parameters are given in table 5.1.

Table 5.2: Material properties

Material	**Density(kg/m^3)**	**Thermal conductivity (W/mC)**	**Emissivity**
Copper	8946	398	0.87
Epoxy resin	1400	0.35	0.88-0.94
Mild steel	7846	54	0.17-0.32
Aluminium	2700	250	0.02-0.19
Stainless steel	8000	16	0.28-0.66

The parameters are calculated for vacuum operation with temperature correction.

Table 5.3: Thermal parameters

Parameter	Representation	Resistance
Rce1	Conduction Face epoxy	0.175
Rra1	Radiation from stator to environment	0.220
Rcc1	Conduction through containment	0.035
Rrm1	Radiation from stator to magnets	0.004
Rrd1	Radiation from stator to rotor disk	0.003
Rcb1	Conduction through stator brazing	0.028
Rcb2	Conduction through stator brazing 2	9.950
Rcr1	Conduction through rotor disks	0.002
Rcs1	Conduction through shaft	0.106
Rct2	Conduction through Tee plate	0.001
Ce1	Epoxy	92
Cf2	Bearings	47.6
Ce2	Copper	63
Cf1	Stray	48

The lumped parameter mode considered is based on the axial flux machine model a heat flow path within the flywheel system. The heat transfer due to convection was neglected as the system was operated under reduced air pressure. The bearings losses together with stray losses are considered in the simulation.

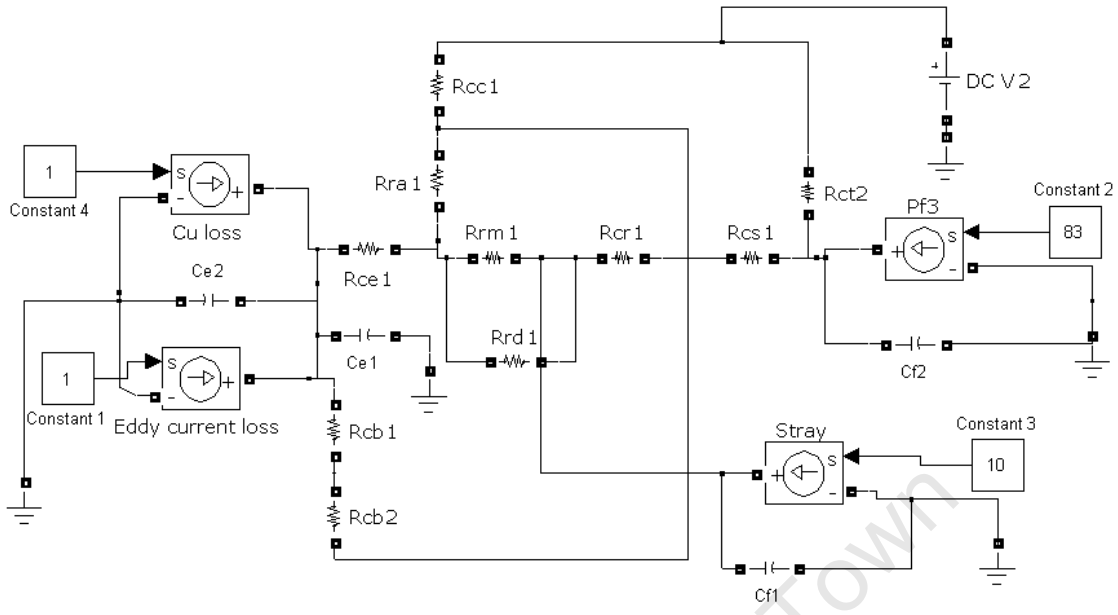

Figure 5.16: Lumped parameter model of flywheel system

5.3.5 Simulation Results

The model was used to carry out various analysis and considerations. For these simulations, the ambient temperature is taken as 30^{o}C. The system was simulated for various speeds and air pressure to obtain the transient and steady-state temperatures in the stator, rotor disk, and permanent magnets among others. For this application, the high speed operation is vital. Fig.5.17 shows the temperature rise of vacuum, rotor disk and stator temp at reduced air pressure.

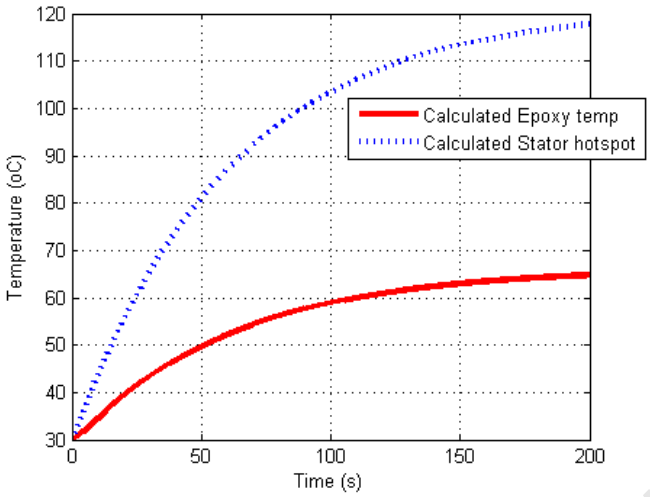

Figure 5.17: Temperature rise at rated current.

In the simulations the maximum temperature limit is not reached in transient state ambient and water temperatures are taken 30◦C and 20◦C respectively. The same analysis is repeated for the case where the system is running under different load conditions. The results are shown in Fig.5.18. In comparison to the previous case, the steady-state temperatures are relatively low due to low current.

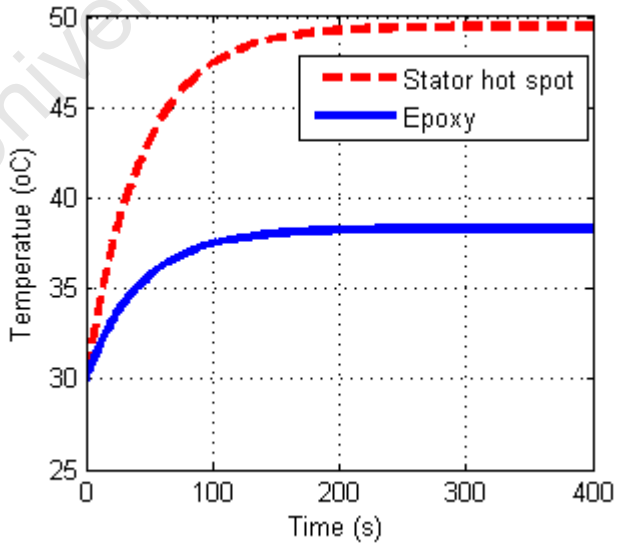

Figure 5.18: Temperature rise at low load condition

The thermal conditions in the case of an overloaded machine are also investigated. Fig.5.19 shows the temperature curves at reduced air pressure conditions.

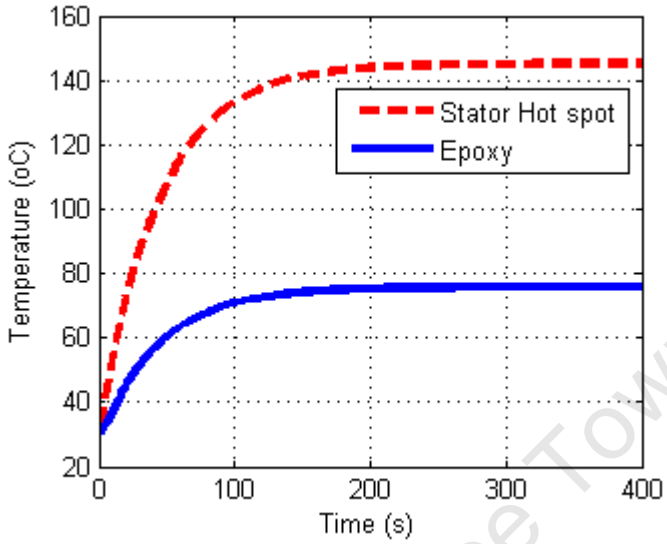

Figure 5.19: Temperature rise at overload condition

From Fig. 5.19, it's clear that cooling is required to for overloading capability of the system for proper operation.

5.4 Concluding remarks

This chapter summarized the development of thermal models using lumped parameter for the flywheel energy storage system. The thermal parameters are calculated based on the material properties and dimensions of the flywheel system. The results presented show temperature rise at vital operating points. In chapter 6, the measured temperatures are compared to simulation results.

5.5 References

[5.1] G. Genta, "Spin tests on medium energy density flywheels," *Composites*. Butterworth & Co (Publishers) Ltd, January 1982.

[5.2] D. Johnson, "Design considerations and implementation of an electromechanical battery system," Ph.D. dissertation, Dept. Electrical Engineering, University of Cape Town, 2008.

[5.3] F.J.M. Thoolem, "Development of an advanced high speed flywheel energy storage system," Ph.D. dissertation, Eindhoven university of technology, December 1993.

[5.4] Y. BAI, Q. Gao, H. Li, Y. Wu, M. Xuan, "Design of composite flywheel rotor," *Mech. Eng*. Vol. 3, no. 3, pp. 288–292, China 2008.

[5.5] A. C. Arvin, C. E. Bakis, "Optimal design of press-fitted filament wound composite flywheel rotors," *Elsevier Composite Structures,* vol. 72, pp.47–57, 2006.

[5.6] E.L. Danfelt, S.A. Hewes and T.W. Chou, "Optimization of composite flywheel design," *Int. J. Mech. Sci*. vol. 19, pp. 69-78, 1977.

[5.7] S.K. Ha, D.J Kim, T.H.Sung, "Optimum design of multi-ring composite #ywheel rotor using a modi"ed generalized plane strain assumption," *Elsevier, International Journal of Mechanical Sciences*, vol.43, pp.993-1007, 2001.

[5.8] S. Kitade, Comprehensive composite materials, vol. 6. *Elsevier*, 2000, Chapter 6 Flywheel, pp.571-580.

[5.9] Giancarlo Genta, "The shape factor of composite material filament-wound flywheels," *Composites*, April 1981.

[5.10] ANSYS, Inc *Theory Reference*, ANSYS Release 9.0.002114. SAS IP Inc

[5.11] C. Huynh, L. Zheng and P. Mc Mullen, "Thermal performance evaluation of a high speed flywheel energy storage system," *presented at the 33rd Annual Conference of the IEEE Industrial Electronics Society (IECON),* Taipei, Taiwan, Nov. 5-8, 2007.

[5.12] O. Aglén, Å. Andersson, Thermal analysis of a high-speed generator, *IEEE*, 2003

[5.13] F. Sahin, "Design and development of a high-speed axial-flux permanent-magnet machine," Ph.D dissertation, Technische Universiteit Eindhoven, 2001.

[5.14] J. Saari, "Thermal analysis of high speed induction machine," Ph.D dissertation, Helsinki University of Technology, Espoo, Finland, 1998.

[5.15] E.L. Danfelt, S.A. Hewes and T.W. Chou, "Optimization of composite flywheel design," *Int. J. Mech. Sci*. vol. 19, pp. 69-78, 1977.

[5.16] www.skf.com last checked 27th November 2009

[5.17] J.E. Vrancik, "Prediction of windage loss in alternators," NASA technical note D-4849, 1968.

[5.18] G. Genta. *Kinetic Energy Storage, Theory and Practice of Advanced Flywheel Systems*, Butterworth & Co. Ltd, 1985.

[5.19] Y.Suzuki, A. Koyanagi, M. Kobayashi, R.Shimada, "Novel applications of the flywheel energy storage system," *Energy*, vol. 30, pp. 2128-2143, 2005.

[5.20] Kirk D. Hagen, *Heat Transfer with Applications*, 1st ed., Pearson Education, June1998

Chapter 6

Experimental Results

This chapter discusses the experimental results of the flywheel testing. Two flywheel set ups are considered with 100W and 500W machine. The analysis includes isolation of the losses, efficiency, run down and thermal results.

6.1 Results of Flywheel System with 100 W machine

The first test of the flywheel system consisted of a cast flywheel rotor, hybrid deep groove bearings, with the 100W machine. The system was set up as shown in Fig. 6.1. The test was conducted to examine the overall performance of the system whereby the flywheel rotor and machine are coupled on the same shaft and tested under normal pressure.

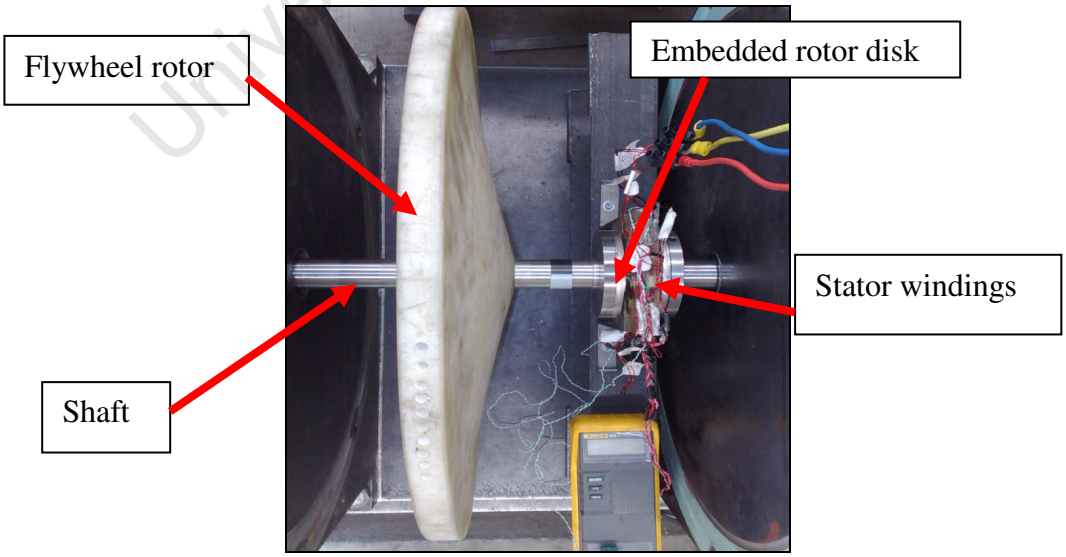

Figure 6.1: Experimental set up of flywheel system

The cast flywheel rotor named profile one was considered in this case as it exhibited lower weight compared to the others. This was attributed to the manufacturing and gentle exponential curve it exhibits. The shaft consisted of fixed hinges (shoulders) to afford the rotor disks from crushing onto the stator windings. This resulted in a fixed airgap of the electrical machine. In addition, one of the rotor disks was fixed through the flywheel side. This meant for every assembly process, the flywheel had to be removed first before the rotor disk making the system inflexible. The press-fitting of the flywheel rotor made the process even more cumbersome.

The grub screw used to hold the rotor disks in place were placed on the outer face of the disk. This resulted in an imbalance during the low speed operation. In Fig. 6.1, it can be seen that the test system exhibits a low energy to weight ratio. The system was ramped up at rated current and overload as explained in sections below.

6.1.1 Rated Current at 10A

Rated current was supplied to the system. Fig. 6.2 shows the speed response at start up, whereby the flywheel reaches a maximum speed of 320 rpm. The flywheel was unable to reach high speed operation and this was attributed to the low developed torque in the system.

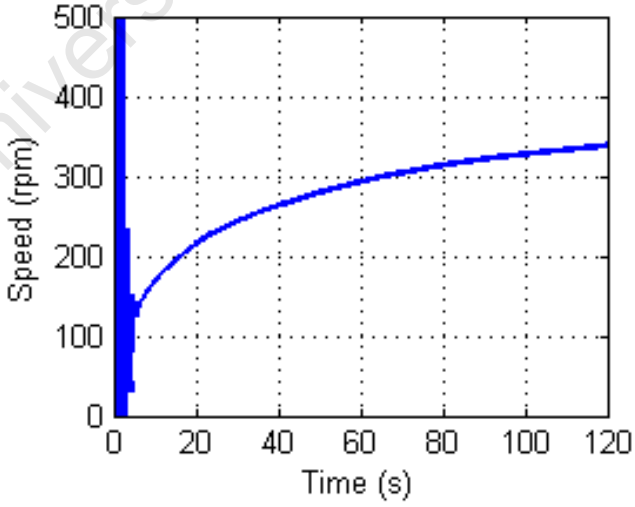

Figure 6.2: Speed response at rate power

The line current response of the system at rated power is given in Fig. 6.3, whereby BLDC mode of operation is evident by the square waveforms with a conduction angle of 120^{o}.

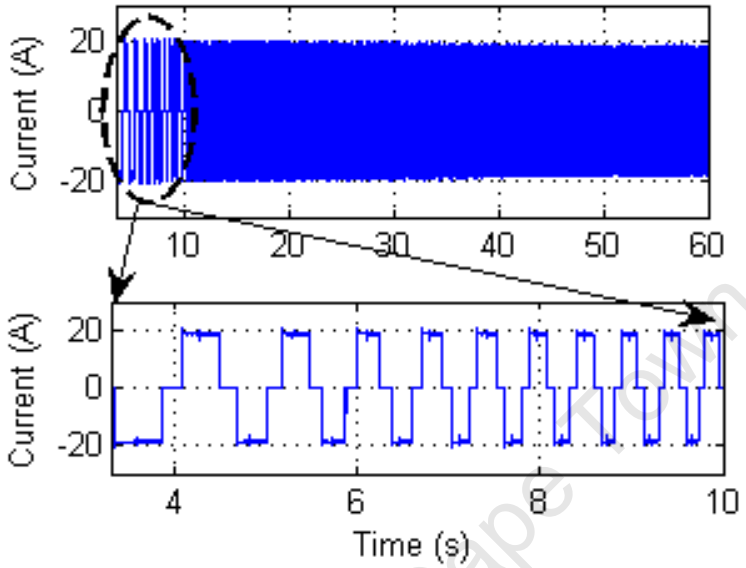

Figure 6.3: Line current response at rated power

The high losses resulting from the system were from the bearing structure which shows evidence of very high stiffness. The electrical machine was rated at low power yet the losses increased exponentially with speed. This meant the machine was unable to accelerate to the required speed.

6.1.2 Over-Load at 30A

To overcome the high frictional losses in the bearing structure, the system was supplied with 30A while monitoring the stator winding temperature. The system accelerated quickly to 1,000 rpm as shown in Fig. 6.4; however the flywheel was disconnected from the supply due to high temperature rise. The stator windings used in this case were of class F.

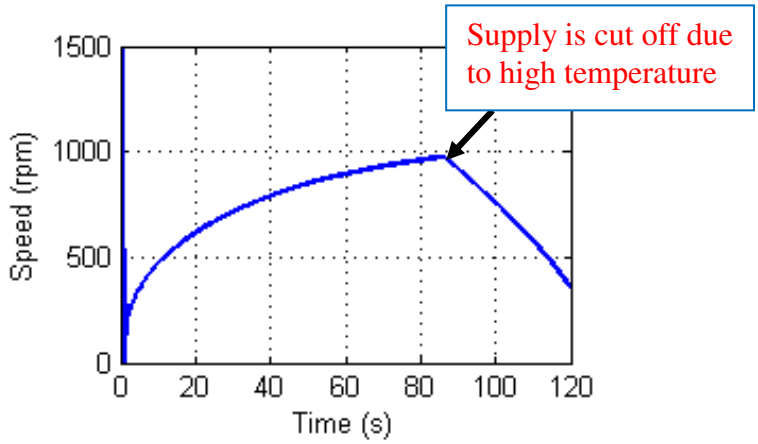

Figure 6.4: Speed response at 30A

The line current response of the system at 30A is given in Fig. 6.5. It was evident that a high current, the operation was still exhibiting square waveforms with a conduction angle of 120^{o}. The start up transients drop as the system ramps to speed.

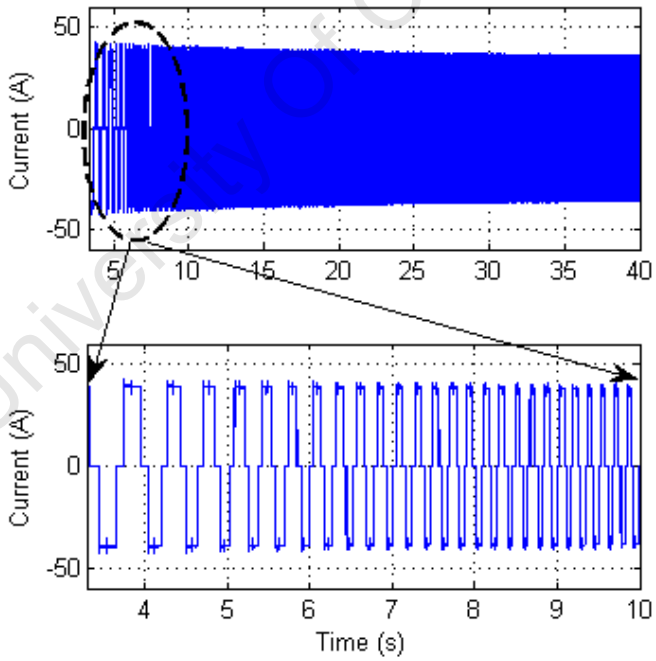

Figure 6.5: Line current response at 30A

The results from the first test set up showed that the machine was relatively small and inadequate to produce enough torque to accelerate to the designed speed. This together with the high friction bearings and large airgap made it even more complex.

In fact, there are numerous possible contributors to the unaccounted power loss in the system. The misalignment in the test rig would add to the frictional losses. Furthermore, these tests were not performed in the vacuum sealed containment; therefore the windage losses would be considerably higher as the system ramped up to speed. Since the motor is only rated at 100W, any of these factors could attribute to the results shown above. All the above issues were considered in the 500W machine. The efficiency and losses at the low speeds were not measured due to the low speeds achieved.

6.2 Results of Flywheel System with Modifications

As mentioned in section 6.3, the first flywheel set up exhibited low developed torque, high temperature rise, low power and had a fixed air gap. The new machine was designed and prototyped with other accessories to ensure elimination of the problems encountered earlier as shown in Fig. 6.6.

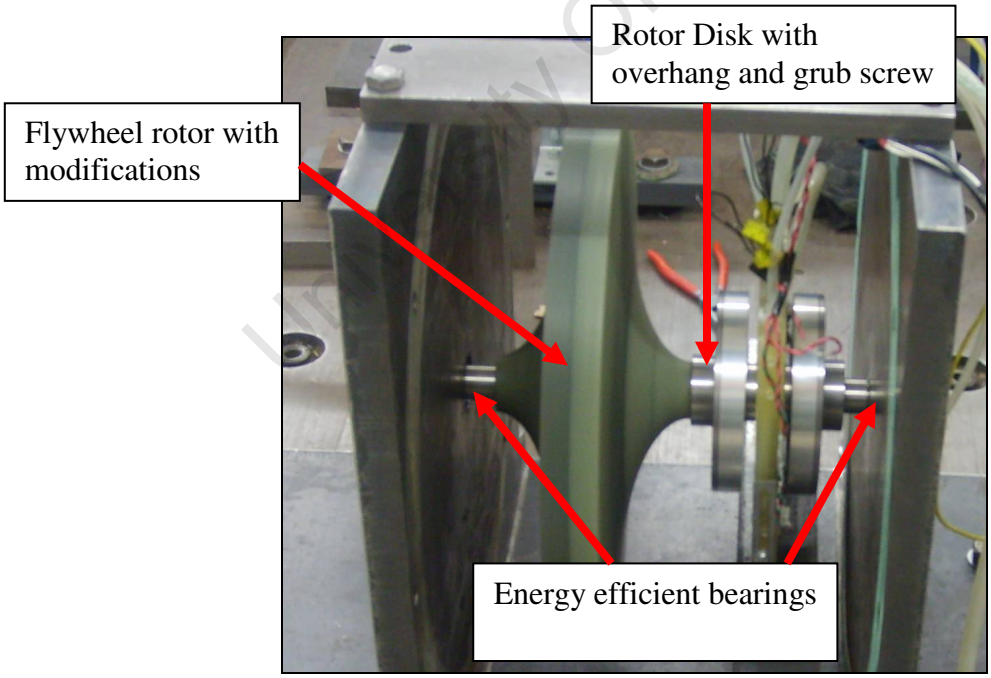

Figure 6.6: Flywheel system with modifications

For this test, the layered flywheel rotor exhibiting profile two with modification was considered. This meant more energy could be stored for any increased rotational speed achieved. New energy efficient bearings were considered and these bearings reduce the losses by 50% with a 95% saving.

To eliminate the fixed air gap problem, spacers between the rotor disks were considered to vary the airgap. This meant better air gap sizing and flexibility. In addition, the rotor disks were manufactured with an overhang and grub screw to hold the disks in place. This ensured easier assembly of the electrical machine and flywheel rotor, making it more flexible.

The 500W machine was considered for this test. The details of the prototype are given in chapter 4. The use of the 500W machine meant increased cost of the system. However, the construction and assembly was made much easier. The system was assembled in a containment structure and air pressure reduced to eliminate the windage loss resulting from the air friction as shown in Fig. 6.7.

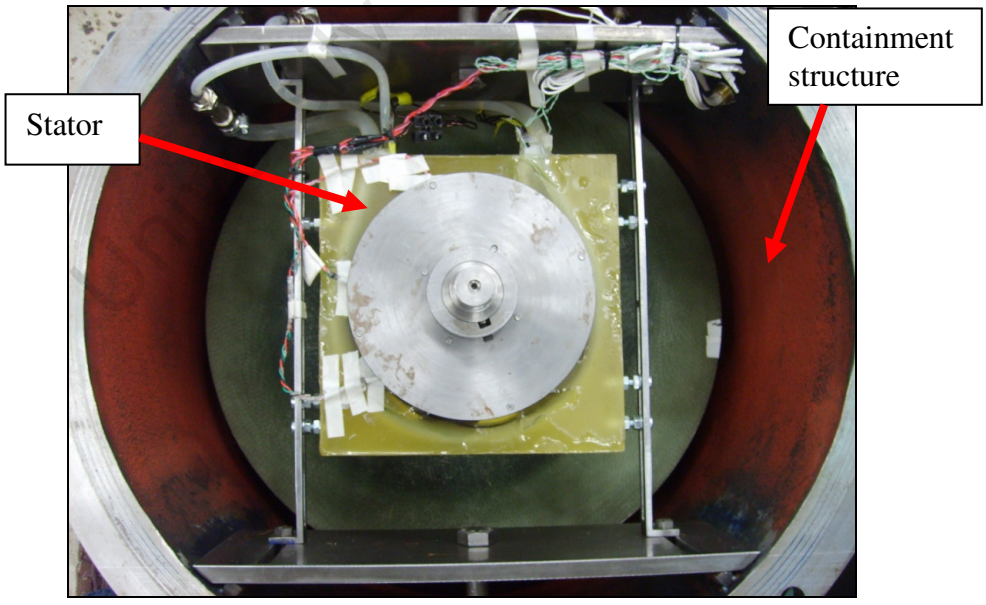

Figure 6.7: Assembled flywheel system

The flywheel system was ramped up to 6,000 rpm. Vibrations were observed and the testing was stopped at this stage due to safety concerns.

6.2.1 Rundown Curve

The system was accelerated to maximum speed of 6,000 rpm at reduced air pressure. Fig 6.8 shows the accelerating and run down curves. From the run down curve, the idling losses (mechanical losses at no load) are extracted. During operation at normal air pressure, the losses include, windage, frictional and stray losses. For reduced air pressure, the losses include frictional and stray losses. The windage losses are considered negligible at reduced air pressure.

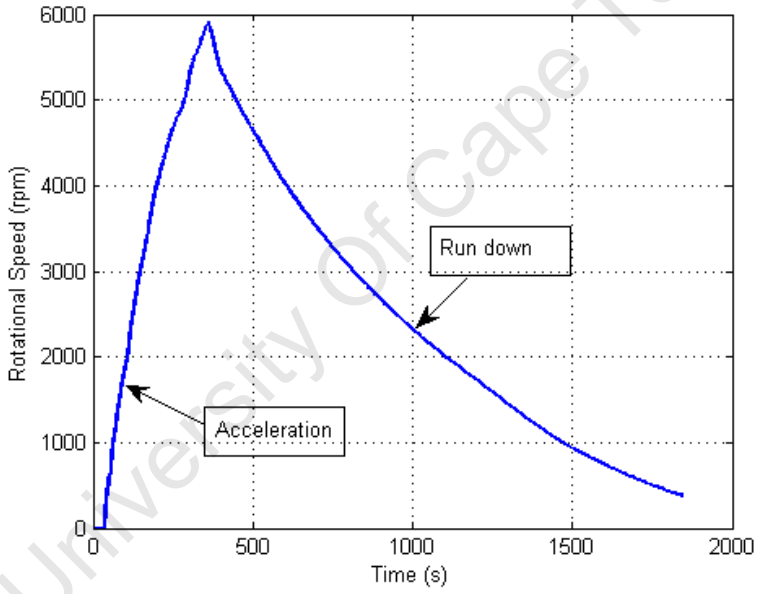

Figure 6.8: The acceleration and run down curve of the flywheel system.

Fig.6.9 shows the measured and calculated losses. The measured loss shows an exponential profile, which signifies the existence of windage loss. This is attributed to the pressure leakages existing in the test rig.

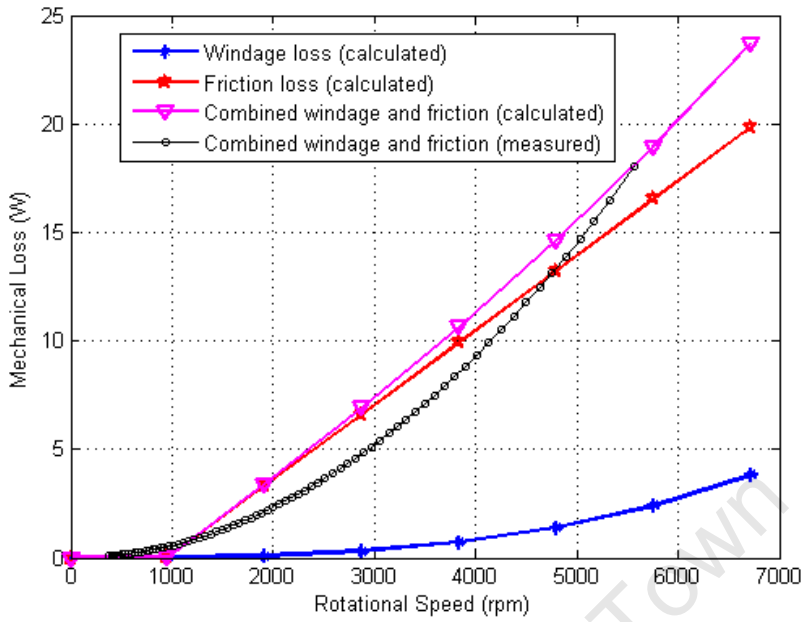

Figure 6.9: Measured and calculated mechanical losses.

The vacuum pump used was not able to hold the vacuum consistently. In addition, due to leaks in the containment structure, perfect vacuum was not achieved. The leaks result from numerous connections required for the hall sensors, thermocouples, power cables and stator brazing.

6.2.2 Flywheel System Efficiency

The charging efficiency during motor mode of operation and the total efficiency for a resistive load test were measured and shown in Fig. 6.10 and 6.11. The system was found to accelerate quickly, gaining the developed torque required to ramp the flywheel rotor. The flywheel experiences relatively lower losses during low speed operation as compared to high speed operation. Fig. 6.10 shows the motor mode efficiency with line of best fit.

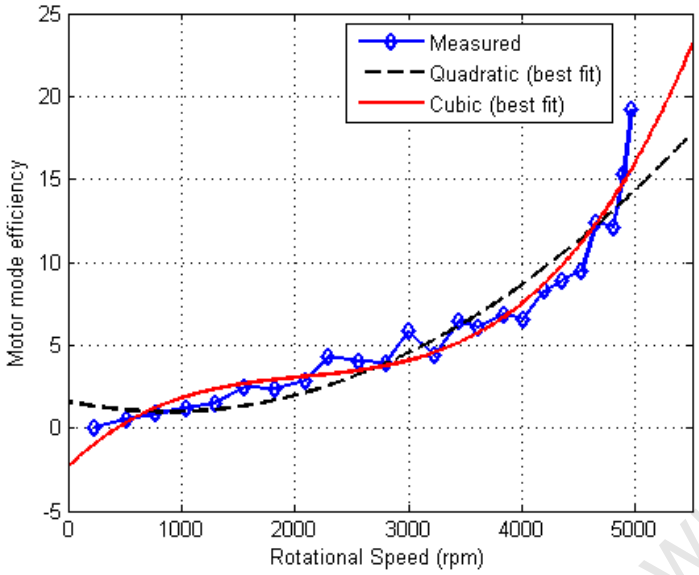

Figure 6.10: Motor mode efficiency

To ascertain the total round trip efficiency, the system is loaded during generator mode. This efficiency is also termed as the energy conversion efficiency is result of power required to convert electrical energy to mechanical in the rotating mass and back to electrical energy in generator mode. Fig. 6.11 shows the overall flywheel efficiency at rated current.

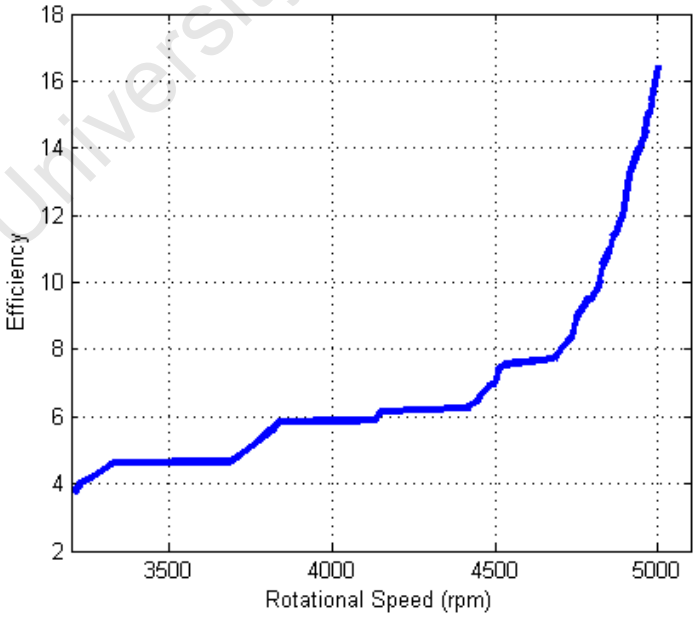

Figure 6.11: Shows the overall efficiency at 6,000rpm

It is observed that the efficiency rises with speed and takes the same form as the charging efficiency of the system. The maximum attainable is not reached due to vibrations experienced; however, this result gives a good indicator of what efficiencies can be reached.

6.2.3 Thermal Results

A thermal model was developed in chapter 5 to predict the thermal behaviour of the system. Temperature rises in the various parts of the system extracted using thermocouples in the flywheel system and Pico logger. The parts where the temperature readings were taken include, the stator windings, surface of the stator over the epoxy resin, expected routes of the heat path. The temperature on the epoxy is very important as it validates the conduction through the resin and temperature radiated to the magnets and rotor disks. Fig. 6.12 and 6.13 shows the calculated and measured stator temperatures respectively.

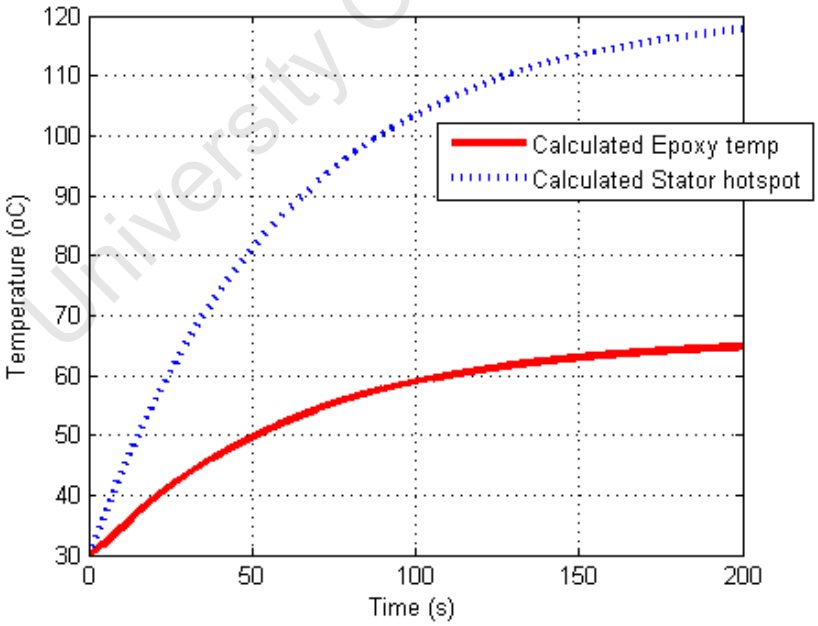

Figure 6.12: Calculated stator temperatures

The calculated temperatures in Fig. 6.12 show the predicted temperature for the stator hotspot and epoxy temperature. In Fig.6.13, the measured values are presented.

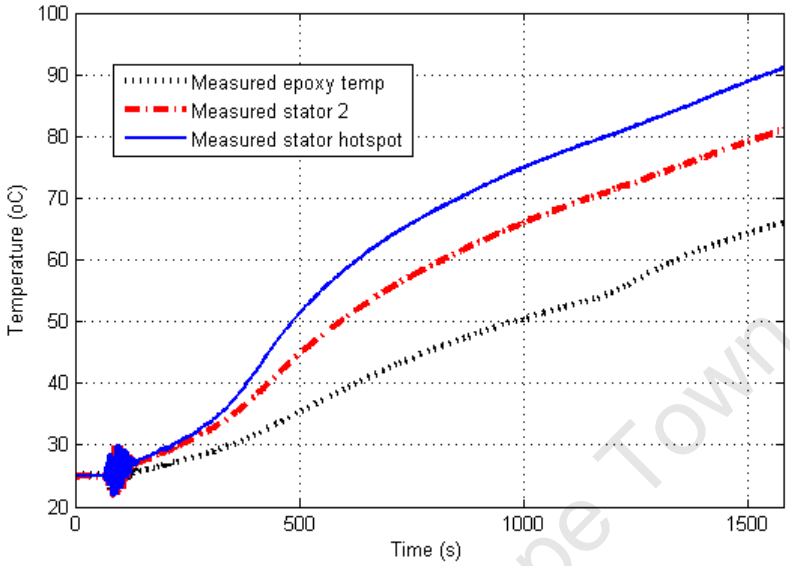

Figure 6.13: Measured stator temperatures

The predicted and measured results show some level of correlation although the difference in temperature could be between 10°C to 15°C. The flywheel system was not run until the temperature stabilized and this was because of the vibrations concerns. However, the model gives an approximation of what the temperature rise in the various components could be. The temperature rise of the other peripheral components is given in Fig. 6.14 and 6.15 which show the calculated and measured temperatures respectively.

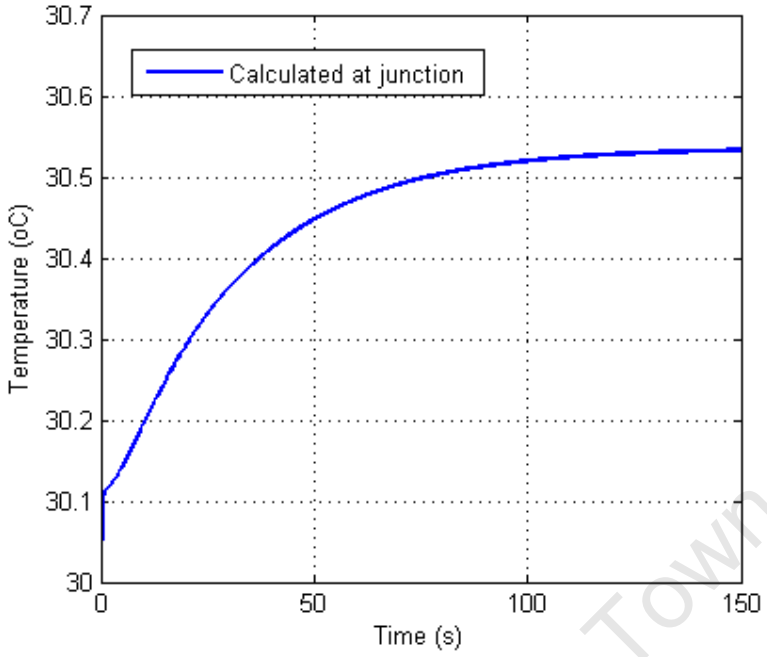

Figure 6.14: Calculated peripheral temperatures

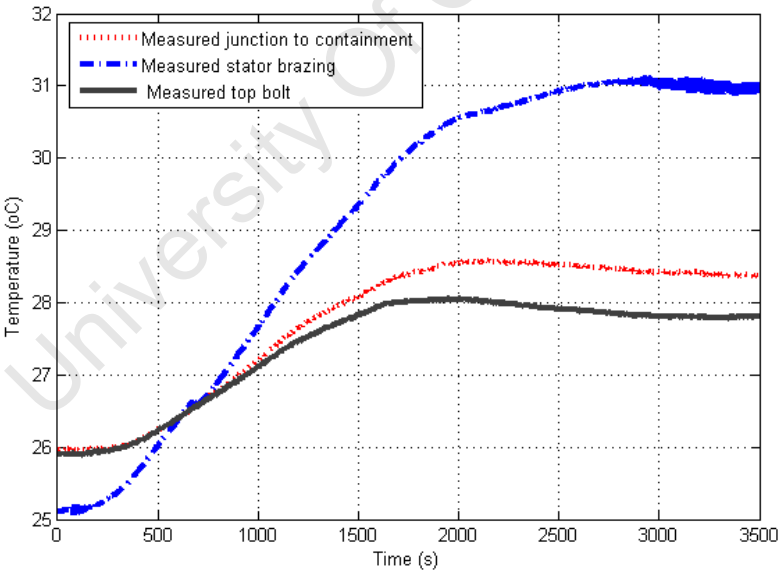

Figure 6.15: Measured peripheral temperatures

Fig. 6.14 shows only one temperature rise while Fig. 6.15 shows three. This is because in the lumped parameter thermal model considered, all the components were not considered and it is observed that the temperature rises are insignificant at rated current. The position in the model seeks to observe the worst case temperature in the stator brazing

area which is considered the heat conductivity path for this system. The model shows a good prediction against the measured values.

The accuracy of the thermal equivalent circuit can be validated by considering the measured values of the losses. It can be concluded from these tests that the thermal analysis of the flywheel system through an equivalent circuit gives sufficient information about the thermal behaviour of the system.

6.3 Concluding Remarks

This chapter explained the analysis performed on two flywheel test set ups. The results and impact of the modal and stress analysis on the performance of the system are discussed. The flywheel system with 100W machine was tested, only achieving low speed operation. The results of the system with modifications showed great improvement in performance reaching up to 6,000 rpm. The modifications of the system are also. It was observed that the sensitive parameters are the bearing system, machine, vacuum, balancing of the shaft with rotor. It was observed that the system with modifications acquired high energy to weight ratio as compared to first test system.

Chapter 7

Conclusions and Recommendations

This chapter discusses conclusion and recommendations made to the research findings. This thesis aimed to answer questions related to design and prototyping of flywheel system rural application. The findings and further work are discussed in this chapter.

7.1 Conclusions

The main research question of this thesis was whether a low cost flywheel energy storage system could be manufactured using locally available materials while maintaining its technical integrity. Replacement of lead acid battery technology with the flywheel storage systems for rural applications presents numerous advantages including, quick charge times, extended operating life, being environmentally friendly and increased efficiency. The specific objectives of this study are summarised as; critical literature review of technological trends, establishment of flywheel rotor design techniques, selection of a robust low cost electrical machine and drive and use of locally available materials to design and construct a flywheel for energy storage.

Firstly, a critical review of the concept of flywheel energy storage was explored. This was performed by reviewing the literature on flywheel development over the years by industry and academia. A number of flywheel systems have been developed to date by numerous companies and research groups but mainly for power applications. These were

mainly for frequency regulation, voltage compensation and bulk supply of power for a few seconds. No commercial flywheels are available for long term energy storage specifically for rural areas. However, advances in technologies for power and other applications were found to be vital in promoting this technology for the rural agenda. Notable is the advances in flywheel systems for vehicle application in hybrid electric & electric vehicles and the use of these systems in space applications.

The review showed that the major limitations to flywheel development are; flywheel rotor design and manufacture with high structural integrity, availability of low loss, low cost bearings, efficiency of the electrical machine, simplicity of the drive system, safety and reliability of the entire system. In addition, maintaining the idling losses at bare minimum during free spinning is very critical in realising long term energy storage.

Various techniques for designing and optimising the flywheel rotor shape were reviewed. The rationale for profiling the rotor shape of the flywheel rotor instead of the conventional shape is due to the high cost of high strength materials required for high speed operation. Two techniques were considered in the final design. Furthermore, numerous flywheel rotor manufacturing techniques were reviewed and the main driving factors of choice were cost and mechanical integrity.

The various electrical machine topologies for high speed operation were analysed. The PM machines were found to be more efficient and exhibited numerous advantages required in flywheel design. An axial flux topology for the electrical machine was finally selected due to high torque, power density, compactness and simplicity in assembly as compared to the radial topology. The machine was designed to operate in Brushless DC mode of operation due to simpler control, lower maintenance, an attribute suitable for rural applications.

It was realised that magnetic bearings are well suitable for flywheel applications as they improve on the idling efficiency. Preliminary designs for vertical oriented configurations were considered however, due to cost time factor, the use of the horizontal configuration,

conventional bearings were used. Hybrid ceramic and E2 energy efficient bearings were considered and tested for both flywheel test set ups. These bearings are locally available and fault diagnosis and maintenance can be done by local staff.

7.1.1 Findings Based on Experimental Results

The two design techniques for calculating the optimal flywheel rotor dimensions were found to ascertain the required shape that utilised less material and exhibited low mechanical stresses. One of the profiles exhibited exponential characteristics, henceforth called profile one and the one with hyperbolic characteristics called profile two. These design techniques were also found to cut down on time and complexity involved in optimal shape design.

The two profile shapes were manufactured using two techniques, cast and layered techniques. The casting method was used to manufacture both profile one and two shapes. With this technique, only 30-35% fibre to resin ratio was realised and this was attributed the low grade moulds used, which were selected for their low cost. The process of creating the shape was found to be cumbersome due to the thermal cracking of the thick flywheel rotor. The process was highly exothermic and with several attempts, the cracks were only minimised. The casting approach was hence found to be cheaper but the resultant product was limited in tensile strength. The layered technique was only used to manufacture profile two shape. Due to the thickness of the piece, the inner wall thickness was increased to accommodate the shaft and elastomeric layer. Numerous attempts to hand lay the fibre with resin infusion were fruitless. The final product was split into six parts, manufactured with 70-74% fibre-resin ratio and joined together to form a 17.6kg flywheel rotor. The flywheel rotor manufactured from this technique was found to be of high structural integrity however, the cost was more than quadruple the casting technique flywheel.

Two AFPM machines were constructed, a 100W and 500W using a similar methodology. The rotor disk of the 100W machine was built with 300WA low carbon steel and had OD of 84mm. The four pole machine utilised NdFeB arc magnet segments

with a thickness of 10mm, outer diameter of 80mm and inner of 40mm. Glue, epoxy resin and stainless steel ring were used to provide retention on the disk. The attractive forces between the magnets were contained using fixed hinges on the shaft. The 100W machine stator had a voltage rating of 36V and was wound using two strands of 0.8mm copper wire. The double layer had six coils each with 32 turns per coil. The each coil was wound separately, and then a star connection was made with two coils per phase in parallel. The stator windings were moulded in epoxy resin.

The rotor disks of the 500W machine were made from high strength carbon steel with 170mm OD. This machine utilised NdFeB magnets with arc segment of 75^{o}, 150mm OD, 80mm ID and 10mm thick. The magnets were grade 40 (maximum energy product 40MGoe), NiCuNi plating with operating temperature of $120^{o}C$. The same retention method was used except aluminium was used instead of stainless steel for mass reduction. Also, spacers rather than fixed hinges were considered to increase flexibility during assembly. The stator for the 500W machine was constructed from a 1.6mm conductor size, class H insulation with voltage rating of 150V.

Two types of conventional bearings were considered, high speed hybrid ceramic bearings used in a first flywheel test and E2 energy efficient bearings used in the second test. The frictional moments for both bearing sets were analysed. The E2 bearings reduce the frictional losses by 50% and are 95% less expensive. The major difference is in the material used in the manufacture.

The profile one rotor manufactured from the casting technique and profile two from the layered technique were shaft-coupled to the 100W and 500W electrical machine respectively. The first set was tested at normal pressure and speeds of up to 350 rpm were achieved at rated current. The system was supplied with three times the current reaching speeds of up to 1,000 rpm. This high loss was mainly attributed to the frictional loss from the hybrid ceramic bearings. During this time, over heating was realised in the 100W electrical machine and the supply cut off. The flywheel system with the 500W machine was assembled with E2 energy efficient bearings and accelerated under reduced

air pressure containment up to 6,000 rpm at rated current of 10A. Measurements of charging efficiency, which excluded losses in the inverter and generator mode, were made reaching up to 21% efficiency. The average energy conversion efficiency was found to be 18% at 6,000 rpm. The flywheel system was able to store up to 77Wh, which represents 25.6% of the design energy requirement.

A thermal model was developed for the flywheel system to accurately determine the thermal behaviour of the system. This was essential in predicting temperature rise in the different components of the system. The experimental results were found to agree with theory; hence the model was sufficient to check for temperature rises in the different parts of the flywheel system in case of change in design parameters.

Critical to this research was the design, prototyping and analysis of a test rig used to evaluate the performance of the flywheel system. This system was designed with the ability to test various flywheel energy storage systems, flywheel rotors, high speed electrical machines, drives and bearings.

A comparison was done between the life cycle costs of the traditional lead acid battery storage system and a proposed electromechanical flywheel battery for a rural energy storage application, using two different models. It was shown that the flywheel is more cost effective in the long run than the traditional lead battery. Integrating the flywheel system into Solar Home Systems would mean making a saving of 35% per kWh with rural systems, under current conditions. This situation will improve even further in favour of the flywheel given that this technology is still in transition while the lead acid has practically reached its technical development.

7.1.2 Limitations of the Flywheel Prototype

The flywheel system was not accelerated to its rated operating speed range due to vibrations encountered at 6,000 rpm. Numerous reasons were attributed to this.

- During the prototyping stage, only low speed balancing was achieved. Yet, high speed balancing is essential in eliminating residual imbalance in the system during high speed operation. Attempts to have the shaft-flywheel-machine system balanced were unsuccessful as commercial high speed balancing experts were not familiar with the flywheel rotor and its failure criteria.

- The flywheel rotor used in the high speed acceleration was hand layered creating uneven fibre distribution in the E-glass composite rotor. At higher speeds, the distribution affects the balancing inducing vibrations.

- The vibrations were also attributed to the flywheel shaft load imbalance. The placement of the flywheel rotor and rotor disks on the shaft was analysed using a FE method however the positioning was not optimised. The unbalance created in the positioning resulted into excessive forces on one side of the bearing structure. Notably, the bearing had to be changed during further testing.

- The assembly of the flywheel system on the test rig was considered as a source of error. Small fabrication errors resulted in misalignment, unbalance and uneven air gap clearance in the electrical machine. This was attributed to using many fabricators.

Other problems include; fluctuation in the vacuum levels, limited thermal conductivity path and increased size of flywheel rotor.

7.2 Recommendations

Results, analysis and performance of the high speed flywheel have been presented and based on the findings, the following recommendations are made.

An optimised flywheel system can be achieved by closely linking the optimisation design criteria of the flywheel rotor design to the electrical machine and drive design algorithms.

Two techniques for developing flywheel rotor profiles have been discussed and were sufficient in delivering the required inertial mass however, mechanical and structural design optimisation could be investigated using numerical optimisation techniques. This could open avenues to use the more expensive carbon fibre which can attain higher rotational speeds.

The flywheel rotor, which is the only orthotropic composite in the system, was balanced for only low speed. High speed balancing is therefore required to avoid vibrations. A more balanced flywheel rotor could be achieved using an aluminium master plug-in for the casting manufacturing technique and computer based programs to lay the fibre in the lamination (layered) manufacturing approach.

A critical and sensitive aspect of this thesis was the bearings. Further research could focus on low cost magnetic bearings and these would significantly reduce the frictional losses. For rural applications, the research could focus at ease of construction, repair, assembly and replacement. Magnetic bearings were considered in the first phase of this research however due to cost and time constraints, this was not achieved. In the short run, it is envisioned that cheaper and more efficient conventional bearings will be produced. This specific trend is driven by the armature rewind market. These bearings could further ease the cost. In the long run, magnetic bearings will drop in cost and complexity, making them readily available for rural applications. Importantly, the

conventional bearings are easy to assemble and fault detection is possible using local technology, something well suited for the rural applications.

The stator winding structure was appropriately designed however the use of epoxy resin to improve on the structural integrity is counter progressive. The heat from stator windings is not sufficiently conducted across. An epoxy resin with a thermal conductivity of 0.35W/mK was considered. The use of a good conductor would mean a clear heat conductivity path from the source hence reducing the complexity resulting from modelling radiation. However, the utilisation of a good conductor would interfere with the magnetic path. In addition, the material considered should be able to withstand the high mechanical forces exerted on the stator as current is supplied. Further work could also consider the use of a water cooled stator using silicon tubing. The efficiency and the choice between natural and forced cooling could be investigated.

Cost optimisation of the electrical machine is essential as the PM magnets were found to be expensive. However, the South African government is looking at manufacturing magnets to reduce the cost of PM machine manufacture that can be used for not only flywheel technology but also the penetration of PM machines for renewable energy.

The drive system topology was not fully utilised. The system was manually operated without the use of the DC-DC converter. The system could be extended to fully utilise the DC-DC converter and replace the dSPACE control desk with a microcontroller. This study could also include the efficiency considerations due to the power electronics.

The performance of the flywheel energy storage system was not fully assessed because of the vibrations observed during its operation. Vibration analysis concerns arising from imbalance and mechanical alignment could be investigated so as to realize increased operating speed range of the flywheel energy storage system.

APPENDICES

Appendix A: Publications

A1. Conferences

1. R.Okou, M.A Khan, A.B Sebitosi, P.Pillay A Case for Electromechanical Energy Storage, *SAUPEC08, Durban, 2008*.

Flywheels are energy storage devices that have been around for thousands of years. The origins and use of modern flywheel technology for mechanical energy storage can be traced to several hundred years ago and was further developed throughout the industrial revolution. These systems exhibit many advantages over other energy storage systems. However, the original designs were costly, unsafe and limited by power electronics, strength of materials and bearings. In the recent years, there have been renewed interests due to technology developments in those areas. This paper could contribute to the betterment of various sectors and applications including; transport, environment, rural electrification, power quality among others.

2. R.Okou, M.A. Khan, A.B. Sebitosi, P. Barendse, P. Pillay, An Approach to High Speed Electromechanical Flywheel and Brushless DC Machine design, *SAUPEC09, Stellenbosch 2009*.

This paper presents a design of a high speed electromechanical flywheel for energy storage. A brushless dc machine was designed as a motor/generator. The design procedures for the machine are discussed. The system is explored both analytically and using finite elements. The rotating flywheel rotor is designed using fibre and epoxy and envisaged to operate between 8,000 rpm and 25,000 rpm. Stress and electromagnetic analyses together with loss models are presented. The total loss of the system was found to be 28.3W which corresponds to 10 hours of idling. The maximum radial and hoop stresses were found to be below the designed maximum stresses for all the rotating components.

3. G.Mwaba, R.Okou, M.A Khan, P. Pillay, Comparison of Permanent Magnet Topologies for High Speed Flywheels, *SAUPEC09, Stellenbosch, 2009.*

This paper discusses the comparison of several PM machine topologies for use in high speed flywheels. A high level comparison of four topologies is done including outer rotor Halbach array, radial flux, axial flux and double rotor single stator machines. A detailed comparison based on analytical modeling is then performed for a brushless ac and brushless dc machines.

4. R.Okou, G.Mwaba, MA Khan, P. Barendse, P Pillay, High Speed Electromechanical Flywheel Design for Rural Electrification in Sub Saharan Africa, *IEEE International Electrical Machines and Drives Conference (IEMDC) 2009.*

This paper presents the electromechanical flywheel energy storage system designed to enhance rural electrification in sub-Saharan Africa. Most non-grid connected areas, mostly rural, are powered with solar home systems whose sustainability is limited by the short life span, low power density and low storage efficiency of the battery storage. The electromechanical flywheel rotor is made from glass fiber and epoxy composite and designed using novel shape profiles based on Berger, Porat and Stodola's design. Dr. Stodola's design utilizes a stress based solution by introducing a central hole for a shaft inclusion. An Axial flux brushless DC machine was considered because of the low cost, ease of construction and simple control. The system stores 1,080kJ and supplies 100W with an operating speed range of 8,000-25,000 rpm. Stress, modal and thermal analysis are performed on the flywheel system using finite elements and analytical methods. The brushless DC drive together with the DC-DC converter were constructed and tested. The various components were simulated, prototyped using locally available material and the results presented.

5. R.Okou, MA Khan, P. Barendse, P. Pillay, Test Rig for High Speed Electromechanical Flywheels in Sub Saharan Africa, *IEEE International Electrical Machines and Drives Conference (IEMDC) 2009.*

This paper presents a test rig designed at the University of Cape Town to evaluate the performance of a high speed electromechanical flywheel for energy storage. The electromechanical flywheel is specifically designed to enhance rural electrification through improving the energy storage component in solar home systems. A safe, flexible and low vibration test rig has been designed. Modal analysis using an FE package ANSYS was used to validate the low vibrations at high speed rotation. Special attention was given to the alignment issues and this was done to avoid imbalance in the rig. The rig has the ability to test up to 40,000 rpm flywheel with maximum diameter of 0.55m as is. With changes in the bearings, much faster flywheels can be tested. In addition, the rig was built to ensure testing under various operating environments. A thermal model was developed for the rig and simulated with analytical and FE packages. Sensors are

installed in the containment to monitor performance of flywheel system.

6. R.Okou, M.A. Khan, P. Barendse, P. Pillay, Considerations to high speed electromechanical flywheel design for sub-Saharan Africa, *IEEE, Electrical Power and Energy Conference (EPEC) 2009, Montreal, Canada.*

The results of an electromechanical flywheel are presented to ascertain the considerations during the design stage. The design procedure is explained in brief. The considerations include, load profiling, mechanical and electrical aspects are discussed. This is essential in achieving the numerous advantages associated with the flywheel energy storage system. The results for low speed testing are presented with considerations to improving the system.

7. R.Okou, MA Khan, P. Barendse, P Pillay, Thermal Analysis of flywheel with brushless DC machine, *IEEE, Electrical Power and Energy Conference (EPEC) 2009, Montreal, Canada*

A thermal model of an electromechanical flywheel with a brushless DC machine is presented. Thermal analysis is particularly important during vacuum operation of the flywheel. Accurate prediction of temperature facilitates material selection and structural integrity which good performance. In addition, the choice of vacuum level, bearings, conductor sizes and system overload capability can be attributed to a good thermal model. A thermal model was developed and simulated on MATLAB Simulink. The simulation results were compared with experimental results and a good correlation was observed.

A2. Journals

8. AB Sebitosi, R.Okou, Re-thinking the power transmission model for sub-Saharan Africa, *Elsevier Policy 38 (2010) 1448-1454.*

A vision for a United States of Africa has been advocated since the dawn of independence by, among others, pioneers like Kwame Nkrumah, Gamal Abdel Nasser and Julius Nyerere. More recently the idea gained new momentum, through such initiatives as the New Partnership for African Development (NEPAD) and the African Union (AU) to create a single market of Africa's 750 million people that is competitive within itself and within the global economy. This would be achieved through a deliberate, systematic and concerted effort to integrate, upgrade and modernize

infrastructure that would offer the required catalyst for economic growth. However, the prioritization by African policy makers of a grand plan to link up the entire African continent's electric power grid networks would appear to be incompatible with 21st century thinking. The specifications for a centrally managed power grid were made by Nicola Tesla in 1883 and have served the power industry for over 125 years but are now obsolete in the era of digital micro-electronics and smart grid concepts. This paper examines some issues that surround the evolution of sub-Sahara African regional power pools and highlights the anomalies and perhaps wrong timing around the conceptualization and prioritization of grand inter-state power grids. The authors then propose an alternative model that conforms to a new and more sustainable paradigm in electricity supply economics. The proposals are however not meant to provide a panacea but it is hoped that the article will ignite a debate that will lead to a lasting solution.

9. R.Okou, M.A. Khan, A.B. Sebitosi, P. Pillay, Possible Impact of Small Scale flywheel Energy Storage Technology on Uganda's Energy Sector*, Journal of Energy South Africa, Volume 20, No 1, February 2009*.

The energy crisis in Uganda has caused a sharp decline in the growth of the industry sector from 10.8% to 4.5% between 2004/5 and 2005/6. This crisis has escalated the power disruptions, which have had adverse effects on various sectors. While business owners have resorted to importation of fossil fuel generators that have increased the cost of production, others have resorted to battery energy storage systems to cater for short outages, which are limited in life span, depth of discharge, among others. These interventions have, thus further, increased the cost of goods and services. In addition, the rural populations using solar home systems incur high battery maintenance and replacement costs. In this paper an electromechanical flywheel battery is proposed as a better alternative in mitigating energy storage problems. It is found that by replacing the battery storage systems with the electromechanical flywheel battery, a saving of up to 35% on cost of energy can be made in the solar home systems and for the industry sector, the power disruptions could be reduced.

A3. Under review

10. R.Okou, M.A. Khan, P. Barendse, A.B. Sebitosi, P. Pillay, An electromechanical battery for rural electrification in sub-Saharan Africa, *IEEE ECCE 2010.*

This paper presents an electromechanical battery energy storage system designed to enhance rural electrification in sub-Saharan Africa. The system consists of a flywheel rotor, an electrical machine, bearings and a containment structure. The flywheel rotor was constructed from E-glass fiber, the machine from imported NdFeB magnets and commercial energy efficient bearings. With the exception of the power electronics and magnets, local materials were used for the manufacture of the flywheel system. The

system was designed to operate between 8,000 rpm to 25,000 rpm with a rated storage capacity of 300Wh. Numerical stress analysis was performed during the design stage to ensure that the maximum tensile strength is not exceeded. A lumped parameter thermal model was used to estimate the temperature distribution to ensure safe operating conditions of the flywheel system and environment. The system was accelerated to 6,000 rpm and the results are presented.

11. R.Okou, M.A. Khan, P. Barendse, P. Pillay Test rig for high speed electromechanical flywheels in sub-Saharan Africa, *IEEE Transactions on Energy Conversion*

This paper presents a test rig designed and developed to evaluate the performance of a high speed electromechanical flywheel for energy storage. The system is specifically designed to enhance rural electrification through improving the energy storage component in Solar Home Systems (SHSs). Two electrical machines built with high mechanical integrity rated at 100W and 500W are used to test different flywheel rotors. The drive system is able to test different types of machines and/or flywheel systems. The friction moments of the bearings used are highlighted. Modal analysis using an FE package ANSYS was used to investigate the vibrations at high speed rotation. The rig has the ability to test up to 40,000 rpm flywheels with a maximum outer diameter of 465mm as is. With changes in the bearings, much faster flywheels can be tested. The rig was built to ensure testing under various operating environments. A thermal model was developed for the rig and simulated with analytical and FE packages. Thermocouples are installed in the containment to monitor thermal performance of flywheel system.

12. R.Okou, M.A. Khan, P. Barense, P. Pillay, High Speed electromechanical flywheel design for rural electrification in sub-Saharan Africa, *IEEE Transactions on Energy Conversion*

This paper presents the electromechanical flywheel energy storage system designed to enhance rural electrification in sub-Saharan Africa. The system consists of a flywheel rotor, electrical machine, drive system, bearings and containment structure. The flywheel rotor is made from glass fiber and epoxy composite and designed using novel shape profiles based on Berger, Porat and Stodola's design. Dr. Stodola's design utilizes a stress based solution by introducing a central hole for a shaft inclusion. An Axial Flux Permanent Magnet (AFPM) machine topology was considered for two machines with the driving factors of choice being low cost, ease of construction and simple control. The system is capable of storing 227kJ with a designed operating speed range of 8,000-25,000 rpm. Stress, modal and thermal analysis are performed on the flywheel system using Finite Elements (FE) and analytical methods. The Brushless DC drive (BLDC) was constructed and tested. The various components were prototyped using locally available material, assembled, tested and the results presented.

13. R.Okou, M.A. Khan, A.B. Sebitosi, P. Pillay, Local manufacture of high speed flywheel rotors for rural communities in sub-Saharan Africa, *IEEE Transactions on Sustainable Energy*

This paper presents the electromechanical flywheel rotor prototypes designed to enhance rural electrification in sub-Saharan Africa. The flywheel rotor was made from E-glass fibre with epoxy resin and designed using novel shape profiles based on Berger, Porat and Stodola's designs. Dr. Stodola's design utilizes a stress based solution by introducing a central hole for a shaft inclusion. The rotors were manufactured using locally available materials. A test rig with an axial flux brushless DC machine topology was used to test one of the flywheel rotors storing 227kJ. A life cycle cost analysis was performed to compare the energy costs between the battery and flywheel rotor system. It was realized that by integrating the flywheel system into Solar Home Systems would result in a saving of 37% per kWh for rural system installations.

Appendix B: Numerical stress analysis

B1. Profile one stress analysis

- **Normal Stress**

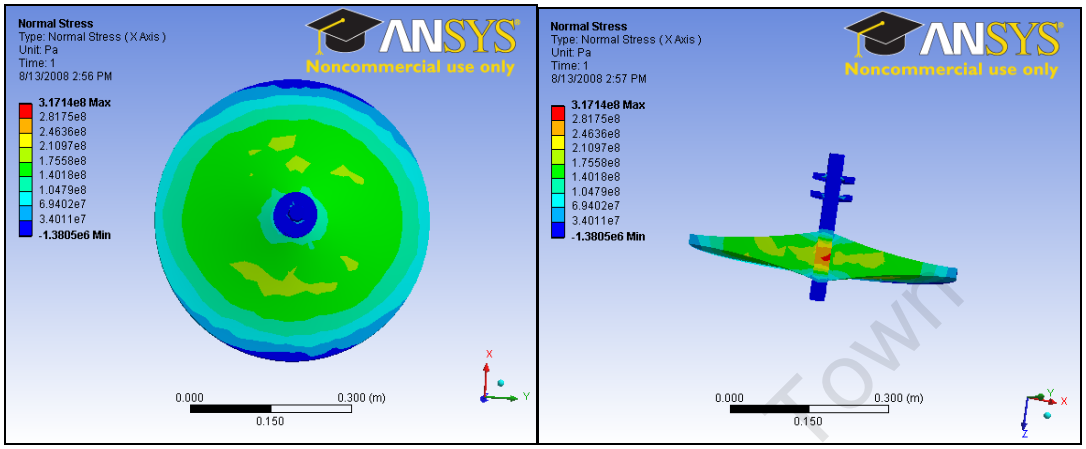

- **Shear Stress**

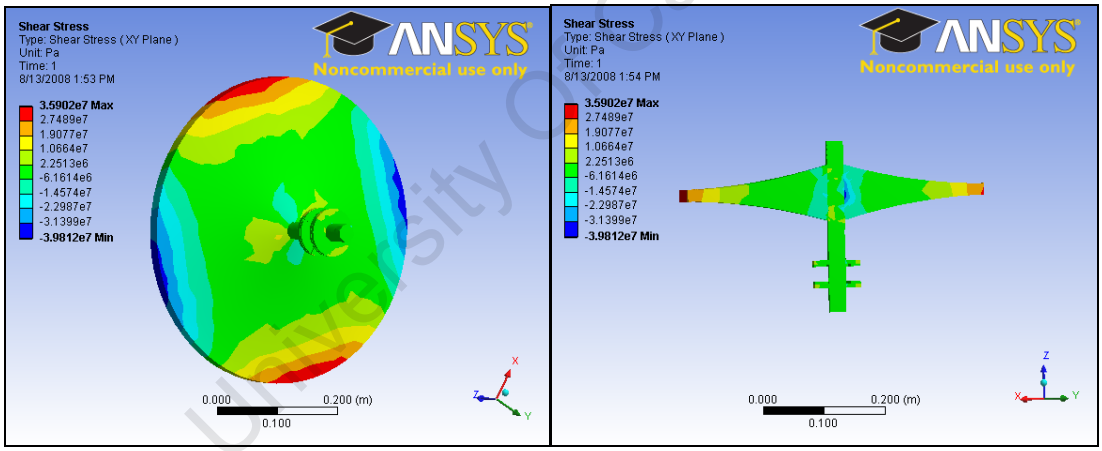

B2. Profile two stress analysis

- **Normal stress**

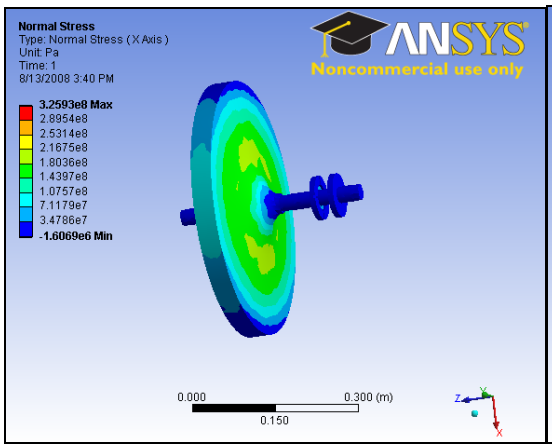

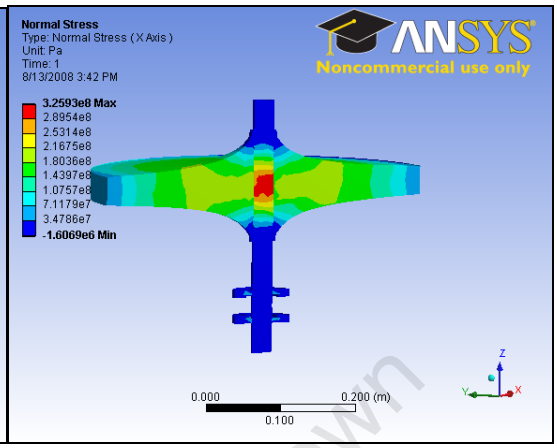

- **Shear stress**

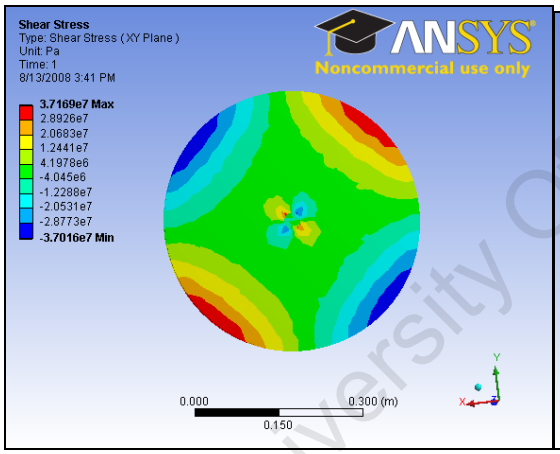

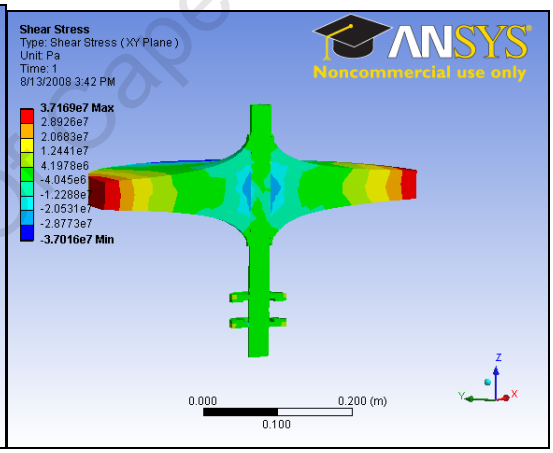

B3. Profile two with modifications

- **Maximum Principal elastic strain and normal stress**

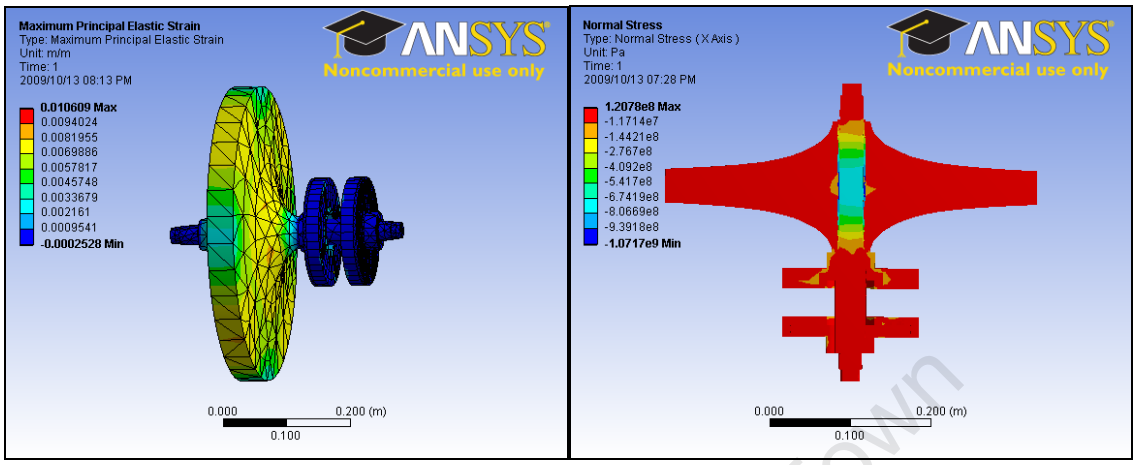

- **Shear Stress**

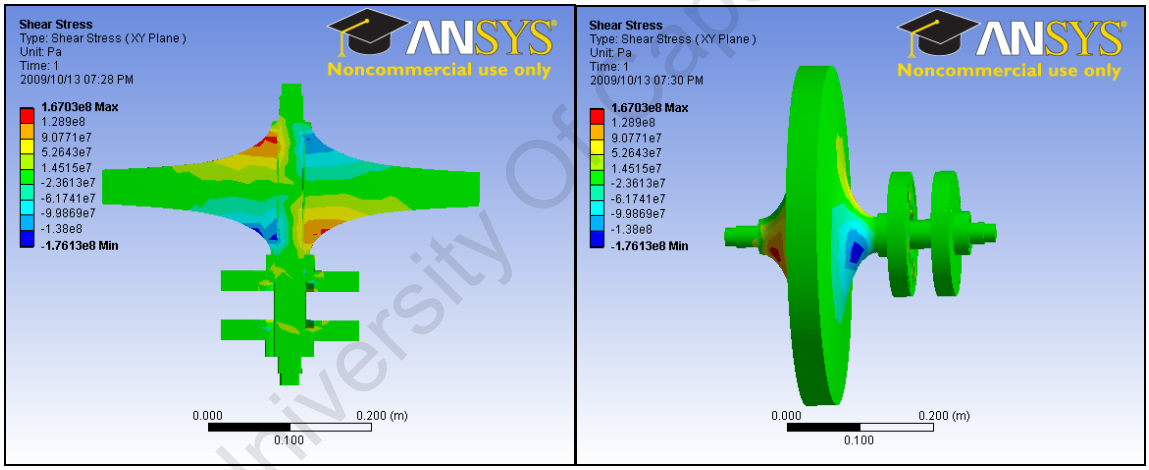

- **Maximum shear elastic strain**